ARMY RESEARCH LABORATORY

Damage Tolerance of Thick-Section Composites Subjected to Ballistic Impact

by Bruce K. Fink, Ahmed M. Monib,
and John W. Gillespie, Jr.

ARL-TR-2477 — May 2001

20010601 067

Army Research Laboratory
Aberdeen Proving Ground, MD 21005-5069

Damage Tolerance of Thick-Section Composites Subjected to Ballistic Impact

Bruce K. Fink
Weapons and Materials Research Directorate, ARL

Ahmed M. Monib and John W. Gillespie, Jr.
University of Delaware

Abstract

There are two predominate modes of failure in a compressively loaded laminate that has been subjected to ballistic damage. Analysis has shown that the stress concentration and the membrane failure are sensitive to the in-plane stiffness matrix of the damaged region, while delamination growth failure is dependent on the size and location of the damage as well as the fracture toughness of the material. An experimental study investigated means of improving damage tolerance ranging from resin toughness to through-thickness stitching. From the experimental study, it was found that improving fracture toughness by through-the-thickness stitching resulted in a reduction in damage size. Stitching may cause severe reductions in stiffness of the damage region as projectile energy is absorbed through the fiber breakage and pullout mechanisms. Thus, while stitching improves multi-impact performance, it may also lead to an increase in fiber damage, causing the compression after ballistic impact (CABI) failure mode to shift from delamination growth to membrane failure. A design trade-off exists between maximum fracture toughness and stiffness reduction induced within the ballistically damaged region. By examining the factors affecting residual strength (i.e., fracture toughness, inclusion stiffness, loading condition, and finite width effects) the methodology to develop design chart may be produced to optimize damage tolerance.

Table of Contents

INTENTIONALLY LEFT BLANK.

List of Figures

viii

ix

x

List of Tables

Executive Summary

Damage tolerance of thick-section composite materials subjected to ballistic impact can be defined as the ability of a structural component to withstand multiple impact damage and remain structurally functional; improving the Mode I fracture toughness of a composite laminate reduces damage size upon ballistic impact. Increasing fracture toughness can improve compression after ballistic impact (CABI) strength, depending on the failure mode. There are two predominate modes of failure in a compressively loaded laminate that has been subjected to ballistic damage. In-plane or membrane failure occurs when stress concentrations that develop around the damaged region increase stress levels that exceed the strength of the material. Delamination growth failure occurs when interlaminar defects resulting from ballistic impact cause sublaminate buckling resulting in unstable delamination growth. Analysis has shown that the stress concentration and the membrane failure are sensitive to the in-plane stiffness matrix of the damaged region, while delamination growth failure is dependent on the size and location of the damage as well as the fracture toughness of the material. An experimental study investigated means of improving damage tolerance ranging from resin toughness to through-thickness stitching. From the experimental study, it was found that improving fracture toughness by through-the-thickness stitching resulted in a reduction in damage size. Stitching may cause severe reductions in stiffness of the damage region as projectile energy is absorbed through the fiber breakage and pullout mechanisms. Thus, while stitching improves multi-impact performance it may also lead to an increase in fiber damage, causing the CABI failure mode to shift from delamination growth to membrane failure. A design trade-off exists between maximum fracture toughness and stiffness reduction induced within the ballistically damaged region. By examining the factors affecting residual strength (i.e., fracture toughness, inclusion stiffness, loading condition, and finite width effects) the methodology to develop design chart may be produced to optimize damage tolerance.

INTENTIONALLY LEFT BLANK.

1. Introduction

1.1 Background. During the past 20 years, applications for composites have grown rapidly. Composites continue to be used in weight-critical structures such as space, aerospace, and high-performance military systems. New advances in manufacturing processes combined with decreasing material costs have led to their widespread use in the automotive and sporting goods industries. Recently, composites have entered the infrastructure market as hundreds of thousands of decaying bridges across the country are in desperate need of repair.

Although composites offer many unique advantages over traditional materials, they remain sensitive to impact loading. When a composite material is subjected to low-velocity or ballistic impact, delaminations, matrix cracking and fiber breakage may result. This, in turn, leads to a reduction in the component's residual strength. Repair of such damaged parts is often difficult and time consuming. Thus, it would be highly beneficial to develop means of improving damage tolerance so that repair becomes unnecessary. Damage tolerance is defined as the extent of damage that a structure may withstand and still be structurally functional (functionality is determined based on the design requirements).

Design optimization of composite ballistic armor for military applications typically focuses on the armor's ability to withstand multiple ballistic impacts and remain structurally functional (Fink 2000). To date, the majority of research efforts have focused on improving the compression after impact (CAI) strength of thin-section aerospace composites. Little work has been done on the compression after ballistic impact (CABI) strength of thick-section composites (i.e., thickness greater than 0.6 in) and less work still on multiple hit performance of armor panels. In addition, the work presented herein shows that a design trade-off exists between improving multihit performance and improving residual strength.

Improvements in multi-impact performance are gauged by measuring the size of the damaged area generated. Smaller damage areas result in improved multi-impact performance. This is

1

typically accomplished by improving the interlaminar fracture toughness of the material. However, ballistic impact absorbed in a smaller damage area leads to severe fiber damage that reduces in-plane stiffness in this region. This results in increased stress concentrations that reduce the residual strength.

In this study, methods for improving damage tolerance of thick-section composites have been considered. The effects of through-thickness stitching, resin type, and manufacturing processes on damage reduction and residual strength were experimentally investigated. Analytically, the factors affecting residual strength (i.e., fracture toughness, in-plane stiffness, loading conditions, and finite width effects) were examined in order that design charts may be generated to determine the optimal fracture toughness for reducing damage size and increase residual strength.

1.1.1 Delamination Damage in Aerospace Composites. Often the result of impact damage is severe delamination of the composite structure. The aerospace industry has investigated the delamination damage of thin-section composites extensively, particularly carbon/epoxy laminates. Delaminations are a common defect in composite aircraft structures. Delamination defects arise not only from low-velocity impact damage (bird strike, dropped tools, hail, etc.) but also from processing defects and assembly-induced damage. An example of assembly-induced damage is delaminations around fastener holes due to unshimmed gaps and improperly installed fasteners (Wanthal et al. 1993). Since composite aerospace structures are often assembled into large structural components, the cost of repairing or replacing damaged components can be considerable.

Two types of delaminations generally occur when manufacturing composite structures: single-level and multilevel delaminations. Single-level delaminations are generally caused during processing, while multiple-layer delaminations generally occur due to improper assembly or low-velocity impact damage. Other types of defects such as matrix cracking and fiber breakage often exist in structures with multiple-layer delaminations.

2

Many researchers have investigated the effects of single-level delaminations on the static compression strength and fatigue life of thin-section composite components. Compared to the published research available on single-level delaminations, the available literature on multilevel delamination is less prevalent (Wanthal et al. 1993).

In 1988, McDonnell Douglas Aerospace discovered assembly-induced delaminations in the upper compression wing skin of an AV-8B. The results of strength tests showed that larger delaminations lead to greater reductions in compression strength. In addition, for a given delamination size, a larger reduction in compression strength was observed for the thin laminates than for the thick laminates. Interestingly, most specimens showed no delamination growth under cyclic loading. Resin infusion repairs were found to improve compression strength on average by 15%. Further details on the McDonnell Douglas AV-8B project can be found in Wanthal et al. (1993). Similar repair approaches are viable for thick-section composite armor.

In addition to the extensive study conducted on assembly-induced delaminations, investigations have been performed on low-velocity impact as another source of delaminations (Wanthal et al. 1993; Chai 1982; Naval Air Development Center 1986; Madan 1989; Horton and Whitehead 1988; Ramkumar 1982; Williams 1984; Guynn and O'Brien 1985). Impact damage can occur at almost any time during the service lifetime of an aircraft. Some examples include damage caused by falling tools, hailstones, debris, collision with ground service vehicles, etc. Damage caused by impact is not always visible, thereby making it difficult to determine if delaminations or matrix cracks are present. Although a considerable amount of research has been conducted towards understanding impact damage on the strength of composite structures, the effects of geometry, layup, thickness, etc., are still not well understood.

Madan (1989) presented an investigation of the effect of impact energy and laminate thickness on the in-plane compression strength of a toughened carbon/epoxy system. Impact tests were conducted on test specimens using a Dynatup impact machine, whereby a hemispherical projectile is dropped from a certain height with weights attached. The impact

3

energy level imparted to the specimen is recorded, and the specimen is inspected using nondestructive evaluation (NDE) to determine the extent of damage. The specimens were then tested for in-plane compression strength. Madan's paper concludes that at low energy levels, past a threshold value, strength decreases linearly with the square root of impact energy. This behavior exists until a plateau is reached, after which no further strength reduction is seen. Madan (1989) has also shown that thinner laminates required less energy to delaminate, but the plateau strength was approximately the same that of the thicker two laminates. The thermoplastic systems showed a 10% plateau strength improvement over the thermoset resins.

Surveys conducted by Horton and Whitehead (1988), indicate that impact damage is the most critical type of ordinary defect found in composites. Horton and Whitehead's work examines the effects of damage due to impact, single level delaminations, flawed fastener holes, and voids. Results show that barely visible impact damage can cause reductions in compression strength up to 60%, while single level delaminations of equal size reduce compression strength by only 10%.

Due to the detrimental effects of delamination damage, analysis techniques to predict residual strength are sorely needed. Several techniques have been proposed and will be discussed in the following section.

1.1.2 Predicting Compression After Impact Strength. Compression failure in impact damaged composites is primarily the result of stiffness loss in the damaged region or interlaminar defects as discussed above. The elliptical inclusion model proposed by Lekhnitskii (1968) is an elegant analytical technique for assessment of the stress and strain distribution in a composite structure, where stiffness losses in the damaged region led to high stress concentrations that cause failure. A detailed description of Lekhnitskii's solution is presented in section 3. Many authors have used Lekhnitskii's approach to determine the stress state in a damaged composite (Cairns 1987; Nyman et al. 1998; Xiong et al. 1995; Wanthal et al. 1993). Once the stress distribution is known, a variety of failure criteria can be applied to predict strength. To date, a consensus has not been reached regarding the proper set of failure criteria. This is mostly due to

the fact that composite systems demonstrate different failure modes and damage mechanisms and thus may require different analytical and experimental techniques. Awerbuch and Mudhukar (1985) give a comprehensive literature review on the commonly used fracture models. In this study a standard point stress or average stress criterion is applied to predict failure (Whitney and Nuismer 1974).

Interlaminar defects resulting from impact energy may lead to unstable delamination growth when compressively loaded. Delamination growth failure can be characterized using strain energy release rate concepts (Broek 1986). The advantage of this approach lies in the relative ease by which mathematically defined quantities can be related to physically measurable quantities (Gillespie 1991).

A multitude of authors have examined the use of Mode I, Mode II, and total strain energy release rates (G_I, G_{II}, and G, respectively) to predict interlaminar crack propagation. Ashizawa (1981) used a stress intensity approach, together with an assumed delamination growth criterion that relies solely on the opening mode of crack displacement. Gillespie and Pipes (1984) use a similar approach using strain energy release rate. Rothschilds et al. (1988) has investigated mixed-mode crack propagation in compressively loaded thermoset and thermoplastic columns using beam theory and finite element modeling (Whitcomb 1989) of the crack tip. Expressions were derived for the Mode I and Mode II components of strain energy to predict the critical load at the onset of delamination growth. El-Denussi and Weber (1986), Sallam and Simitses (1985), and Chai and Babcock (1985) have investigated delamination growth using the total strain energy release rate criterion. However, using the total strain energy criterion to predict delamination growth is not generally applicable to geometeries where failure is either Mode I or Mode II dominated. Generally, a mixed-mode criterion is needed, such as that proposed by Johnson and Mangalgiri (1985), where the onset of crack growth occurs when $(G_I/G_{IC}) + (G_{II}/G_{IIC}) = 1$.

Energy balance for fracture states that crack growth can occur if the energy required to create additional crack surface area can be delivered by the system through the formation of an additional crack length, da (Gillespie 1991). Mathematically, this is stated as:

$$\frac{d}{da}(F - U) = \frac{dW}{da},$$

(1)

where U is the elastic strain energy stored in the body, F is the work supplied by external forces and W is the energy required to form a crack. The total strain energy release rate, G, and the crack resistance, R, are defined as:

$$G = \frac{d}{da}(F - U)$$

(2)

and

$$R = \frac{dW}{da}.$$

(3)

From an experimental perspective, the total strain energy release rate can be expressed as

$$G = G_I + G_{II} + G_{III} = \frac{P^2}{2w}\frac{\partial C}{\partial a},$$

(4)

where P is the applied load, C is the compliance, and w is the width of the specimen. An expression for compliance as a function of crack length is determined experimentally. Experiments are generally designed to separate the strain energy modes. For mix-mode test

6

specimens, it is not possible to determine G_I, G_{II}, and G_{III}, from experimental measurements alone (Gillespie 1991). The total critical strain energy release rate, G_c, is defined in terms of the critical load just prior to crack growth. The Mode I (G_I), Mode II (G_{II}), and Mode III (G_{III}) critical strain energy release rates are thus material properties determined experimentally. Increasing the materials fracture toughness (i.e., matrix toughness or stitching) increases the resistance to delamination growth and improves damage tolerance of the composites.

Delamination growth failure of an impact-damaged specimen is initiated by instability-related growth of sublaminates that have delaminated during the impact. Residual properties are determined by deriving expressions for the strain energies, based on the assumption that post-buckled shape will occur under compression loading, and then applying an appropriate mixed-mode failure criterion.

One form of a general mixed-mode growth criterion is given by

$$\left(\frac{G_I}{G_{IC}}\right)^a + \left(\frac{G_{II}}{G_{IIC}}\right)^b + \left(\frac{G_{III}}{G_{IIIC}}\right)^c = F. \tag{5}$$

Failure is assumed to occur when $F(G_I, G_{II}, G_{III}) = 1$. Various forms of the criterion have been proposed where the parameters a, b, and c are varied. The most commonly accepted forms are the linear (a = b = c = 1) and the quadratic (a = b = c = 2). Fundamental input to the failure criteria is the Mode I, Mode II, and Mode III critical strain energy release rates, which are determined by standard ASTM test methods (Gillespie 1991). Further details on the delamination growth failure criteria will be discussed in section 3.

In this study, an analytical model is used to predict CAI strength and the predominant mode of failure: in-plane failure or instability-related delamination growth. The model is based on Lekhnitskii's in-plane failure analysis and Flanagan's (1988) delamination growth model and

7

will be discussed in further detail in section 3. The model was experimentally verified for thin-section carbon/epoxy systems by McDonnell Douglas and for thick-section glass/resin systems in the present study.

1.1.3 *Methods for Improving Damage Tolerance.*

1.1.3 Methods for Improving Damage Tolerance. To avoid the need for repair, recent research has focused on improving damage tolerance. As mentioned earlier, damage tolerance is defined as the extent of damage that a structure may withstand and still be structurally adequate. This can be accomplished in one of two ways: by improving the laminate's ability to withstand ballistic impact or by improving the post-impact properties.

Although the damage evolution within composites during ballistic impact is not well understood, damage tolerance of composites subjected to quasi-static compressive loading has been studied extensively (Monib et al. 1998; Gillespie and Pipes 1984; Gillespie and Carlsson 1988; Gillespie 1991). These studies show that sublaminate buckling is extremely sensitive to delamination size, depth, and laminate properties. Instability related delamination growth is governed by the interlaminar fracture toughness of the laminate. Conservative estimates for delamination growth are typically based on Mode I interlaminar fracture toughness, G_{Ic}. Residual compression strength is defined as the farfield stress at the onset of delamination growth. Alternatively, residual compression strength can be governed by in-plane membrane failure due to stress concentrations around the damaged area.

Many techniques have been investigated to improve interlaminar fracture toughness (G_{Ic}). Typically these techniques involve either material improvement or modification of the fiber architecture. Material improvements are made by improving the fracture toughness in the matrix material and the fiber-matrix interface bonding, since delaminations initiate and propagate through the matrix material and interface region (Kim and Mai 1998). Tough matrix materials, such as rubber-toughened epoxies and high-performance thermoplastics have been studied extensively. A comprehensive review may be found in several references (Kinloch and Young 1986; Kinloch 1986; Garg and Mai 1988). A technique called "interleaving" has also

8

shown much promise. In this technique, soft, tough strips of adhesive (or composite) are placed between laminar interfaces where delaminations are likely to occur (Kim and Mai 1998).

Due to the need for large allowable design strains and highly reliable aerospace structures, material improvement alone has been shown to be inadequate. The aerospace industry has looked at geometrical means of confining damage. In addition, modifications to the fiber architecture, such as by using through-thickness stitching reinforcement, are being investigated as an alternative means of improving interlaminar fracture toughness (Kim and Mai 1998). The effect of through-thickness stitching, particularly chain stitching, on damage tolerance of thick-section composites is examined in the present thesis.

In the late 1970s, Huang et al. (1978) introduced a method of improving local shear strength and reducing delamination growth in thin-section carbon/epoxy laminates. By inserting steel wires of a 0.33-mm diameter at ±45° to the laminate thickness and spaced 1.6 mm apart, Huang et al. (1978) were able to improve interlaminar shear strength by approximately 50%. However, the steel wires were required to be placed manually, and it was not until the mid 1980s that Mignery et al. (1985) investigated the possibility of stitching fiber thread into the carbon/epoxy laminate prior to curing (Dransfield et al. 1994). Under the National Aeronautics and Space Administration (NASA) Advanced Composite Technology (ACT) program, Hinrichs et al. (1995), Wang et al. (1996), Poe (1996), and Sankar (1996) have shown that stitching of thin-section carbon/epoxy laminates subjected to low-velocity impact may significantly improve failure loads to 90–97% of the ultimate design load.

As mentioned earlier, unstable delamination growth in a compressively loaded, impact-damaged laminate is governed by the Mode I and Mode II fracture toughnesses. Since conservative estimates for delamination growth are typically based on Mode I interlaminar fracture toughness, G_{IC}, previous research has focused on methods such as through-thickness stitching. Ogo (1987) was able to achieve a twelvefold increase in the Mode I fracture toughness when Kevlar stitching was used in thin-section graphite-epoxy laminates. Guenon (1988) has

shown that an addition of 1% volume fraction of through-thickness reinforcement results in a tenfold increase in Mode I fracture toughness of a carbon/epoxy orthogonal interlocked fabric composite. Morales (1990) has found that stitching improves G_{IC} up to 28 times, depending on stitch density and thread type as shown in Figure 1.
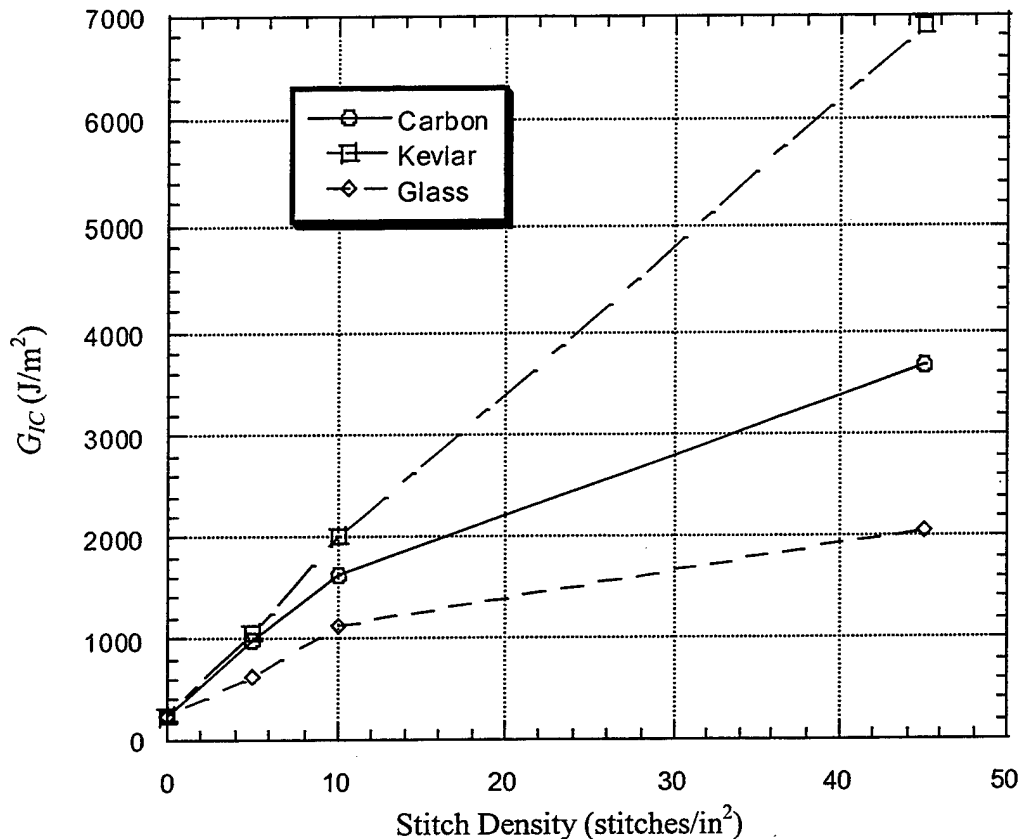
Figure 1. **Effect of Stitch Material and Stitch Density on Fracture Toughness. Material System Shown Is a Carbon T300-3K/Tactix 123 Epoxy Resin With a Baseline G_{IC} of 249 J/m^2.**

In addition to the effects of through-the-thickness stitching on residual strength, some recent work has been conducted to examine the effect of stitching on reducing impact damage size in thin-section carbon/epoxy laminates. Under the NASA ACT program, Portanova (1995) showed that stitching graphite composites can reduce the impact damage area by 35%. Adanur et al. (1995) demonstrated that too high of a stitch density caused excessive fiber breakage upon ballistic impact, while too low of a stitch density did not reduce damage size. In the present

study, the effect of stitching on reducing impact damage is also investigated, with a focus on thick-section glass-fiber-reinforced composites.

It has been shown that although stitching improves fracture toughness, it can reduce in-plane properties (Chou and Ko 1989; Dow et al. 1989; Liu 1990). A composite panel loaded in compression may suffer loss of strength due to stress concentrations that develop around the stitches. Thus, the benefit gained by stitching will depend on the role of fracture toughness on strength. Laminates that contain interlaminar defects and are loaded in compression typically fail due to delamination growth. Increasing fracture toughness will, in this case, lead to an improvement in strength. In addition, ballistically impacted panels develop multiple interlaminar defects (Zukas et al. 1982; Susuki and Takatoya 1997); therefore, stitching could serve to significantly improve residual strength, depending on what other forms of damage are present. In the present study, stitching of thick-section, S-2 glass-reinforced laminates will be investigated for their effect on damage resistance and compression after impact strength.

1.1.4 Damage Tolerance of Military Ground Vehicles. Most research to date on damage tolerance has focused on thin-section, carbon-fiber systems for aerospace applications. Recently, however, much interest has been generated in thick-section, glass-fiber-reinforced composites for military ground vehicle applications. Composites in combination with ceramics or conventional armor offer lightweight high-performance structures.

Significant differences exist in the design philosophy for combat vehicles compared to that for aerospace structures. Aircraft structures typically operate in extreme temperature conditions (between $-90°$ and $+350$ °F) and are designed to withstand only low-velocity impact. Combat vehicles operate under less extreme temperature conditions but must be able to tolerate high-velocity ballistic impact. In addition, manufacturing costs are more crucial, since the cost savings for weight reduction are not as high as the $500/lb estimated for aircraft (Thomas et al. 1994).

The Composite Infantry Fighting Vehicle (CIFV) developed by what is now United Defense Limited Partnership (UDLP) in 1986, demonstrated that the use of thick-section-composite structures on armored vehicles was feasible. By utilizing 65% by weight S-2 glass/CYCOM polyester prepreg composite material on the hull structure, a weight savings of 25% was obtained (Thomas et al. 1994). Further weight reductions could be made if improving damage tolerance could reduce the composite hull thickness requirements, via methods such as through-thickness stitching.

The Composite Armored Vehicle (CAV) program managed by the U.S. Army Tank-Automotive Research, Development, and Engineering Center (TARDEC) and contracted through United Defense Limited Partnership (UDLP) sought to further demonstrate the application of advanced composites to integrated structural armors for combat vehicles. The CAV employed a toughened epoxy resin system, rather than a polyester prepreg, to improve ballistic performance. Automated tow placement and hand-layup processes were used to manufacture the composite components.

One current goal is to reduce the manufacturing costs of future-generation lightweight combat vehicles—such as the Future Ground Combat System (FGCS)—by employing low-cost processes such as Seemann Composite Resin Infusion Molding Process (SCRIMP) (to be described in section 2) while maintaining the ballistic and damage-tolerant performance of previous-generation vehicles. In this work, the ballistic performance and residual strength of SCRIMP-processed panels is compared to those of panels manufactured using the CYCOM polyester prepreg, used on the CIFV. Panels are also made using low-cost 411-C50 vinyl-ester resin and compared to the more expensive SC-4-toughened epoxy system used on the CAV.

The U.S. Army Research Laboratory (ARL), in collaboration with the University of Delaware Center for Composite Materials (UD-CCM) and industrial partners, is working on the development of a multilayered, hybrid-composite ballistically resistant structures for military vehicles and other weapons platforms. Such an armored structure must be able to withstand

multiple impact hits and still maintain structural stability. A cross section of integral armor is shown in Figure 2. The thin outermost layer is a composite cover that provides protection against low-velocity impact and signature radiation. Alumina ceramic tiles provide ballistic protection by absorbing impact energy and shattering projectiles into small fragments. To increase multihit performance, a urethane rubber layer is placed behind the ceramic tiles to attenuate stress waves and keep adjacent tiles from debonding. Behind the rubber layer, a thick-section-composite layer is employed to increase ballistic protection and provide structural integrity.

Composite cover for
durability and signature

Alumina ceramic tiles
for ballistic performance

Rubber / urethane
layer for multi-hit
performance

Composite for structural layer

Phenolic liner for flammability
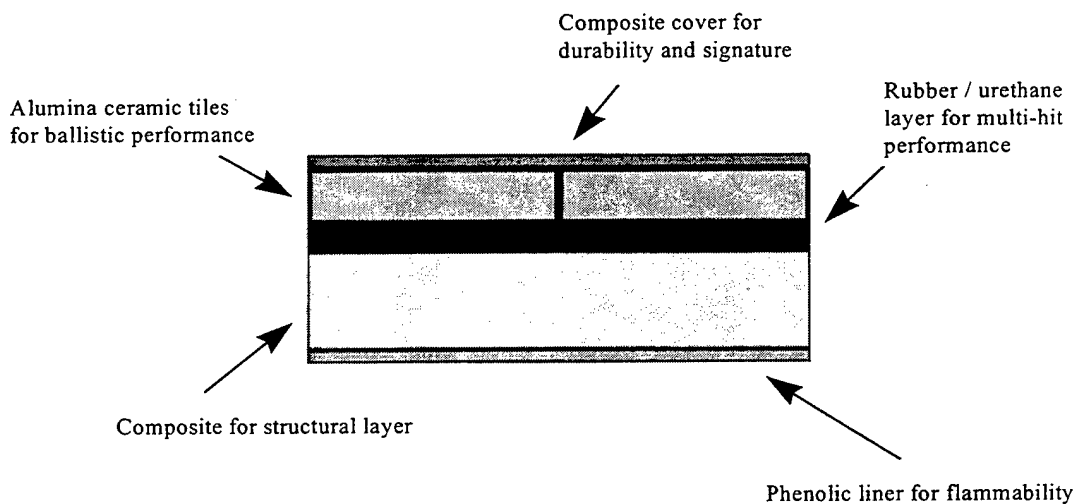
Figure 2. Cross Section of Integral Armor.

The structural layer is made of S-2-glass fibers and epoxy or vinyl-ester resin. This layer bears the majority of the structural loads and absorbs a significant amount of the impact energy (Figure 3). The final layer is a phenolic resin-based-composite liner that protects crew members from fire smoke and toxicity.

The focus of this research is on the damage tolerance properties of the thick section composite layer. The composite layer must be capable of sustaining multiple hit damage, while retaining sufficient residual compressive strength to satisfy design requirements. Other factors, or metrics, of performance of multifunctional composite integral armor are provided by Fink et al. (2000). The type of damage resulting from ballistic impact greatly influences the residual

Figure 3. **Ultrasonic Scan of an S-2 Glass/Vinyl Ester Structural Layer Subjected to Ballistic Impact. The Damaged Region at the Center of the Panel Consists of Delaminations, Matrix Cracks, Fiber-Matrix Adhesion Failure, and Fiber Breakage.**

strength behavior of the damaged part. As mentioned previously, there are two predominant post impact compression failure mechanisms in a composite part: membrane failure and delamination growth (Figure 4). Membrane failure (or in-plane failure) generally occurs when there is a loss of stiffness in the damaged area due to impact-induced matrix cracking and extensive fiber breakage (Wanthal et al. 1993; Tan 1994). Failure occurs when stress concentrations near the damaged region increase stress levels that exceed the undamaged strength of the material. A delamination growth-type failure occurs when local instabilities arise due to interlaminar defects. When a composite plate with an interlaminar defect is loaded in compression, residual stresses arise in the delaminated region. The result of these stresses is out-of-plane deformations of the local delaminated plies and a decreased axial stiffness of the buckled sublaminate. This, in turn, leads to Mode I (G_I) and Mode II (G_{II}) crack surface displacements at the interlaminar crack tip (Figure 5) (Gillespie and Carlsson 1991; Gillespie and Pipes 1984; Chai and Babcock 1985; Yin 1988).

The majority of techniques used to improve residual strength of ballistically impacted composites focus on improving fracture toughness. However, improving fracture toughness is beneficial only if the dominant failure mode is delamination growth. Delamination growth failure generally occurs when delaminations are present near the surface of the laminate. The

14

N_y

N_x

y, v

b

x, u

a

(a)   (b)
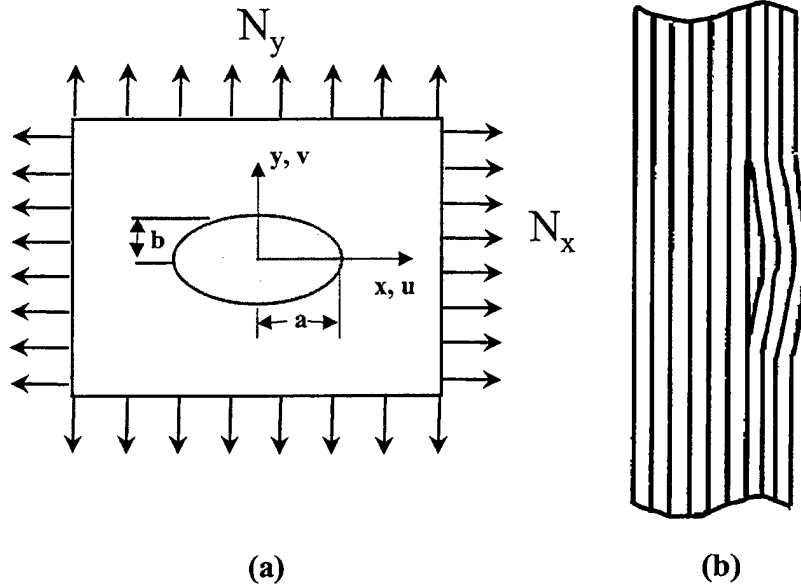
Figure 4. Two Failure Mechanisms: (a) In-Plane Failure Due to Stress Concentrations Around an Inclusion and (b) Unstable Delamination Growth Due to Interlaminar Defects.

L

D

A

b

L_T
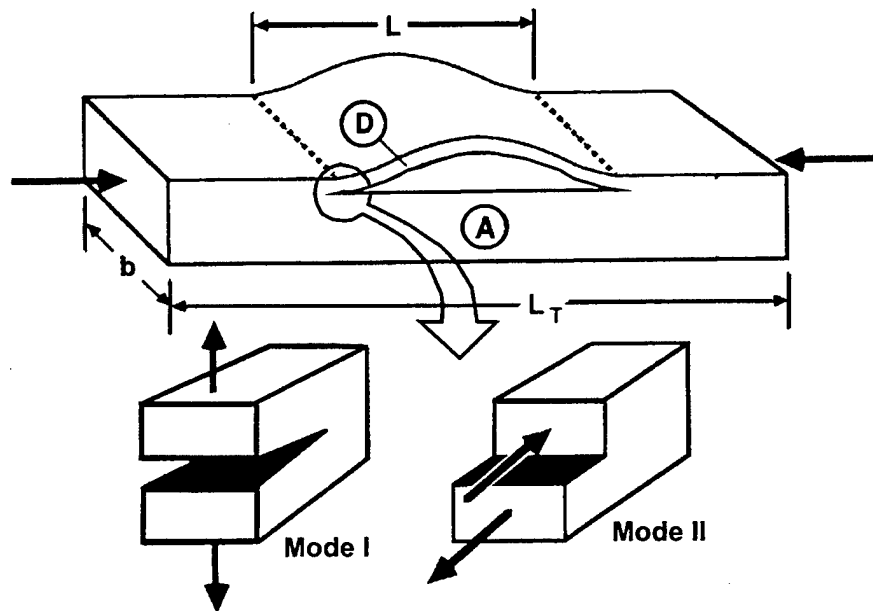
Mode I   Mode II

Figure 5. Composite Plate With an Interlaminar Defect. The Delamination Divides the Plate Into the (D) Buckled Sublaminate and (A) the Parent Laminate. At the Crack Tip, Normal and Shear Stresses Develop Causing Mode I and Mode II Crack Displacements, Respectively (Gillespie and Carlsson 1991).

instability of the sublaminate causes high out-of-plane stresses resulting in global failure. In the particular case of an impact-damaged panel, multiple delamination planes exist which allow an inner group of plies to grow as soon as the surface delaminations grow (Flanagan 1988).

Since membrane failure generally occurs when there is a loss of stiffness in the damaged region, a successful improvement in damage tolerance can be accomplished only by limiting the extent of fiber breakage. In the case of the CAV armor, this is achieved through the hybrid structure, in particular, through the addition of ceramic tiles (Figure 2).

Another important consideration for composite armor applications is multiple-hit performance. The size of the damaged region upon each impact should be small enough to reduce the likelihood of overlapping delaminated regions that could severely reduce residual strength. During ballistic impact, stress waves propagate through the thickness and reflect off the laminate back surface. Complex interlaminar stress fields develop that nucleate cracks that subsequently propagate as delaminations prior to arrest. As previously mentioned, the critical fracture toughness of the material controls the interlaminar crack propagation. By improving Mode I fracture toughness, it is postulated that damage size can be reduced and multihit performance improved. Mode I fracture toughness improvements are achieved in this study by using through-thickness stitching. However, it may be disadvantageous to increase fracture toughness to the point where the type of damage generated changes from multilevel delaminations to severe fiber breakage that causes membrane failure. Thus, an optimum fracture toughness value may exist, beyond which no strength improvement is gained.

1.2 Scope and Organization of Report. This work seeks to investigate the effects of the damage state on the residual compressive properties of various thick section laminates, both analytically and experimentally. In addition, means of improving multi-impact performance are experimentally tested. One such means is the use of relatively inexpensive 411-C50 vinyl-ester resin processed using the low cost SCRIMP method. Another means of improving ballistic tolerance is the use of through-thickness stitching to improve the effective fracture toughness of

16

the material. Both the SCRIMP process and through-thickness stitching are described in section 2.

In order to determine the type of damage seen in a ballistically damaged composite, nondestructive ultrasonic scanning is used as well as an experimental method by which damage is determined based on stress distribution. This information, coupled with analytical models and compression testing, will provide a more complete understanding of the residual strength behavior of ballistically damaged composites.

Three different resin systems, in conjunction with two fabric preforms, are investigated in this study for their ballistic and residual strength performance. The resin systems are: (1) CYCOM polyester used in the CIFV, (2) SC-4 epoxy used in the CAV, and (3) vinyl-ester 411-C50. The CYCOM polyester prepreg panels are manufactured using traditional manual layup, while the vinyl-ester and SC-4 epoxy panels are manufactured using the SCRIMP technique. The two fabric preforms used are 24-oz S-2 glass 5 × 5 plain weave fabric and an 18-oz S-2 glass 2 × 2 twill weave. In addition, through-the-thickness stitching is investigated as a means of improving both multihit performance and residual strength. An analytical model is proposed to examine the factors affecting residual strength, including damage size and type, fracture toughness, and stiffness loss. To account for certain geometrical effects, finite element analysis (FEA) is also used. From the combined analytical, FEA, and experimental study, a design chart is formed to determine the optimum improvement in fracture toughness attainable such that multihit performance and residual strength are maximized.

In section 2, some background material is presented. The first subsection of section 2 reviews the techniques used to manufacture and stitch the composite laminates. The SCRIMP technique is used prevalently, and a large industrial stitching machine was used to stitch the preforms in a square grid pattern with Kevlar thread. The second subsection describes the three different resin systems investigated and the relevant advantages and disadvantages of each. The third subsection describes the method used to ballistically impact the various laminates. The

final subsection gives an overview of the various NDE techniques available, with particular emphasis on ultrasonic scanning, which was the technique employed herein.

Section 3 provides the theoretical background necessary to model the compression strength behavior of impact-damaged laminates. An analytical model is proposed that combines instability-related delamination-growth criteria and Lekhnitskii's analysis for in-plane failure to predict compression after impact strength for given damage sizes and locations through the thickness. The effect of finite width on stress distribution is also examined using finite element analysis. The Compression Strength of Delaminated Structure (CSDS) program (Wanthal et al. 1993), which employs the analytical failure criteria, is then evaluated for a case study of thick-section S-2 glass/polyester systems containing multiple delaminations resulting from ballistic impact. The model is also verified experimentally and numerically for thin-section carbon/epoxy laminates. From the case study and CSDS/FEA analysis presented in section 3, it was concluded that further experimental work was needed to determine the CABI modes of failure.

In section 4, such experimental work is presented. In addition, experiments have been carried out to determine the effect of through-thickness stitching and ceramic tiles on arresting damage development upon ballistic impact and on improving residual strength. Three different resin systems were investigated for their ballistic performance in various combinations with two different S-2 glass fabrics. The SCRIMP process is compared to the manual layup of CYCOM polyester prepreg in light of ballistic performance and CABI strength. The normal stress distribution under compression loading is also examined in order to determine the degree of stiffness loss in the damaged region. This was done in an effort to determine the CABI failure modes.

Section 5 presents a parametric study that seeks to examine how the predominant modes of failure and the CAI strength vary as a function of fracture toughness, in-plane stiffness, and

geometrical effects. From this study, recommendations are made in order to optimize multihit ballistic performance and residual strength depending upon threat level.

Section 6 summarizes the main conclusions of this study and presents suggestions for areas where there is potential for future work. Finally, an appendix is included that contains additional experimental data not presented in section 4.

2. Background on Processing, Materials, and Testing

2.1 Introduction. In this section, a brief summary will be given of processing, materials, and test techniques used in this study. Section 2.2 will discuss two molding processes and through-the-thickness stitching techniques. The first molding process, resin-transfer molding (RTM), has been in use for over two decades. The second molding process, a variation of the RTM process called Seemann Composite Resin Infusion Molding Process (SCRIMP) (Seemann 1990), is relatively new. For the most part, composite panels tested in this study were manufactured using the SCRIMP process. Section 2.3 discusses the various material systems used to produce various thick-section composite panels in this thesis along with the relative advantages and disadvantages of each system. Section 2.4 will describe the method used to ballistically impact the panels. In section 2.5, the prevailing techniques used to nondestructively evaluate internal damage after ballistic impact will be summarized.

2.2 Manufacturing Techniques.

2.2.1 RTM. In RTM a preform is placed within a mold cavity, the mold is closed, and a thermosetting resin is injected using positive pressure (Strong 1989). Resin enters through one or several injection gates while excess resin and air exit through vent gates (Figure 6). In some instances, a vacuum is applied at the vent gates to help speed the RTM process and to aid in the removal of trapped air to reduce void content. In this process, the resin typically flows in the plane of the preform with uniform wetting of the preform through the thickness.

19
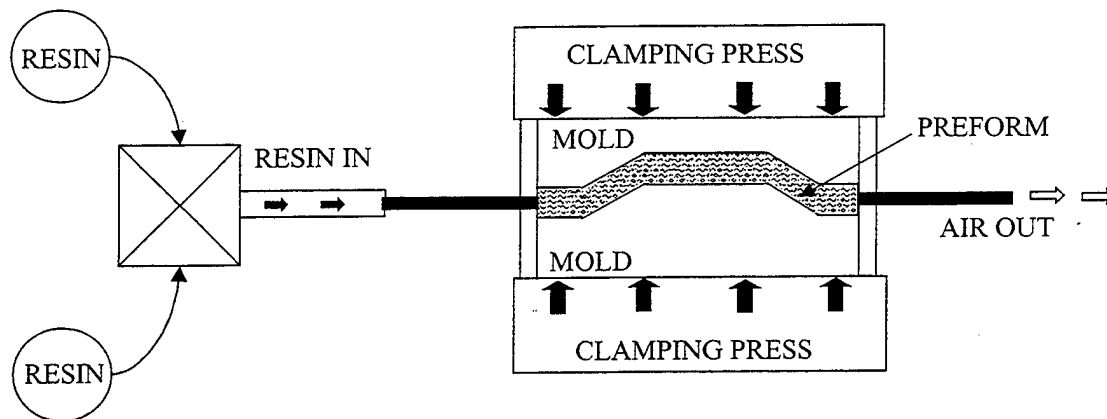
Figure 6. Schematic Diagram of the RTM Process.

The RTM process works with most standard reinforcement materials. The main requirement is that the reinforcement material retains its shape during injection. Typically, the reinforcement material is stitched around the periphery or bonded with a water-soluble binder to maintain near-net shape during injection.

The viscosity of the resin should be low enough that the fibers may be easily wetted. Normally, resin viscosities are below 500 cP. In some cases, the resin is heated to reduce viscosity and injection pressure. In addition to low viscosity, the resin should have a pot life much longer than the fill time so that the injection will fully wet out the fiber preform prior to gelation (Strong 1989).

Critical to the RTM process is the mold design. The mold should be designed such that resin may reach all areas of the cavity to avoid defects such as dry spots or regions of high-void content. RTM molds may be made of various materials depending on the temperature and processing requirements needed to cure the resin. For high-volume, high-temperature production, steel is the material of choice. For low-volume production not exceeding 2,000 parts and low temperature, fiberglass/epoxy molds may be used. Fiberglass/epoxy molds offer the advantage of low cost and relative ease of manufacturing. The advantages and disadvantages of the RTM process when considered against alternate manufacturing processes are tabulated in Table 1.

Table 1. Advantages and Disadvantages of the RTM Process

Advantages	Disadvantages
• Efficient and inexpensive production of large complex parts.	• Mold design is difficult. Problems arise with dry spot formation due to poor distribution of resin.
• Excellent surface finish and tight tolerances.	• Parts typically have lower fiber volume fraction than parts made through autoclave processing.
• Short production times compared to manual layup.	• Fiber movement during resin injection sometimes occurs.
• Good reproducibility.	• High injection pressure requires more costly tooling.
• Process automation is possible.	• Scalability is limited.

2.2.2 SCRIMP. The SCRIMP process, developed by William Seemann in the late 1980s (Seemann 1990), utilizes vacuum pressure alone for resin infusion. Unlike the RTM and vacuum-assisted resin-transfer molding (VARTM) processes, which use a two-sided mold, the SCRIMP process uses only a one-sided mold (Figure 7). The fiber preform is placed on a mold surface that is typically coated with a release agent to keep the final part from sticking to the mold. A layer of peel ply is placed on top of the fiber preform. On top of the peel ply is a layer of distribution medium, slightly smaller than the preform. The distribution medium is a highly permeable material that serves to increase the speed of resin flow across the surface of the preform while simultaneously wetting out the preform thickness. Two tubes are placed along opposite sides of the part. On one side of the part, the tube is connected to a vacuum pump. This is often termed the "vent/bleeder" tube. On the opposite side, the tube is placed within the resin source. This is called the "injection/feeder." The entire preform is then placed beneath a vacuum bag, and a vacuum is applied.

As the vacuum is applied, the preform compacts, a pressure gradient is produced in the closed system, and the resin flows through the feeder tube, and the fiber preform, and out the bleeder tube at the opposite side (Figure 8). The SCRIMP process offers many advantages over the RTM process, primarily low-cost tooling, scalability and affordability (Table 2). The SCRIMP

21

resin injection

fiber preform
under vacuum

Lay-up detail

vacuum pump

vacuum bag

distribution media

peel ply

fiber preform

mold
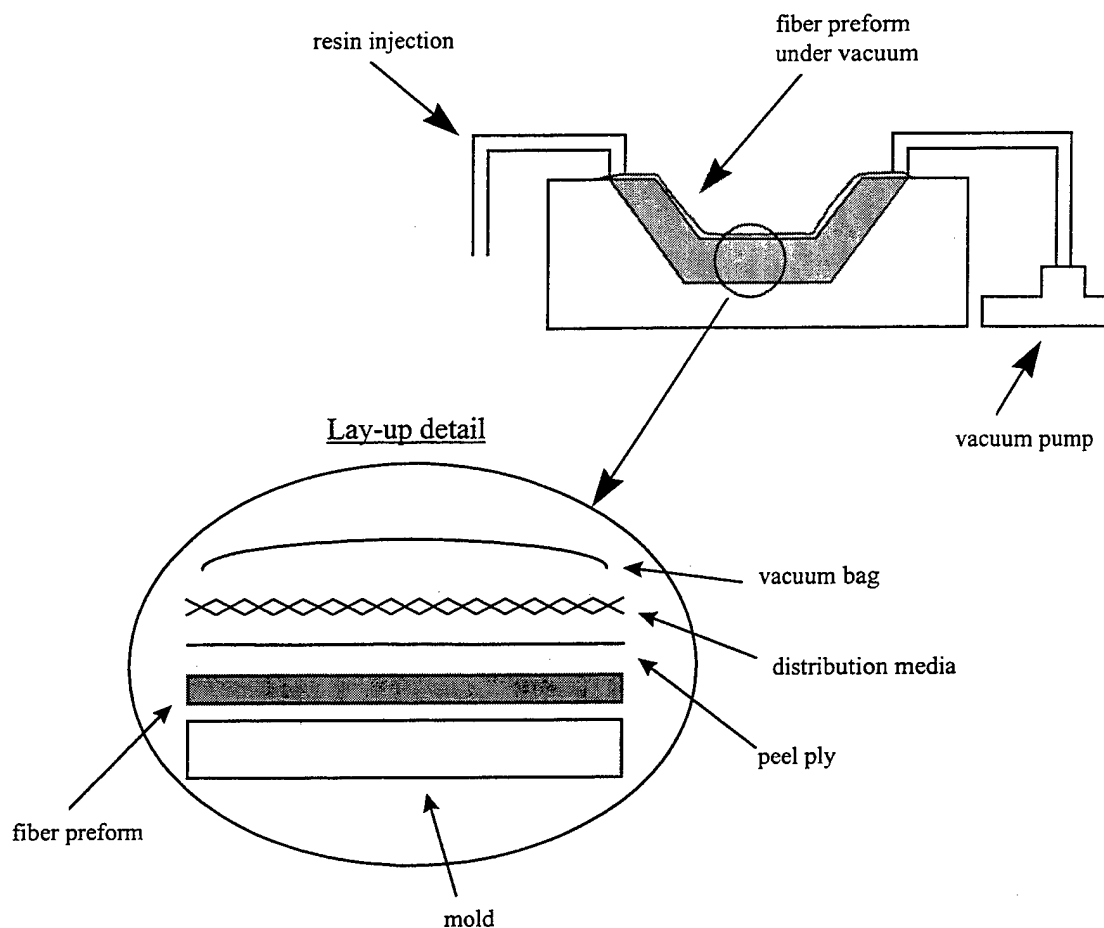
Figure 7. Schematic Diagram of the SCRIMP Process.

process will be used extensively in the experimental study presented in this report, along with manual layup. In this study, the SCRIMP process was used to manufacture 30.48-cm × 30.48-cm × 1.78-cm (12 in × 12 in × 0.7 in) panels.

2.2.3 Preform Description. Two different preforms were used to manufacture the panels in combination with two different resin systems: Applied Poleramic SC-4 epoxy, and DOW Derakane 411-C50 vinyl-ester resin. One of the preforms used was made from an 18-oz S-2 glass 2 × 2 twill weave, while the other preform was a 24-oz, S-2 glass 5 × 5 plain weave (Figure 9). The manufacturer's fabric designation of 24 oz or 18 oz indicates that the fabric
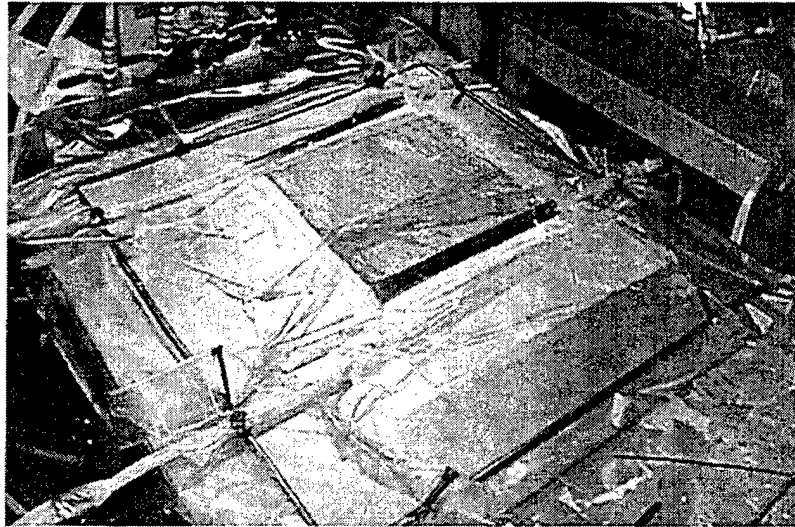
Figure 8. Completed SCRIMP Layup Under Vacuum Prior to Resin Infusion.

Table 2. Advantages and Disadvantages of the SCRIMP Process

Advantages	Disadvantages
• Need only one-sided mold.	• Difficult to automate.
• Quick infusion time of large parts.	• Resin system must have low viscosity.
• Good part quality, high-fiber volume fraction.	• Bag side of part does not have good surface finish.
• Low-cost tooling.	• Difficult to obtain tight tolerances.
• Environmentally safe due to low volatile organic compound (VOC) emissions.	
• Scalable to large structures.	
• Affordable.	

weighs 24 oz/yd^2 and 18 oz/yd^2, respectively. With the SCRIMP process, final parts achieved an average fiber volume fraction of 47%. Stitching the preforms through the thickness with Kevlar thread increased compaction and fiber volume fraction to 55%.

A set of panels was also made by hand layup of 24-oz plain weave S-2 glass/polyester CYCOM 4102 prepreg. Section 4 summarizes the different panel types tested.
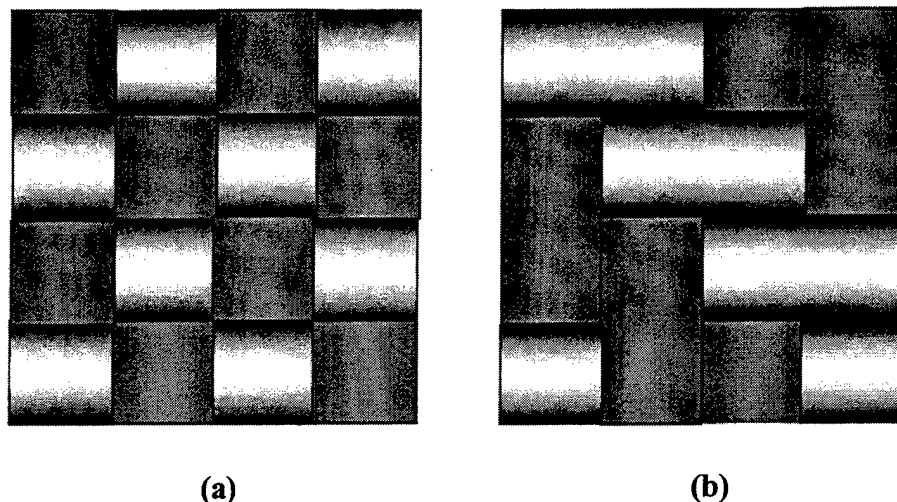
Figure 9.   Schematic Diagram Showing Fabric Weave for (a) 5 × 5 Plain Weave and (b) 2 × 2 Twill Weave.

2.2.4   Through-the-Thickness Stitching.   Previous work has shown that stitching a fiber perform before injecting resin can significantly improve the fracture toughness of the resulting part (Dransfield et al. 1994). In this study, stitching will be used to examine its effect on improving residual strength after ballistic impact. It has also been postulated that stitching has the added benefit of reducing damage size upon projectile impact.

A large variety of stitch geometries exist in the textile industry. One type of stitch pattern mainly used in the apparel industry is called a "lock stitch." To form a lock stitch, a two-thread loop is formed between the needle and the bobbin (Figure 10). This requires that both the top and bottom of the laminate be accessible. The loop generated between the bobbin and needle is generally placed within the center of the part for aesthetic reasons.

For composite applications, this is not desirable since the loop may create internal stress concentrations. Thus, for structural applications, the loop is usually brought to the surface of the part. This is done by adjusting the tension on the sewing machine such that the needle thread is forced to travel to the top surface of the panel (Morales 1990). This is called a "modified lock stitch" (Figure 11).

24
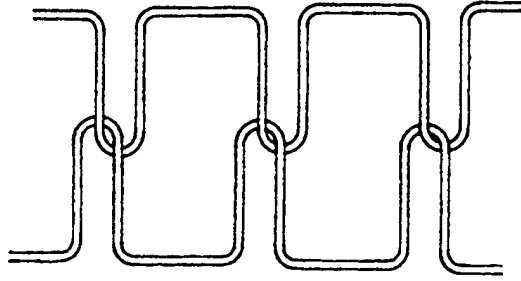
Figure 10. Lock Stitch.
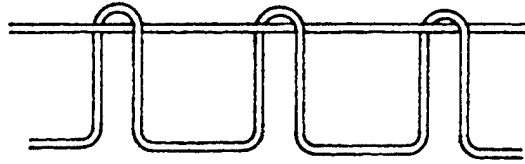
Figure 11. Modified Lock Stitch.

Another commonly used stitch geometry for structural applications is called the "chain stitch." In this method, a single yarn moves with the needle from the top of the panel to the bottom and back again to the top. The thread loops around itself in the process as shown in Figure 12 (Dransfield et al. 1994). Due to its availability, the stitched panels manufactured in the present study were made using a chain-stitch sewing machine.
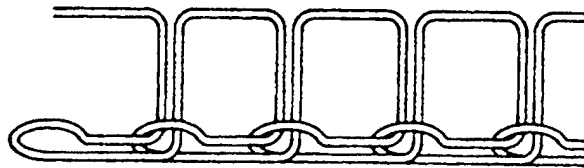
Figure 12. Chain Stitch.

In addition to choosing an appropriate stitch geometry for structural applications, the thread material used should be extensible and resistant to abrasion so that it will not break as it bends and passes through the needle. This is particularly true for stitching prepreg as opposed to resin-free fabric (Lee and Liu 1990). Dow and Smith (1989) reported that glass, Kevlar, and carbon fibers are effective in this regard. Twisting of two or more thread yarns is usually

necessary when stitching to avoid snagging of the thread as it passes through the needle eye. However, twisting thread leads to a reduction in the tensile strength of the thread. Morales (1990) has found that thread twisting can reduce the strength of Kevlar thread by 35% and carbon fiber by 80%. Because of the high tensile strength of Kevlar fiber and its superior performance in thread form, Kevlar was selected in the current investigation.

Liu (1990) and Dow and Smith (1989) have shown that the stitch pattern can affect the shape of the delamination, although the pattern does not seem to have a significant effect on the delamination area. However, it was previously shown (Liu 1990) that stitch density (stitches/in^2) reduces delamination area. Work done by Liu on thin-section composites has also shown that damage area can be reduced as much as 40% by increasing stitch density fourfold.

Stitched panels manufactured for this study have a stitch density of 25 stitches/in^2. The chain-stitch pattern was a regularly spaced grid pattern with a 1-in spacing between stitch rows (Figure 13). A MIL-T-87128 (Department of Defense 2000), 5-ply (yarn), soft, Kevlar thread of 2000 denier was used as the stitching material. Table 3 summarizes the properties of the Kevlar thread used.
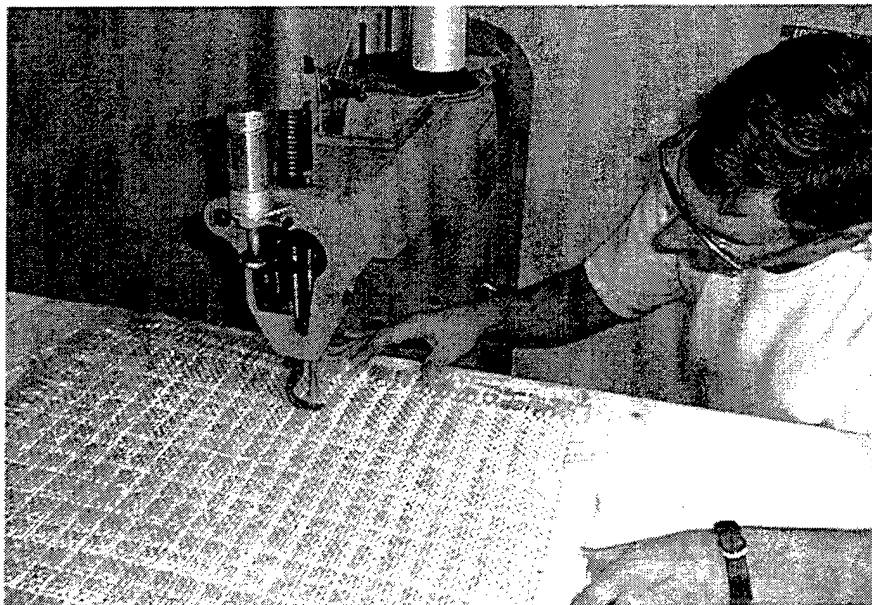
Figure 13. Stitching of S-2 Glass Preform Using Puritan Chain-Stitch Machine.

Table 3. **Kevlar Thread Properties (Based on Military Specification MIL-T-87128 [Department of Defense 2000])**

Yarn Denier (per ply)	Number of Plies	Twist (per inch)		Length (per lb) (yd)	Breaking Strength (lb)
400	5	10s[a]	5z[a]	2,000	80

[a] Indicates the type of twist as explained in the literature (Morales 1990).

It has been shown that although stitching improves fracture toughness, it can reduce in-plane properties (Chou and Ko 1989; Dow et al. 1989; Liu 1990). A composite panel that is loaded in compression may suffer loss of strength due to stress concentrations that develop around the stitches. Thus, the benefit gained by stitching will depend on the role of fracture toughness on strength. Laminates that contain interlaminar defects and are loaded in compression typically fail due to delamination growth. Increasing fracture toughness will, in this case, lead to an improvement in strength. It has been shown that ballistically impacted panels develop multiple interlaminar defects (Zukas et al. 1982; Susuki and Takatoya 1997). In such a case, stitching could serve to improve residual strength significantly, depending on what other forms of damage are present. Figure 14 shows the effect of increasing fracture toughness on microstrain-to-failure for delamination type damage of various sizes for an S-2 glass/polyester prepreg panel. Moderate improvements in fracture toughness are shown to significantly improve strain to failure. Use of through-the-thickness reinforcement has been shown to improve G_{IC} values up to 25x, depending on stitch density, in thin-section carbon/epoxy composites (Morales 1990). In the present study, stitching of thick-section, S-2 glass-reinforced laminates will be investigated for their effect on compression after ballistic impact strength.

2.3 Material Systems. In this study, VARTM epoxy and vinyl-ester resins were studied and compared to polyester prepreg baseline.

2.3.1 Epoxies. Epoxies are used extensively in high-performance aerospace composites applications. Epoxy systems demonstrate excellent mechanical properties, as well as good

Figure 14. Effect of Fracture Toughness (G_{IC}) on Residual Strength (Huang 1998).

moisture, chemical, and thermal resistance. They also demonstrate excellent adhesive properties to a large variety of substrates and have high-fracture toughness as compared to vinyl-ester and polyester resins. However, epoxy resins are typically expensive, have high cure temperatures, and release toxic fumes.

The epoxide ring characterizes epoxy resins. Figure 15 shows the molecular structure for a typical di-functional epoxy prepolymer. The average molecular weight of the prepolymer depends on the number of repeat units in the backbone of the chain, n. The value of n normally ranges from 0 to 2 (Ziaee 1999). Most commercially available resins are based on polyhydroxyphenol, otherwise known as Bisphenol A (Figure 15). The epoxy resin is cured via a step-polymerization mechanism in which a curing agent reacts with the epoxide ring.

Figure 15. Molecular Structure of an Epoxy Compound (Ziaee 1999).

28
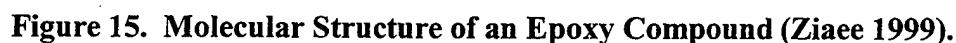
Two common curing agents used with epoxy resins are amines and anhydrides. Figure 16(a) shows a commonly used amine-curing agent known as "PACM20." This compound contains two primary amines, which can react with four epoxide groups. Figure 16(b) shows the chemical structure of an acid anhydride. In this compound, the hydroxyl group of acetic acid is replaced by the entity encircled by the dashed line. Acid anhydrides can react with the end epoxide groups and hydroxyl groups along the epoxy resin molecule.

$$NH_2-CH_2-NH_2 \qquad\qquad CH_3-\overset{\overset{\textstyle O}{\|}}{C}-O-\overset{\overset{\textstyle O}{\|}}{C}-CH_3$$

(a)   (b)
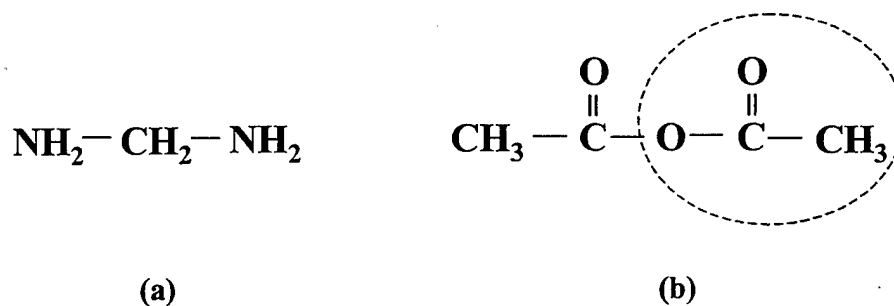
Figure 16. Two Common Curing Agents: (a) Amine and (b) Acid Anhydride.

VARTM epoxies are being developed. These epoxies typically have low viscosity to enable room-temperature processing and typically have lower mechanical properties and glass-transition temperature compared to aerospace-epoxy systems.

In this particular study, an acrylated epoxy resin developed by Applied Poleramic, Inc. called SC-4 was used. SC-4 is a three-part resin system. Part A is an epoxy resin consisting of Diglycidylether of Bisphenol A (50–75%), shown in Figure 16, and multifunctional epoxy resins (25–50%). Part B is an acrylic modifier consisting of various methacrylate monomers. Part C is an epoxy hardener containing primary amine adduct (80–90%), piperazine amine adduct (2–10%) and heterocyclic catalyst (2–10%). The ratio of A:B:C is 100:80:20. A typical processing cure cycle for SC-4 epoxy is shown in Figure 17. SC-4 epoxy has a viscosity between 200 and 300 cP at 25 °C and a glass-transition temperature (T_g) of 93 °C.

2.3.2 Vinyl Ester. Most commercial vinyl-ester resins are a mixture of styrene and a methacrylated bisphenol-A-based compound. This methacrylated compound is made from

29
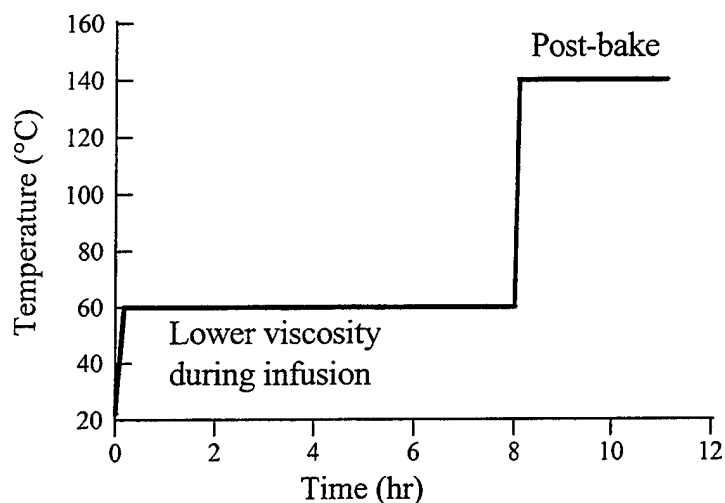
Figure 17. Cure Cycle for SC-4 Epoxy Resin.

reaction between epoxy resins, and methacrylic acid, similar to that shown in Figure 15. For lack of proper nomenclature, this methacrylated compound is referred to as a vinyl-ester molecule. The schematic of a typical vinyl ester is shown in Figure 18. The group R in the bracket is very similar to the epoxy molecule shown in Figure 15.

$$
\begin{array}{ccc}
CH_3 & & CH_3 \\
| & & | \\
CH_2{=}C{-}C{-}O{-}[R]{-}O{-}C{-}C{=}CH_2 \\
\ \ \ \ \ \| & \ \ \ \ \| \\
\ \ \ \ \ O & \ \ \ \ O
\end{array}
$$
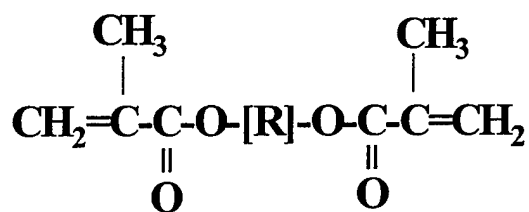
Figure 18. Molecular Structure of Vinyl-Ester Compound.

The goal in synthesizing such a resin was to obtain the superior properties found in epoxy resins while retaining the ease of processing found in polyester systems. Because of this successful combination, vinyl esters have been gaining in popularity. The properties of vinyl-ester resins are generally better than those of polyesters, and they are more affordable than most epoxy systems.

30

Once the vinyl ester is made from the reaction previously described, it is then combined with a reactive diluent (styrene) to lower its viscosity. Commercially available resins typically come as 20–50 weight-percent styrene. Vinyl-ester resins cure through free-radical polymerization. The initiator used in this work is Trignox 239A, which contains 45 weight-percent cumyl hydro peroxide (CHP). An accelerator, cobalt naphthanate (CoNap) 6% is also used in conjunction with Trignox. The weight-percent of Trignox and CoNap is 2% and 0.2%, respectively. A detailed study of vinyl esters and their cure cycles is presented by Stone (1997). A typical cure cycle for vinyl ester 411-C50, which is the system used in this study, is shown in Figure 19. Vinyl ester 411-C50 has a viscosity of 100 cP at 25 °C and a T_g of 122 °C.
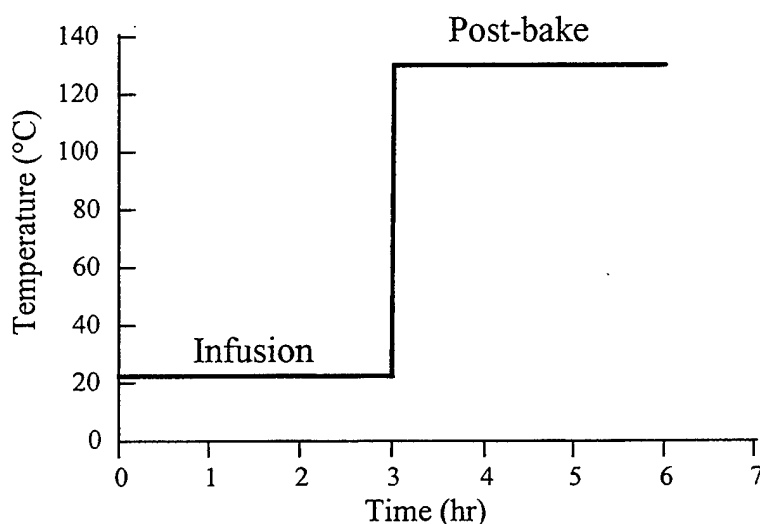
Figure 19. Cure Cycle For Vinyl-Ester 411-C50.

2.3.3 Polyester. Polyester resins have become a widely used resin system due to their ease of manufacturing, low cost, high-rate/low-temperature cure, and good chemical and moisture resistance. However, a major drawback of polyester resins is their high flammability and smoke toxicity upon combustion. In addition, the properties of polyester resins are not as good as those of epoxy resin systems. Polyester resins are used in a variety of applications. The marine industry uses polyester resins for their high-moisture resistance. The consumer goods industry uses such resins for household appliances and business machines due to their low cost and ease

of manufacturing. A growing market for polyester resins is to be found in the transportation industry (Gum et al. 1992).

Unsaturated polyester resins are composed of alkyd polyester (Figure 20) and a monomer (usually styrene) that acts as a reactive diluent. Other chemical agents such as inhibitors, promoters, and peroxide catalysts can be added to the resin to control cure time. The resin cures through free-radical polymerization. Cure starts when the peroxide catalyst is added. The catalyst causes the polyester alkyd to cross link with the styrene to form a three-dimensional (3-D) network. No byproducts are generated in the process, which simplifies the manufacturing process since byproducts require removal and elimination.

$$\text{H-[O-C-CH=CH-C-O-CH}_2\text{-CH}_2]_n\text{-OH}$$
$$\overset{\|}{\text{O}} \qquad\qquad \overset{\|}{\text{O}}$$
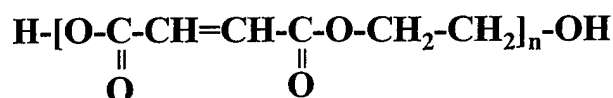
Figure 20. Molecular Structure of Unsaturated Polyester (Gowariker et al. 1986).

In this study, CYCOM 4102 polyester resin is used in prepreg form. The cure cycle is shown in Figure 21. The polyester resin has a viscosity of 200–300 cP at 80 °C and a T_g of 138 °C.
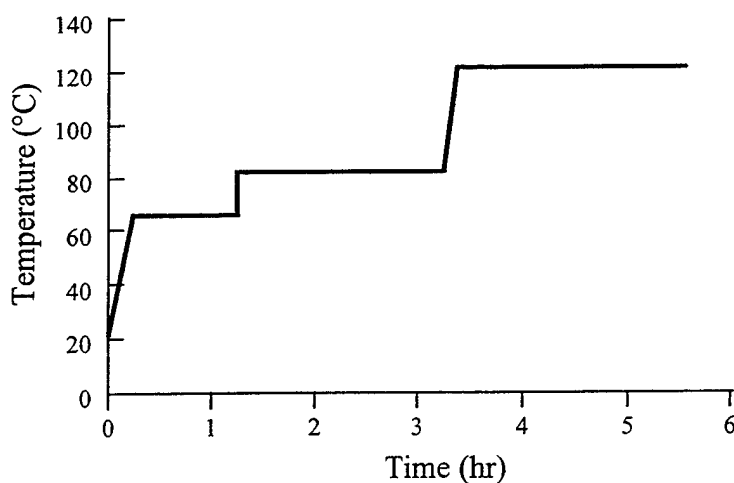
Figure 21. Cure Cycle for CYCOM 4102.

32

Table 4 summarizes the relative advantages and disadvantages of the three resin systems previously described. In this study, laminates manufactured with polyester resin are made by manual layup of S-2 glass fabric pre-impregnated with uncured polyester. Laminates manufactured using the vinyl-ester and SC-4 resins were made by the SCRIMP process.

Table 4. Thermoset Resin Comparison (Gillio 1997)

Resin System	Advantages	Disadvantages
Polyester CYCOM 4102	• Low cost. • Easy to process. • Good chemical and moisture resistance. • Fast cure time. • Room-temperature cure.	• Flammable. • Toxic smoke upon combustion. • Average mechanical properties.
Vinyl ester VE 411-C50	• Low Cost. • Ease of processing. • Low viscosity. • Room-temperature cure. • Moisture resistant. • Good mechanical properties.	• Flammable. • Smoke released upon combustion. • Mechanical properties not as good as epoxies.
Epoxy SC-4	• Excellent mechanical properties. • Good chemical and heat resistance. • Good adhesive properties with a large variety of substrates. • Moisture resistant. • Variety of compositions available. • Good fracture toughness.	• Expensive. • Requires high processing temperatures to achieve good properties.

2.4 Ballistic Testing. To test the performance of panels subjected to high-velocity impact and to measure their residual strength, ballistic tests were carried out. Initially, impact testing was performed using a drop tower in which a weight is suspended from a certain height and then dropped to cause damage. The weight and height can be adjusted to the desired energy level, depending on the thickness and layup of the material. This method is advantageous in that it

allows for controlled, repeatable impact energies. However, it was not possible to achieve the desired severity of damage with the drop tower. Instead, panels were impacted ballistically. Although the energy level cannot be as accurately controlled with ballistic testing, it is more representative of the type and severity of damage that would be seen under real conditions.

Normally, composite plates are used as the structural backing layer in an armor structure. Thus, an impact event would most likely cause severe delaminations. In order to simulate this effect with a projectile, the impact velocity, and consequently the impact energy, must be carefully selected. The impact velocity must be high enough to cause large delaminations but not so high that the projectile passes cleanly through the laminate. In order to determine the proper speed, V50 ballistic-limit tests were performed. The V50 ballistic limit represents the velocity at which complete penetration of the laminate by the projectile is likely to occur with a 50% probability (U.S. Army Research Laboratory 1987). The V50 values for the polyester and epoxy resins were determined by Fink and Gillespie (to be published) using a .50 cal. fragment simulating projectile (FSP) fired from rifled barrels 8 ft (2.44 m) in length. Testing was done in accordance with NIJ Standard 0101.03 (U.S. Department of Justice 1987) (Figure 22) on panels 30.48 cm × 30.48 cm × 1.78 cm (12 in × 12 in × 0.7 in) in dimension. For polyester systems, the V50 value was determined to be 1,770 ft/s; for the SC-4 epoxy resin, the V50 was 1,740 ft/s. The V50 for the vinyl-ester systems was approximated to be the same as the polyester systems. This is a reasonable assumed, considering the similarities in material properties between the two systems. Since the objective in this study was to cause damage without perforation, a velocity of 1,550 ft/s was chosen for constant velocity testing. Due to the light powder charge in the projectile case, velocity varied somewhat. Standard deviation in velocity was approximately 100 ft/s. Tables 5 and 6 summarize the results of the V50 testing for the SC-4 and polyester panels reported by Fink and Gillespie (2000). The V50 tests demonstrate the comparable ballistic performance of VARTM-manufactured panels to that of the polyester CYCOM prepreg panels at reduced cost.

34

A - 5 m

B - 2 m

C - 1.0 m
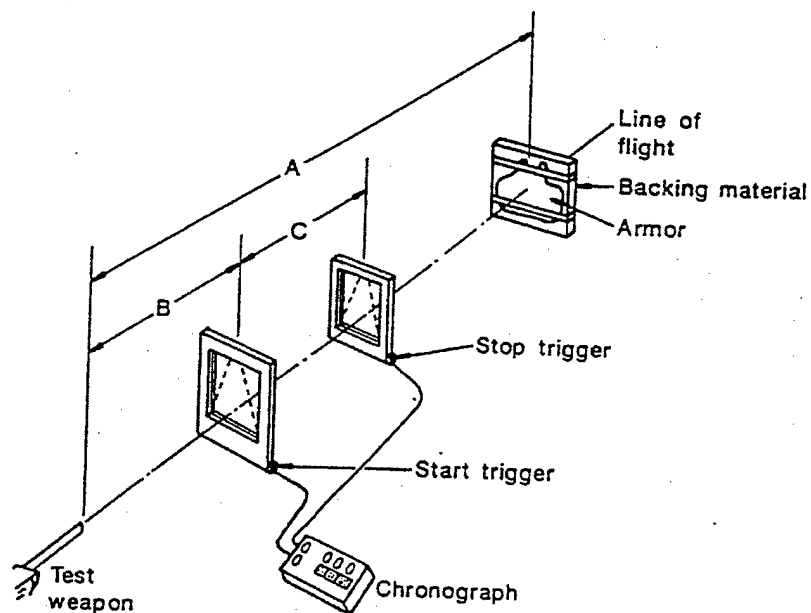
Figure 22. Schematic of Ballistic Test Setup. The Start Trigger and Stop Trigger Are Placed in the Line of the Projectile Attached to a Chronograph to Measure Velocity (U.S. Department of Justice 1987).

Table 5. V50 Test Results for SC-4 Panels

Panel No.	Areal Density (lb/ft^2)	Velocity (ft/s)	Comments
SC-4-1	6.9	1,729	Incomplete Penetration
SC-4-2	6.9	1,536	Incomplete Penetration
SC-4-3	7.0	1,749	Complete Penetration
SC-4-4	6.9	1,685	Incomplete Penetration
V50: 1,740			

2.5 NDE.

2.5.1 X-ray Computed Tomography (CT). X-ray computed tomography (CT) has developed rapidly in the past two decades as a powerful NDE tool. CT uses radiation to image

35

Table 6. V50 Test Results for Polyester CYCOM Panels

Panel No.	Areal Density (lb/ft^2)	Velocity (ft/s)	Comments
CYCOM-1	7.0	1,729	Incomplete Penetration
CYCOM-2	7.0	1,776	Partial Penetration (hit witness plate)
CYCOM-3	7.0	1,808	Complete Penetration
CYCOM-4	7.0	1,663	Incomplete Penetration
V50: 1,770			

cross-sectional slices of an object. Unlike conventional x-ray projection radiography, CT produces clear images of an interior plane of an object, without the confusion of intermediate material. CT scans can be used for either qualitative analysis of material features or quantitative measurements of material density at discrete volume elements within the part.

Standard x-ray techniques yield shadowgraph images that require extensive interpretation. CT uses computer reconstruction to combine information from multiple radiographic images, thus giving a detailed quantitative analysis of the part (Bossi et al. 1990). The CT data is displayed as a reconstructed slice of a plane of the part where the data values from the image are proportional to the spatial electron density distribution in each volume element of the slice.

X-ray CT scans can be used for a variety of applications. One of the major applications of CT is the determination of bulk density. This is important, since density is often directly related to physical properties such as material strength, porosity, and fiber volume fraction. CT scans can also be used to determine density gradients, which consequently allow for the detection of cracks and delaminations. Another application of CT lies in the system's ability to obtain dimensional information. This can be useful for design evaluations and verification of theoretical engineering models. 3-D images can be quickly formed by combining images of individual slices. This is already being used extensively in the medical industry to develop images of the brain, spine, and body.

The x-ray CT technique was used in the case study presented in section 3. Thick-section-composite polyester panels were ballistically impacted and the percent area of damage at 2-mm slice intervals was determined.

2.5.2 Ultrasonic Scan. Ultrasonic inspection techniques are beneficial for flaw detection in a variety of materials, including fiber-reinforced-composite materials. Material flaws such as cracks, delaminations, and voids can be detected via this nondestructive technique. In addition, ultrasonic scans can be used to determine fiber orientation, measure changes in thickness, and determine elastic properties.

Ultrasonic inspection of homogeneous materials such as metals has been extensively studied, and the techniques of inspection are well developed. However, nonhomogeneous materials such as composite materials are more complex to analyze. It is often difficult to correlate ultrasonic data to specific flaws, and producing repeatable results can be troublesome (Blake and Pipes 1990).

Ultrasonic NDE employs acoustic energies to inspect materials, with frequencies greater than the audible range (15 kHz). The sound energy is directionally focused on the material to be inspected. The ultrasound energy travels through the material under inspection, and a complex interaction takes place with the material's microstructure (Blake and Pipes 1990). The energy wave is then reflected when the acoustic wave encounters areas of the sample where the acoustic properties vary, typically as the result of density changes. The sound source is usually coupled to the material with water due to water's high efficiency in transmitting high frequency sound energy. From the resulting information obtained on changes in wave amplitude and velocity, an evaluation can be made about the material structure. The methods used to evaluate and analyze the ultrasonic information comprise the bulk of the task involved with NDE evaluation. Much research to date has been performed in analyzing NDE data to obtain both higher resolutions in flaw detection, and faster detection times.

In the present study, a type of ultrasonic scan called a "C-scan" was used to analyze damage in the ballistically impacted panels. The C-scan is mainly a way to detect large defects within the

material, such as inclusions and delaminations. C-scans are two-dimensional (2-D) views of the interior structure of the material. Defects show up as color variations in the image. The C-scan collects three values for each point on the sample: x coordinates, y coordinates, and a gray-scale value corresponding to the quality. A focused ultrasonic transducer rasters over the specimen surface with the aid of two sets of screw drives mounted perpendicular to each other. While the transducer scans the part, data is being collected at discrete distance intervals through thickness. The result is a series of 2-D images, with defects appearing as variations in image intensity (Fecko 1996).

The specified region of the total ultrasonic waveform at a particular depth is called the "gated region" and is shown in Figure 23. The interface delay is a function of the speed of sound and thickness of the material, and the front surface delay is a function of the focal length of the transducer. The gate delay is triggered from the front surface echo to compensate for surface and thickness irregularities, as well as warpage (Pipes et al. 1990).
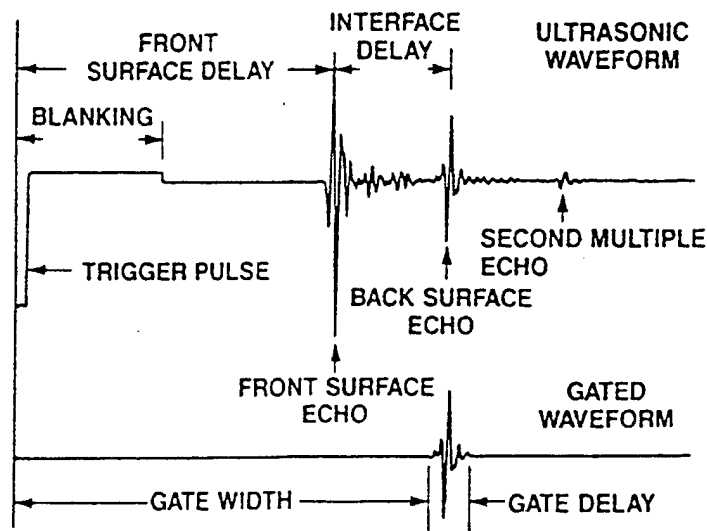
Figure 23. C-Scan Gate Parameters (Blake and Pipes 1990).

The gate width is set by the user to include as much of the waveform as needed, depending on the type of scan chosen. The gate selection determines whether the C-scan will be based upon

attenuation or echo-capture data. Generally, the echo characterization is used to capture delaminations and interlaminar defects. The ultrasonic pulse-echo C-scan technique is used in the present study to identify damage caused by ballistic impact.

A schematic diagram of the procedure of C-scan formation is shown in Figure 24. The image formation is based upon peak amplitude analysis of the gated signal (signal at a particular depth). A short-duration, large-amplitude pulse is transmitted to a lithium-sulphate transducer to create sound in the 2.5–20 MHz frequency range, depending on the form of transducer used. The sound wave is reflected from the material and received by the same transducer that causes the original pulse. This is called the "pulse-echo mode." A gated region is then analyzed for positive or negative peak amplitude. The amplitude signal is divided into 10 discrete levels, each corresponding to a monotonically increasing shade of gray that forms the resulting C-scan image.
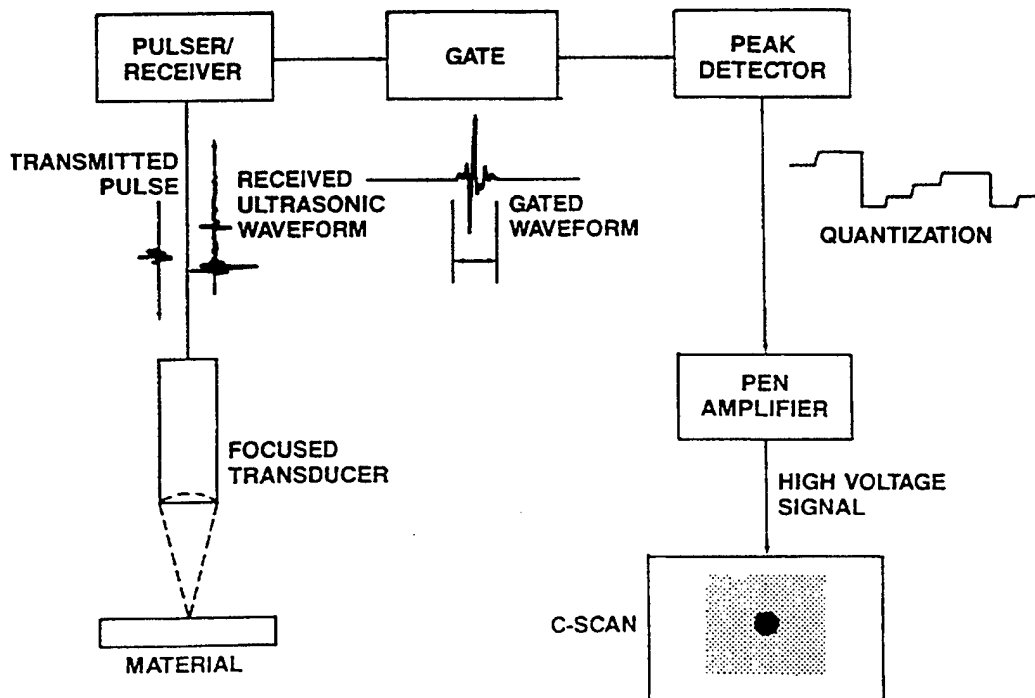
Figure 24. Schematic Diagram of Pulse-Echo C-Scan by Peak Amplitude Analysis.

39

Due to availability, the ultrasonic C-scan was used rather than the x-ray CT. With multiple gating software/hardware capability, the C-scan equipment is capable of obtaining the same information as the CT. Figure 25 shows the C-scan equipment used for this study. The material is placed inside the water tank, and the transducer is focused at the appropriate height above the specimen. The transducer is capable of moving in both the longitudinal and transverse directions with the aid of the two screw drives attached to the sides of the tank. The damaged panels scanned in this study were all made of 18-oz or 24-oz S-2 glass reinforcement in a SC-4 epoxy resin, 411-C50 vinyl-ester resin, or CYCOM 4102 polyester prepreg. Panels were 30.48 cm × 30.48 cm × 1.78 cm (12 in × 12 in × 0.7 in) in dimension. A 5-MHz transducer was used to scan the parts. Damage evaluations were made at three different depth locations. The location of gate 1 was taken just below the impact surface, at a depth approximately 10% of total thickness. Gate 2 was located at the middle of the panel, while gate 3 was located near the back face at a depth approximately 80% of total thickness. A sample of a ballistically impacted S-2 glass/vinyl-ester panel is shown in Figure 26. Severe multiple delaminations are found through the thickness. Visual inspection and residual strength testing has also shown severe fiber damage to exist. Results of the C-scan testing are presented in section 4 and the Appendix.

2.6 CAI Testing. When a ballistically impacted panel is subjected to compression loading, cracks and delaminations may grow to the undamaged area of the plate. In addition, fiber damage caused by the impact energy may lead to high internal stress concentrations upon compression loading. These factors, in turn, lead to global failure of the structure at loads well below the design allowable.

In order to determine the residual compressive strength of the shot panels, a large-scale compression fixture was designed that could support 12-in × 12-in panels of varying thickness (0.72 in–1.7 in). All of the fixture components were made of 1/2-in-thick cold-rolled steel to ensure that the applied loads could be sustained. The base plate shown in Figure 27 is dimensioned to match the base of the Tinius Olsen compression machine. Since the fixture was manufactured by an outside machine shop, English units were used to dimension the parts.
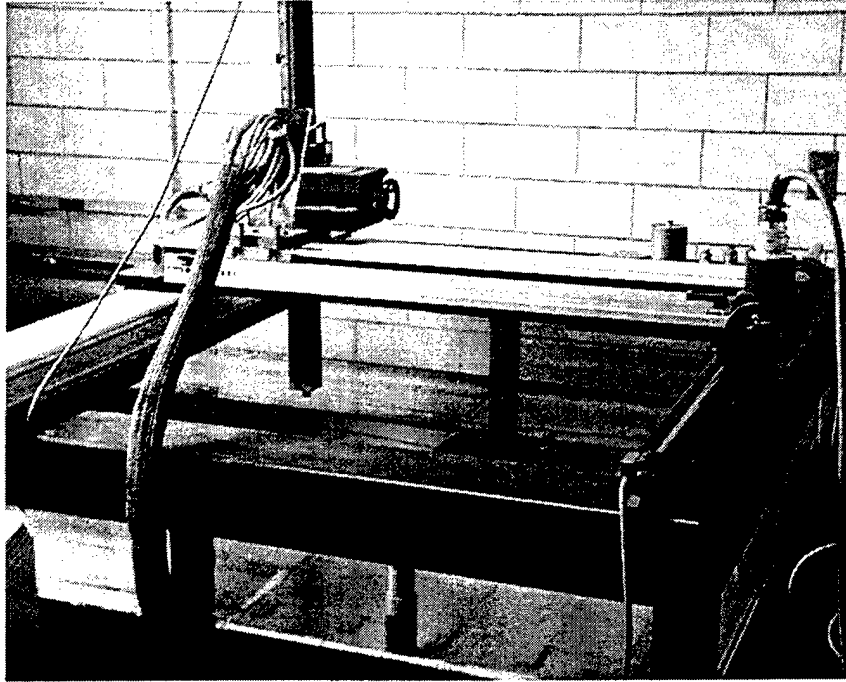
Figure 25. Ultrasonic Scanning Equipment.
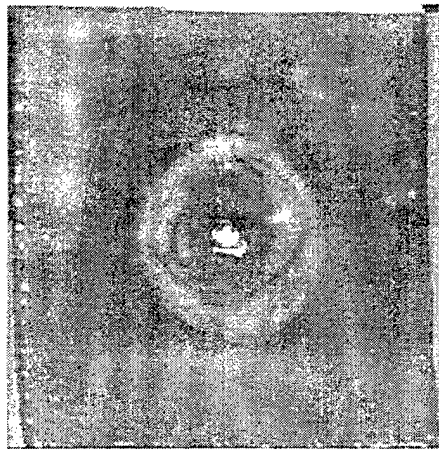
Figure 26. Ultrasonic Image at Gate 3 of 18-oz Vinyl-Ester Panel.

Two angles (Figure 28) are attached to the base plate by the threaded holes shown in Figure 27. The damaged panel is inserted between the two angles and clamped with side clamps (Figure 29[a]) that fasten to the angles. The side clamps are meant to provide stability to the
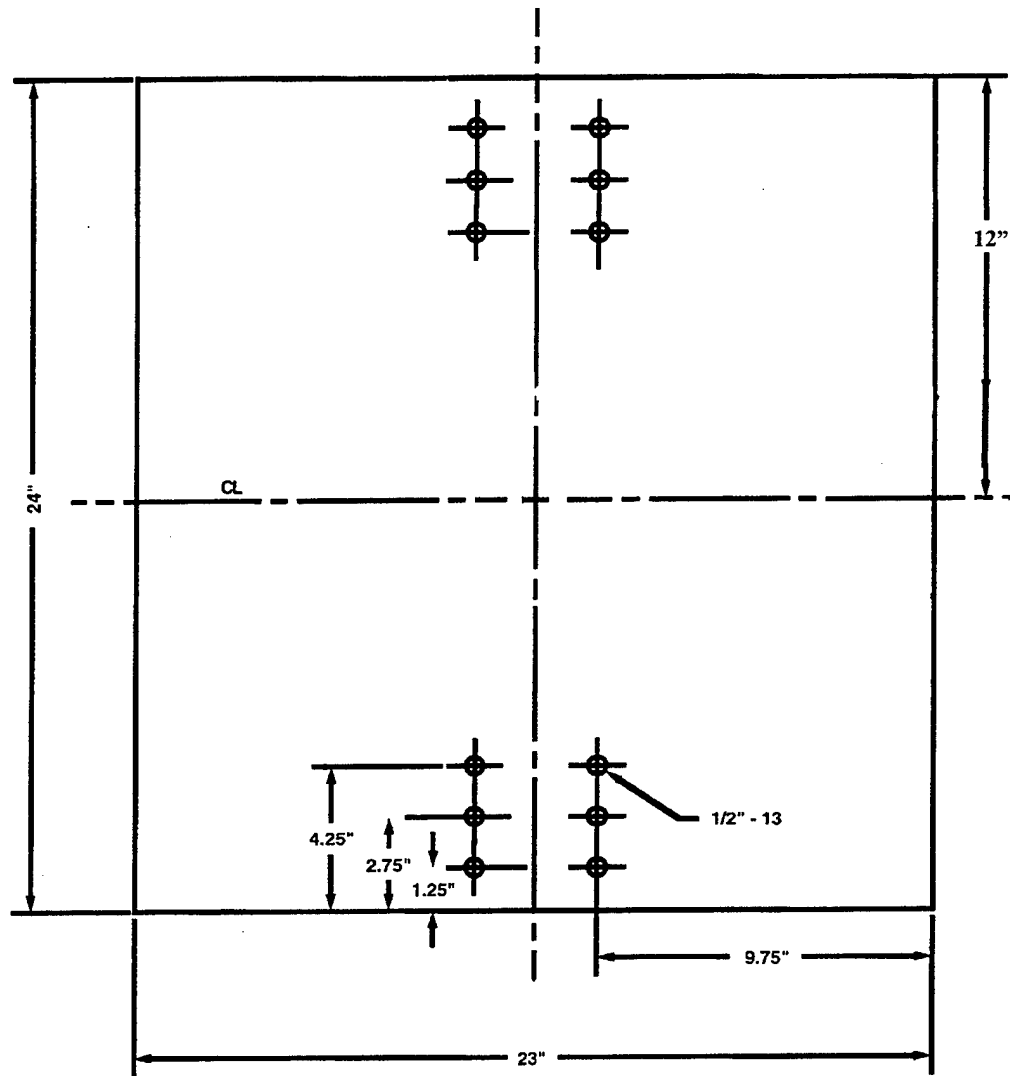
Figure 27. Base Plate.

damaged panels in order to prevent global buckling. The side clamps act as simple supports along the panel edges. A top-hat fixture (Figure 29[b]) is then attached to the upper platen of the Tinius Olsen and lowered unto the edge of the panel. The panel is then loaded under displacement control until failure.

The overall fixture assembly is shown in Figure 30. Due to load introduction, stress concentrations related to geometric tolerances in the panel (e.g., flatness and parallelism) arose.
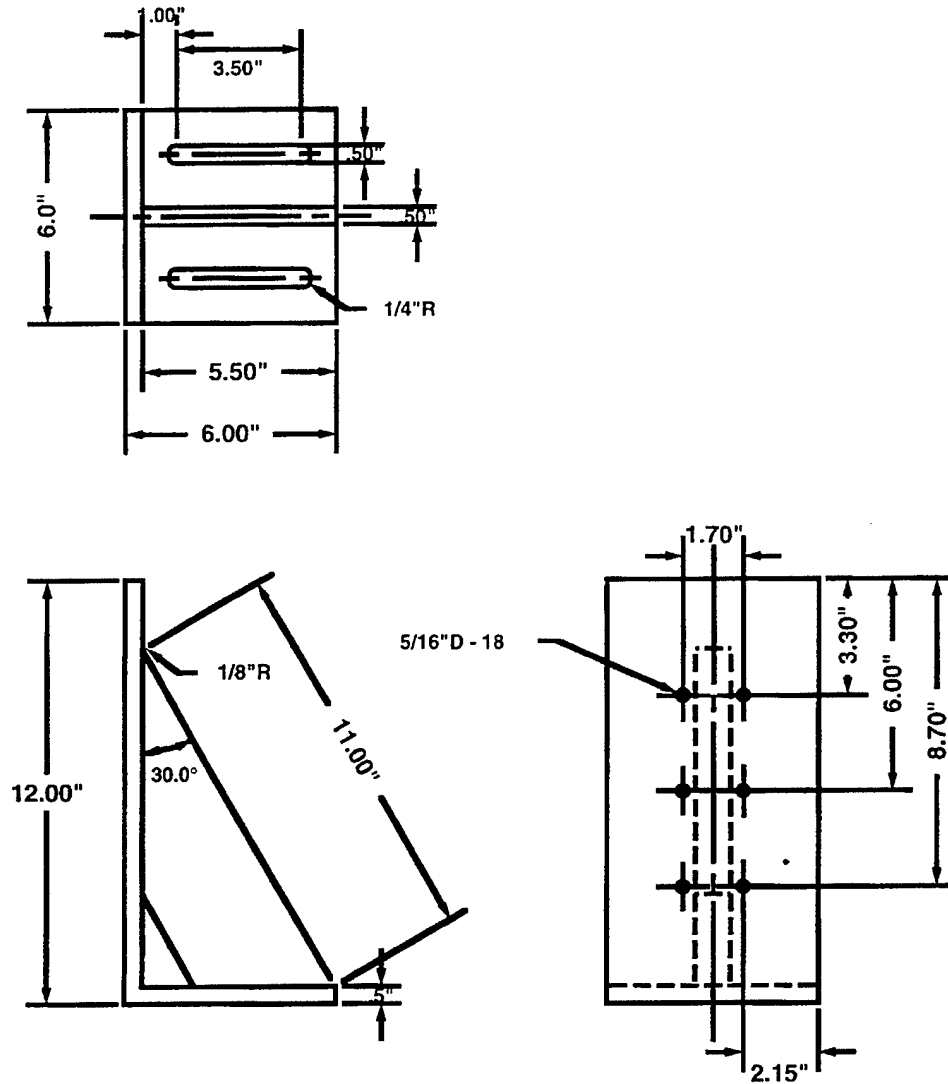
Figure 28. Side Support Angles.

This caused the ends to crush and gave an inaccurately low value for compressive strength. In order to overcome this problem, an aluminum strip 1/2 in thick was placed between the steel fixture and the composite panel. Placing the lower modulus aluminum between the composite panel and steel fixture allowed for a more gradual transition of stresses from the fixture to the panel, which, in turn, led to a reduction in local stress concentrations at the panel edge.

(a)   **(b)**
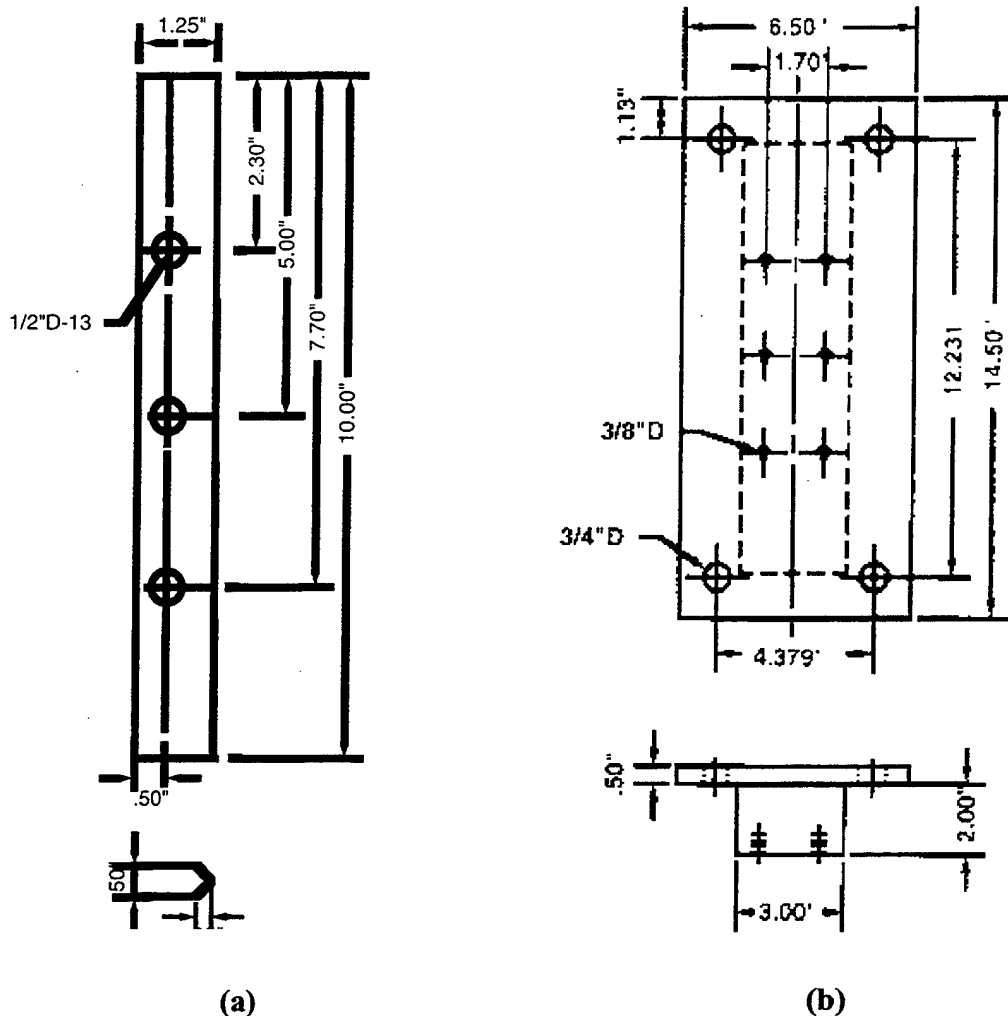
Figure 29. (a) Knife Edge Clamps (Provide Stability to Panel) and (b) Top-Hat Fixture.

In this study, the CSDS program developed by Wanthal et al. (1993) is used to predict CAI strength and the predominant mode of failure: in-plane failure, or instability related delamination growth. The model is based on Lekhnitskii's (1968) in-plane failure analysis and Flanagan's (1988) delamination growth model and will be discussed in further detail in the following section. The CSDS analytical model was experimentally verified for thin-section carbon/epoxy systems by McDonnell Douglas and for thick-section glass/resin systems in the present study. The viability of the model in designing for optimal damage tolerance is also demonstrated.

44
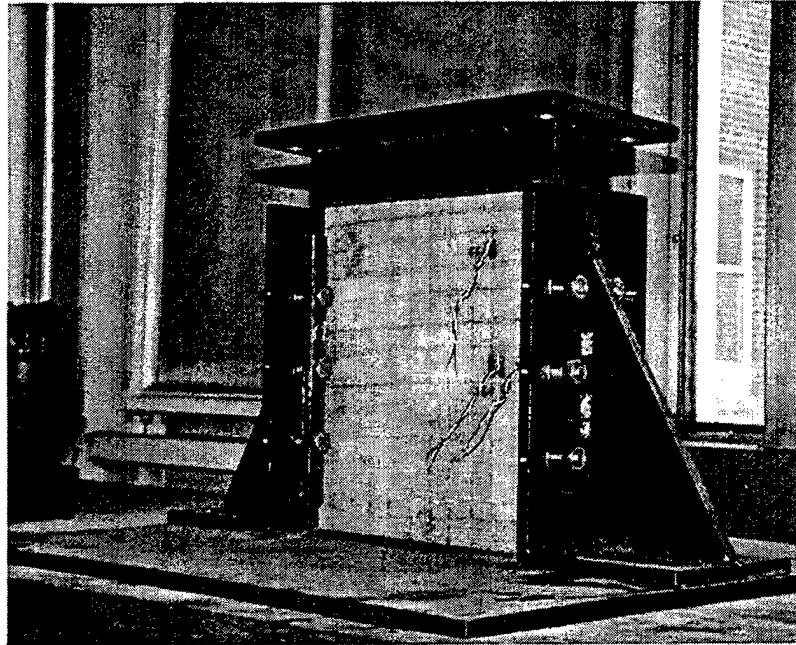
Figure 30. Compression Fixture Assembly With 0.31-m × 0.31-m × 0.02-m (12 in × 12 in × 0.72 in) Panel.

2.7 Background Summary. In this section, a brief summary is given of processing, materials, and test techniques used in this study. Composite laminates 30.48 cm × 30.48 cm × 1.78 cm (12 in × 12 in × 0.7 in) in dimension were manufactured using the SCRIMP process and manual layup of prepreg. Panels made with the SCRIMP process were made using either SC-4 epoxy resin, or vinyl ester 411-C50. Two S-2 glass-fiber preforms were used in the SCRIMP process: a 5 × 5 plain weave S-2 glass, and a 2 × 2 twill weave S-2 glass fabric. A preform set from each panel type was stitched through the thickness with 2,000 denier, 3-ply Kevlar thread, in order to compare ballistic and CAI properties to the nonstitched panels. A set 5 × 5 plain weave S-2 glass/CYCOM 4102 prepreg was also manufactured for baseline testing. The CYCOM prepreg material was originally investigated by the U.S. Army Materials Technology Laboratory at Watertown, MA, as a candidate for the CAV. It was not possible to stitch the prepreg material due to its high tackiness at room temperature.

Panels were then ballistically impacted using a 50-cal. FSP fired from a rifled barrel 8 ft (2.44 m) in length. Ballistic testing was performed at an average velocity of 1,550 ft/s

45

(472.45 m/s). After ballistic testing, the panels were evaluated for damage, using nondestructive-ultrasonic C-scan inspection. A 5-MHz transducer was used to scan the parts. Damage evaluations were made at three different depth locations. The location of gate 1 was taken just below the impact surface, at a depth approximately 10% of total thickness. Gate 2 was located at the middle of the panel, while gate 3 was located near the back face at a depth approximately 80% of total thickness.

After impact testing and nondestructive evaluation, the panels were tested for their residual compression strength. Panels were placed edgewise in a large compression fixture under static loading. Results of the compression testing were used to validate the CSDS model and to determine modes of failure. In addition, the effects on damage tolerance of stitching, processing technique, resin system, and ceramic tiles were investigated.

3. Modeling Compression Strength of Ballistically Damaged Structures

3.1 Introduction. The residual strength of composite structures is reduced when subjected to ballistic damage. As shown in the previous section, a region of the material will be extensively delaminated. Within this inclusion of delaminated material, significant fiber and matrix damage also exists. This region exhibits significant stiffness loss resulting in stress concentrations at the periphery of the inclusion, and reduction in tensile, compression, and shear strength of the laminate. In compression, instability related delamination growth is a second failure mode that must be considered. Historically, compression loading is most critical and governs damage-tolerance-based designs. In this study, our focus is on both the stress concentration factor (SCF) and delamination growth subject to compression loads in thick-section laminates.

Generally, the most accurate way to predict CABI strength would be to conduct detailed stress analysis that would require detailed information about the damage state at each ply level

46

through the thickness. This information is often impossible to measure by NDE techniques. An alternative approach is to assume that embedded delaminations, fiber damage, and matrix damage are the dominant types of damage that govern CABI strength. Other modes of energy dissipation during a ballistic event exist (such as fiber-matrix failure); however, it has been found that embedded delaminations and fiber damage govern CABI strength in thin-section carbon/epoxy laminates (Wanthal et al. 1993).

CABI can be predicted by either assuming that delaminations will buckle due to the compressive load, leading to unstable delamination growth, or by assuming that stress concentrations develop in and around the damaged region, resulting in membrane failure. The purpose of this section is to introduce the analytical methods employed in the model and then to validate the results both numerically and experimentally. A case study is examined in which monolithic laminates of S-2 glass/polyester were impact damaged, nondestructively evaluated, and compression tested in previous work (Chou and DeLuca 1993). The data is compared to predictions made using the analytical methods to be described. In the following section, an analytical program is used to gain an understanding of the failure mechanisms of ballistically impacted composite structures subjected to compressive loading. In addition, the model is utilized to examine the tradeoffs that exist between improving ballistic performance by absorbing more energy over larger regions versus improving residual strength by minimizing damage size.

3.2 Overview of Analysis Methods. Two failure modes are considered. In-plane failure due to localized stress concentrations is described in section 3.2.1 and delamination growth is described in section 3.2.2.

3.2.1 In-Plane Failure. One of the predominant failure mechanisms governing CAI strength is that of membrane failure or in-plane failure. This type of failure generally occurs when there is a loss of stiffness in the damaged area due to impact-induced matrix cracking and extensive fiber breakage (Wanthal et al. 1993; Tan 1994). As mentioned previously, in-plane failure is assumed to occur when stress concentrations increase stress near the damaged region that exceed the undamaged strength of the material. The scope of damage is difficult to

47

determine precisely using nondestructive techniques. Thus, in order to determine the state of stress, damage is modeled as elliptical inclusions of specified stiffness reduction within an undamaged parent laminate (Wanthal et al. 1993). In Lekhnitskii's (1968) famous work *Anisotropic Plates*, a solution is derived for the stress state in and around an inclusion in an infinite plate. The inclusion is assumed to be homogeneous with the same layup as the parent laminate, but with reduced stiffness properties.

3.2.1.1   Lekhnitskii's   Stress   Determination   in   a   Plate   With   an   Elliptic   Inclusion.
Lekhnitskii's work combines results for the stress state of an anisotropic plate, with and without an elliptical hole, to solve the more general case of an anisotropic plate with a bonded center of some intermediate stiffness. The general solution to the stress-strain distribution of an anisotropic plate with and without an elliptical opening subjected to external forces can be found in detail in *Anisotropic Plates* (Lekhnitskii 1968), where Lekhnitskii employs a complex variable method to derive his solution. For the general case of an elliptical opening filled with an inclusion, Lekhnitskii examines an anisotropic plate of arbitrary shape (Figure 31). The inclusion is taken to be the same thickness as the parent plate but of a different material. The inclusion is assumed to be small in comparison to the dimensions of the plate, and is thus at a distance from the edges. Also the inclusion is perfectly bonded to the parent plate. Arbitrary forces act all around the plate edge at the middle plane. Based on these assumptions, Lekhnitskii proceeds to determine the stresses in the plate and in the inclusion due to external forces. A brief summary of Lekhnitskii's solution is given here for reference.
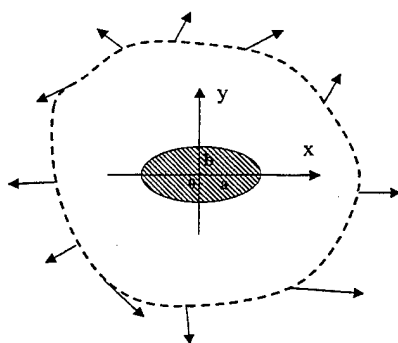
Figure 31.   Anisotropic Plate of Arbitrary Shape With Inclusion.   Inclusion Is of Same Thickness as the Plate but of Different Material.

The technique involves deriving a general equation for the stress function that satisfies both equilibrium and compatibility conditions in terms of imaginary and real components. Lekhnitskii introduces a "characteristic equation" by which he determines in-plane stress components for anisotropic plates (Henshaw et al. 1996).

The coordinate axes are taken to be in the direction of the principal axes, for simplicity. Hereafter, all variables related to the inclusion will be marked with a prime to distinguish them from the variables associated with the parent plate. The inclusion is taken to be elliptical and is thus described by

$$x = a \cos \vartheta \text{ and } y = b \sin \vartheta, \tag{6}$$

where a and b are the lengths of the major and minor elliptical axes, respectively, and ϑ is the counterclockwise angle from the positive x axis.

The generalized Hooke's law for the parent laminate will be written as follows:

$$\left. \begin{array}{l} \varepsilon_x = a_{11}\sigma_x + a_{12}\sigma_y + a_{16}\tau_{xy}, \\ \varepsilon_y = a_{12}\sigma_x + a_{22}\sigma_y + a_{26}\tau_{xy}, \\ \gamma_{xy} = a_{16}\sigma_x + a_{26}\sigma_y + a_{66}\tau_{xy}. \end{array} \right\}, \tag{7}$$

where the a_{ij}'s are the elastic constants. The generalized Hooke's law for the inclusion is the same, except that a_{ij} is replaced with a'_{ij}. Deformations in the plate are assumed to be small and therefore the problem can be solved approximately by superimposing the stresses in a plate without an inclusion with the stresses in a plate with an elliptical opening. The stress and displacement functions for a plate with an inclusion are:

$$\left. \begin{array}{l} \sigma_x = \sigma^\circ_x + 2\,\text{Re}\left[\mu_1^2 \phi'_1(z_1) + \mu_2^2 \phi'_2(z_2)\right] \\ \sigma_y = \sigma^\circ_y + 2\,\text{Re}\left[\phi'_1(z_1) + \phi'_2(z_2)\right] \\ \tau_{xy} = \tau^\circ_{xy} - 2\,\text{Re}\left[\mu_1 \phi'_1(z_1) + \mu_2 \phi'_2(z_2)\right] \end{array} \right\}, \tag{8}$$

49

where σ°_x, σ°_y, and τ°_{xy} represent the stress components for a plate without an inclusion, and z_1 and z_2 are complex variables of the type:

$$z_1 = x_1 + iy_1 \text{ and } z_2 = x_2 + iy_2. \tag{9}$$

The displacement components in the plate with the inclusion are:

$$\left. \begin{array}{l} u = u^\circ + 2\,\mathrm{Re}[p_1\phi_1(z_1) + p_2\phi_2(z_2)] - \omega y + u_o \\ v = v^\circ + 2\,\mathrm{Re}[q_1\phi_1(z_1) + q_2\phi_2(z_2)] + \omega x + v_o \end{array} \right\}, \tag{10}$$

where u° and v° represent the displacement components for a plate without an inclusion. The constants w, u_o, and v_o characterize the rigid body displacements and the remaining functions are defined as:

$$\left. \begin{array}{l} p_k = a_{11}\mu_k^2 + a_{12} - a_{16}\mu_k \\ q_k = a_{12}\mu_k + \dfrac{a_{22}}{\mu_k} - a_{26} \end{array} \right\}. \tag{11}$$
$$(k = 1,2)$$

The functions ϕ_1 and ϕ_2 in equation 10 are functions of complex parameters. The complex parameters are defined as:

$$\phi_i(z_i) = \frac{dF_i}{dz_i}, \tag{12}$$

where F_i is a function of the other stress components and is introduced to satisfy equilibrium conditions. The ϕ function describes the effect of the inclusion on the additional stresses in the plate. If the deformation equations are expressed in terms of the stress components (using the generalized Hooke's law), a differential equation is obtained which must be satisfied by the

50

stress function, F (x,y). The characteristic roots of the differential equation are called the *complex parameters* and are given by μ_1, and μ_2. The characteristic equation of the plate is:

$$a_{11}\mu^4 - 2a_{16}\mu^3 + (2a_{12} + a_{66})\mu^2 - 2a_{26}\mu + a_{22} = 0.$$ (13)

The complex parameters can be considered as numbers that describe the degree of anisotropy.

Let us next consider the stress in the elastic inclusion. The stress function in the elastic inclusion, F' can be expressed by two functions of complex variables—$z_1' = x + \mu_1'y$, and $z_2' = x + \mu_2'y$—where μ_1', and μ_2' are the complex parameters for the inclusion. Boundary conditions for points on the contact surface can be written as (Figure 32):
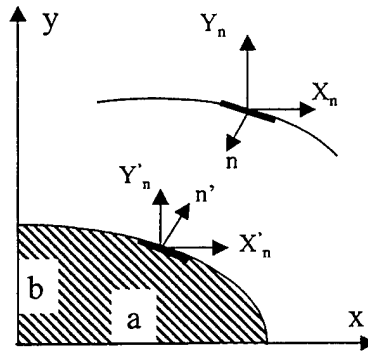
Figure 32. Boundary Conditions of Points on the Contact Surfaces.

$$\left.\begin{array}{ll} X_n = X_n' & Y_n = Y_n' \\ u = u' & v = v' \end{array}\right\}, \qquad (14)$$

where X_n and Y_n are external forces and X_n' and Y_n' are forces at the edge of the inclusion contour. The variables u, v, and u', v' define the rigid body displacements at the contour surfaces of the plate and inclusion, respectively. Transforming the boundary conditions in equation 14 results in:

$$
\left.\begin{aligned}
2\,\mathrm{Re}[\phi_1(z_1) + \phi_2(z_2)] &= \frac{\partial(F' - F^0)}{\partial x} + c_1, \\[4pt]
2\,\mathrm{Re}\left[\mu_1\phi_1(z_1) + \mu_2\phi_2(z_2)\right] &= \frac{\partial(F'-F^0)}{\partial y} + c_2, \\[4pt]
2\,\mathrm{Re}[p_1\phi_1(z_1) + p_2\phi_2(z_2)] &= u' - u^0 + \omega y - u_o, \\[4pt]
2\,\mathrm{Re}[q_1\phi_1(z_1) + q_2\phi_2(z_2)] &= v' - v^0 - \omega x - v_o,
\end{aligned}\right\}.
\tag{15}
$$

The constants c_1, c_2, ω, u_o, and v_o depend on the plate shape and the distribution of forces. The conditions stated in equation 15 are true not only for plates with an elliptical inclusion, but also for inclusions of any geometry (Lekhnitskii 1968).

By solving the boundary conditions in equation 15, the functions ϕ_1, ϕ_2, and their derivatives can be determined and, consequently, equations 8 and 10 can be evaluated. Lekhnitskii solved specific examples for plates with elliptical inclusions and orthotropic plates with circular inclusions. Figures 33 and 34 show Lekhnitskii's solution for a plywood plate of orthotropic properties with an elastic inclusion ($2\,a_{ij} = a'_{ij}$), a hard inclusion ($a'_{ij} = 0$) and no inclusion ($a'_{ij} = \infty$). Figure 33 shows the radial stress distribution around the inclusion contour, while Figure 34 shows the tangential stress distribution. In the case for no inclusion ($a'_{ij} = \infty$), there is no radial stress contribution and the tangential stress distribution is highest. From these figures one concludes that an elastic or rigid inclusion significantly reduces the maximum stress values and also causes a measurable change in the nature of the stress distribution.

The analytical solutions presented by Lekhnitskii are computationally intensive and thus require a computer program (Wanthal et al. 1993) to be of practical use. Nevertheless, the analytical approximations are less time intensive than finite element analysis and serve as a good approximation.

In addition to Lekhnitskii's solution, several methods have been proposed to examine the case of an infinitely wide composite panel with an open hole or crack (Whitney and
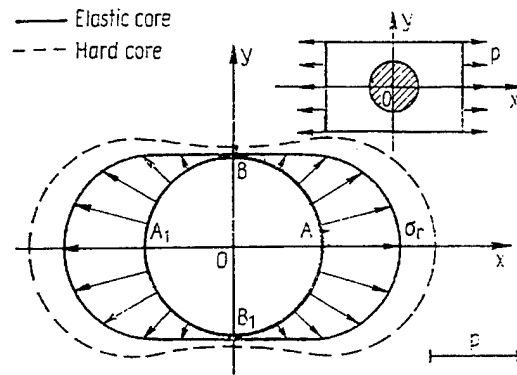
Figure 33. **Radial Stress Distribution, σ_r, at the Opening Contour of a Plywood Plate Subjected to Unidirectional Tension (Lekhnitskii 1968).**
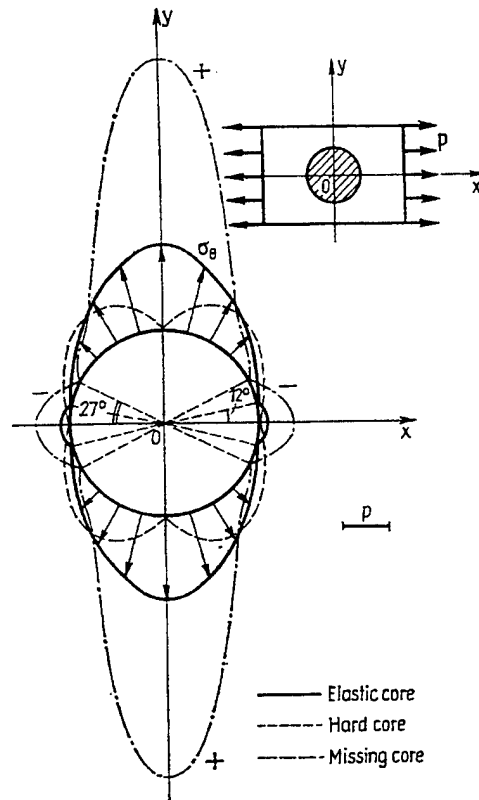
Figure 34. **Tangential Stress Distribution, σ_θ, at the Opening Contour of a Plywood Plate Subjected to Unidirectional Tension (Lekhnitskii 1968).**

Nuismer 1974; Mar and Lin 1977; Pipes et al. 1979). For cases involving a plate of finite width, a correction factor must be introduced, K_T, that accounts for the substantial change in the normal stress distribution due to the width-to-hole geometry. The finite width correction factor is discussed in more detail in the following section.

3.2.1.2 Stress Distribution in an Infinite Width Plate. Before using FEA to examine finite width effects and varying inclusion stiffness, the model is verified against the series solution for the normal stress distribution in an infinite orthotropic plate with an open hole. Whitney and Nuismer (1974) and Gillespie and Carlsson (1988) have shown that Lekhnitskii's equation for the normal stress distribution in an infinite isotropic plate with a circular hole (Figure 35) can be used to derive a good approximation for an orthotropic plate.
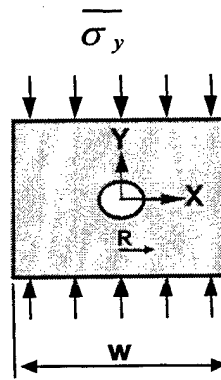
Figure 35. Plate Containing Circular Hole, With Far-Field Stress Being Applied.

The stress distribution $\sigma_y^\infty(x,0)$ ahead of the hole edge, with $x \geq R$ for an infinite orthotropic plate is,

$$\sigma_y^\infty(x,0) = \frac{\overline{\sigma}_y}{2}\left[2 + \left(\frac{R}{x}\right)^2 + \left(\frac{R}{x}\right)^4 - \left(K_T^\infty - 3\right)\left(5\left(\frac{R}{x}\right)^6 - 7\left(\frac{R}{x}\right)^8\right)\right], \qquad (16)$$

where $\overline{\sigma}_y$ is the far-field applied stress and K_T^∞ is the stress concentration factor for an infinite plate:

54

$$K_T^\infty = 1 + \sqrt{2\left(\sqrt{E_y/E_x} - \upsilon_{yx} + E_y/(2G_{xy})\right)}. \tag{17}$$

Figures 36 and 37 show plots of the normal stress distribution for the series solution presented in equation 16 and the FEA. In the FEA model, four-node plane stress elements were used with three-node triangular elements near the center of the inclusion. A finer mesh size was used near the inclusion since the stress gradient is higher in this region. A sample mesh of the FEA model (Huang 1998) is shown in Figure 38. Properties used in the analysis are listed in Table 7. The terms X_T, Y_T, X_c, and Y_c in Table 7 represent the tensile and compressive strengths in the x and y directions, respectively. The x and y directions are defined in Figure 35. The finite element computations were performed using the ABAQUS finite element commercial code. ABAQUS was also used as the pre- and post-processing software for meshing and data analysis. For the purposes of the FEA model, a W/D ratio of 12 is used to approximate the infinitely wide solution.
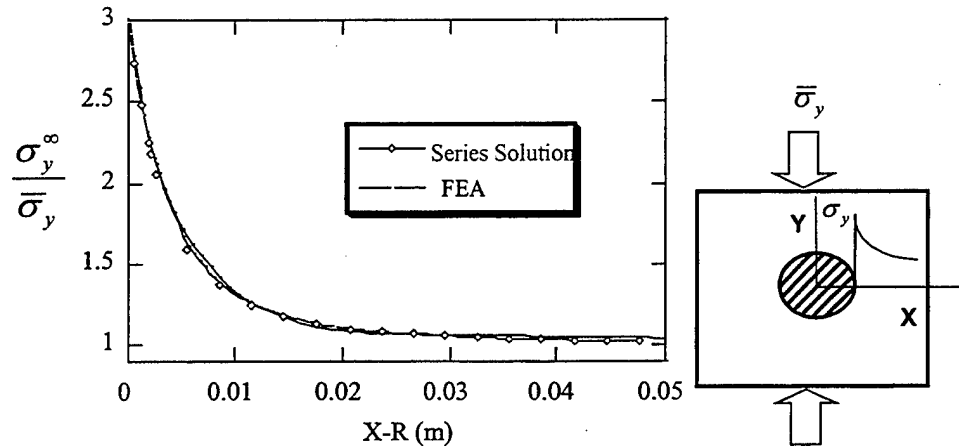
Figure 36. Normal Stress Distribution for Infinitely Wide Isotropic Plate With Open Hole.

Figure 36 shows the case for an isotropic plate and Figure 37 the orthotropic case. In both cases there is excellent agreement. The values for $\sigma_y^\infty/\bar{\sigma}_y$ in Figures 36 and 37 represent the normal stress distribution along the panel mid plane. The distance x is taken from the center of the plate, where R is the radius of the hole.

55
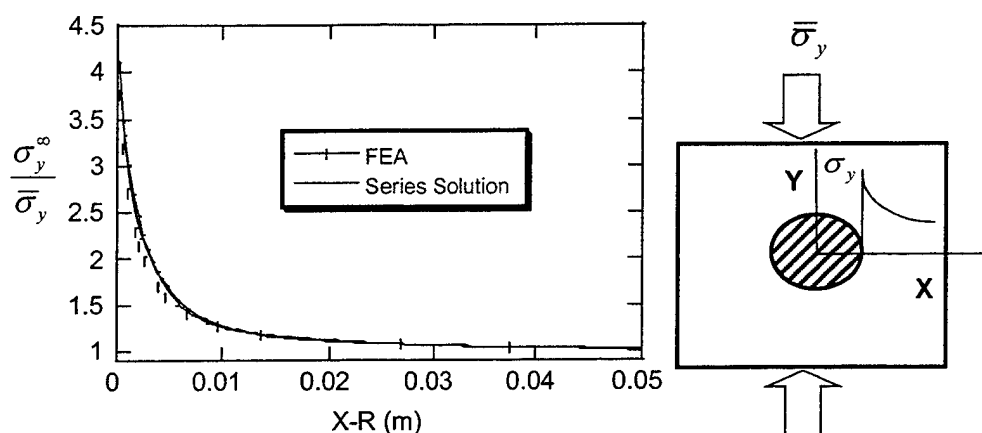
Figure 37. Normal Stress Distribution for Infinitely Wide Orthotropic Plate With Open Hole.
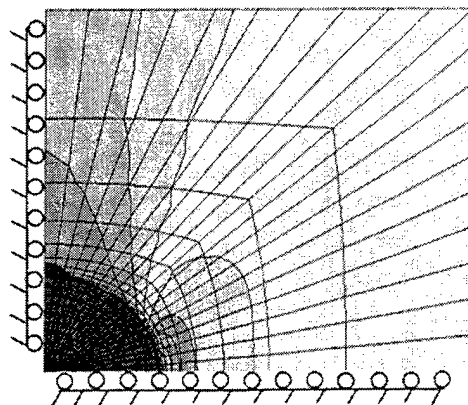
Figure 38. Finite Element Mesh for Orthotropic Panel With an Inclusion and Free Edge Boundary Conditions. The Darkest Quarter-Circle Indicates the Region Within the Inclusion. Dark-to-Light Color Gradient Indicates High-to-Low Stress Intensity.

Table 7. Properties Used in Finite Element Analysis

24-oz. S-2 Glass/Vinyl Ester 411-C50 Orthotropic Laminate	Material and Strength Properties
E_x, E_y	24.00 GPa
E_z	8.00 GPa
v_{xy}, v_{yz}, v_{xz}	0.28
G_{xy}, G_{yz}, G_{xz}	2.76 GPa
X_T, Y_T	541.95 MPa
X_c, Y_c	384.00 MPa

The local stress is normalized with respect to the far-field applied stress. At the edge of the hole, where x = R, the normalized stress converges to the stress concentration value for an infinite plate. As the distance from the hole edge increases, the effect of the hole on stress distribution diminishes rapidly until the local stress equals the far-field applied stress. Note that the stress value at the hole edge in the orthotropic case is higher than for the isotropic case.

3.2.1.3 Stress Distribution in a Finite Width Plate. In the experimental study, the effects of finite width on stress distribution must be considered. One of the main limiting assumptions in Lekhnitskii's analytical model is that the plate is of infinite width. In recent years, extensive research has been conducted to examine the effects of finite width-to-hole ratios in notched composites. However, numerical difficulties arise in determining the stress distribution in finite width plates, since no closed-form solution exists for the stress distribution in a finite width plate with an inclusion. In this case, finite element analysis (FEA) must be used. This is particularly important when examining the in-plane failure mode where hole-to-width effects can cause large changes in stress distribution (Gillespie et al. 1988; Tan 1994).

Once confidence in the FEA model was established for the infinite width case in section 3.2.1.2, the analysis was used to determine the stress distribution in the S-2 glass/vinyl-ester plate of finite width and orthotropic properties and compared to the series solution for the open hole case. The model used a width-to-hole ratio, W/D, of 3 in order to approximate the experimental results presented in section 4. Figure 39 indicates good agreement exists between the series solution and the FEA model. The stress distribution near the hole perimeter is 13% higher in the finite width case than in the infinitely wide case.

This validation provides confidence in the FEA model, which will subsequently be used to determine the stress distribution in a finite width plate with an inclusion. A failure criterion similar to that used for notched strength predictions may then be used to predict residual strength.

3.2.1.4 Notched Strength. It should be noted that the main objective of stress analysis is strength prediction. However, most strength criteria are semi-empirical in nature, while stress
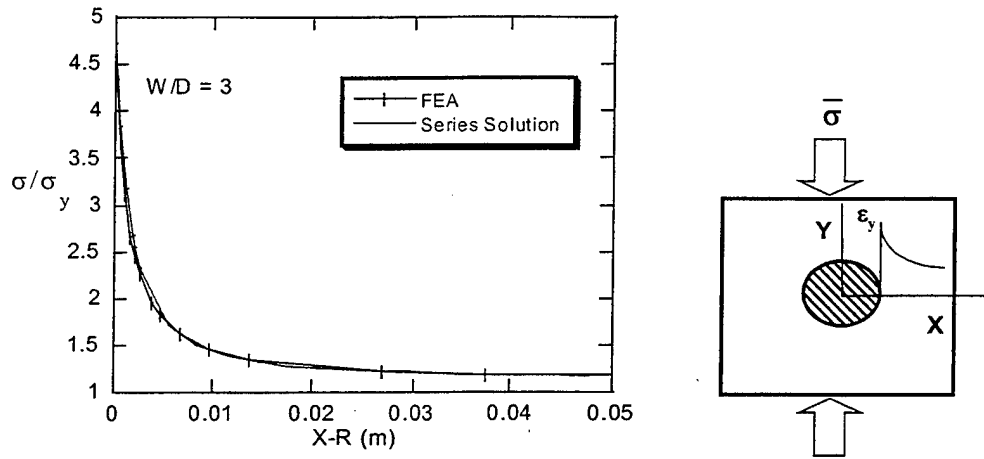
Figure 39. Normal Stress Distribution for Finite Width Orthotropic Plate With Open Hole (W/D = 3).

analysis requires physical boundary conditions to solve for unknowns. This issue has been examined in terms of both linear and nonlinear fracture mechanics. Awerbuch and Madhukar (1985) give a complete survey of the commonly used fracture models in a comprehensive literature review.

From a designer's viewpoint, the easiest way to predict notched strength is to examine the stress distribution adjacent to the notch. One of the most common failure criteria employed is the point stress criterion (PSC) developed by Whitney and Nuismer (1974). The PSC criteria assumes that failure occurs when the normal stress, $\sigma_y(x,0)$, at a characteristic distance $x = R + d_0$, ahead of the hole edge equals the unnotched strength of the material,

$$\sigma_y(R + d_0, 0) = \sigma_0, \tag{18}$$

where σ_0 is the unnotched strength, R is the hole radius (Figure 35), and d_0 is the characteristic distance from the hole edge (Gillespie et al. 1988).

No closed form solution exists for anisotropic plates of finite width. Rather than resorting to time-consuming numerical techniques, a more common practice is to utilize approximate

58

analytical methods that utilize experimental data from finite width geometries. In order to properly correlate experimental notched strength data to a stress fracture criterion, a "finite width correction factor" is typically applied (Gillespie et al. 1988). The explanation to follow presents the commonly used finite width correction factors, K_T, in laminates with an open hole. The stress concentration factor, K_T, is not known analytically for inclusions of reduced stiffness. Approximate analytical solutions for K_T have been proposed, however, for finite plates with an open hole where the inclusion stiffness is $E = 0$. For cases where $E \neq 0$, it was necessary to apply finite element analysis to determine the stress concentration in a finite width plate.

One typical finite width correction (FWC) factor that is commonly applied to relate notched strength, σ_N, of finite width plates to the notched strength of plates of infinite width is to simply multiply σ_N by a correction factor $\dfrac{K_T}{K_T^\infty}$, so that:

$$\sigma_N^\infty = \sigma_N \frac{K_T}{K_T^\infty}, \tag{19}$$

where K_T is the stress concentration factor in a plate of finite width, while K_T^∞ is the stress concentration factor in a plate of infinite width.

The value for K_T^∞ is dependent entirely on the material properties (equation 17). The finite width correction factor is given by the following approximation.

$$\frac{K_T}{K_T^\infty} = \frac{2 + (1 - (D/w))^3}{3(1 - (D/w))}. \tag{20}$$

Equation 19 assumes that the entire distribution of stress within the highly stressed region defined by $R \leq x \leq d_o + R$ scales with the parameter $\dfrac{K_T}{K_T^\infty}$. Since it is assumed that the normal

stress profile of a finite width plate is the same as that of an infinite plate except that it is scaled by the factor $\dfrac{K_T}{K_T^\infty}$, the normal stress distribution profile in a finite width plate can be written as:

$$\frac{\sigma_y(x,0)}{\sigma_y^\infty(x,0)} = \frac{K_T}{K_T^\infty} = \text{constant for } R \leq x \leq d_0 + R.$$

(21)

Using equations 19 and 21 yields the approximate stress distribution near the hole:

$$\frac{\sigma_y(x,0)}{\overline{\sigma}_y} = \frac{1}{2}\frac{K_T}{K_T^\infty}\left[2 + \left(\frac{R}{x}\right)^2 + \left(\frac{R}{x}\right)^4 - \left(K_T^\infty - 3\right)\left(5\left(\frac{R}{x}\right)^6 - 7\left(\frac{R}{x}\right)^8\right)\right],$$

(22)

where $\overline{\sigma}_y$ is the far-field average stress in the finite width panel.

The term d_0 in equation 21, often termed "the characteristic distance," is determined empirically. The PSC criterion postulates that failure will occur when the normal stress at some characteristic distance d_0 from the hole edge, equals the unnotched failure strength of the plate (i.e., X_C). When this condition is satisfied the far-field stress is defined as the notched strength, σ_N. Mathematically, the point stress criterion can be written as:

$$\frac{\sigma_N}{X_C} = \frac{2K_T^\infty / K_T}{\left[2 + \xi^2 + 3\xi^4 - (K_T^\infty - 3)(5\xi^6 - 7\xi^8)\right]},$$

(23)

where

$$\xi = \frac{R}{R + d_0}.$$

(24)

Previous studies show that the PSC model gives good agreement with experiments and that the characteristic distance may be dependent on hole radius (Whitney and Nuismer 1974).

Equations 23 and 24 reveal that the PSC predicts a continuous decrease in notched strength with increased hole radius (i.e., $\xi \rightarrow 1$). The asymptotic line is given by:

$$\frac{\sigma_N}{X_C} = \frac{1}{K_T}.$$

(25)

In the case of the open hole K_T is defined by equation 20. For the case of an elastic inclusion, K_T is calculated using FEA. Thus for large hole radii, the characteristic distance d_0 can be taken to be zero. Since the present study deals with relatively large damage areas $\frac{d_0}{R} \ll 1$ the characteristic distance d_0 is taken to be zero.

Through the proper interpolation of finite-plate experimental strength to infinite-plate strength, a value for K_T can be obtained and equations 19 or 21 can be used to predict notched strength. Nevertheless, finite element analysis is still needed to determine the stress concentrations and, consequently, notched strength in a finite width panel with an inclusion of reduced stiffness.

3.2.1.5 Finite Width Plate With an Inclusion. After validating the accuracy of the FEA model for the case of a finite width plate with an open hole, the analysis was used to determine the stress distribution and stress concentration in a finite width plate of varying inclusion stiffness. Figure 40 shows a plot of the stress distribution in an S-2 glass/vinyl-ester laminate of finite width and orthotropic properties, for various inclusion stiffnesses. As before, W/D is set equal to 3. In the figure, a stiffness reduction of 0.25 × E, for example, indicates that the inclusion's in-plane stiffness matrix is reduced 75% from that of the parent laminate. For a case of an open hole (0.00 × E) there is a significant stress concentration at the hole edge that drops rapidly as the edge of the plate is-approached. Figure 40 also shows that adding stiffness to the inclusion from the open hole state greatly reduces the stress concentration.
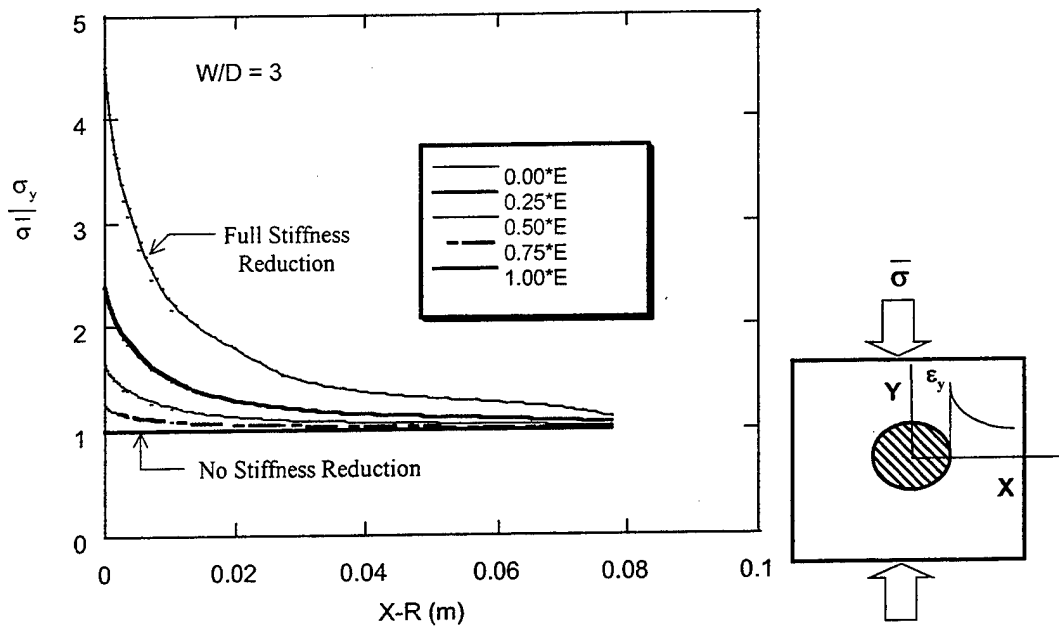
Figure 40. **Stress Distribution in a Finite Width, Orthotropic Plate for Various Inclusion Stiffnesses.**

As mentioned in the previous section, notched strength predictions are typically based upon correlation between experimental notched strength data and the application of a finite width correction factor. Since the stress concentration factor, K_T, is not known analytically for inclusions of reduced stiffness, it is necessary to employ FEA analysis. To investigate further the accuracy of the finite element solution, Figure 41 shows the stress concentration factor, K_T^∞, for an infinite plate of varying inclusion stiffness, based on Lekhnitskii's solution and the FEA model. The plate is an orthotropic layup as in Figures 33 and 34, only with material properties of an S-2 glass/vinyl-ester laminate as described in Table 7. The symbols E and E_o represent the inclusion and parent in-plane stiffnesses, respectively. As the inclusion stiffness approaches the parent stiffness, K_T^∞ approaches 1 as expected. Again, excellent agreement is observed, lending confidence in the accuracy of the numerical solution.

Figure 42 shows a plot of the finite width correction factor as a function of inclusion stiffness for varying W/D using the numerical solution. The plot shows that for large reductions in

62
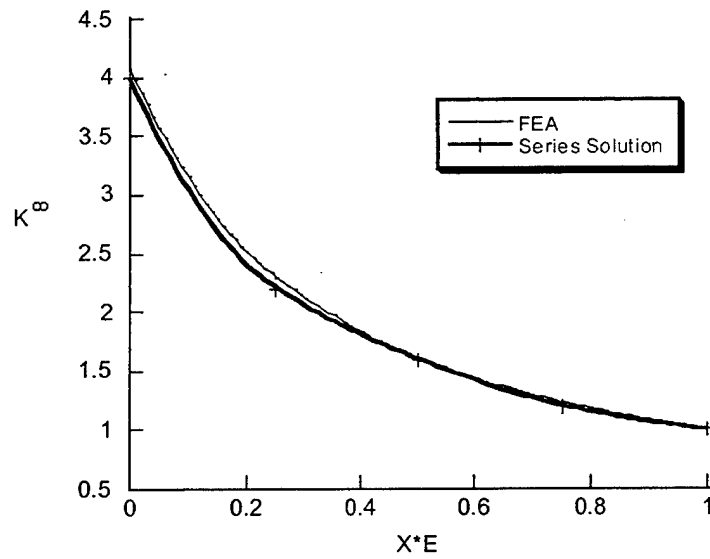
Figure 41. Stress Concentration Factor for an Orthotropic S-2 Glass/Vinyl-Ester Plate of Infinite Width as a Function of Inclusion Stiffness.
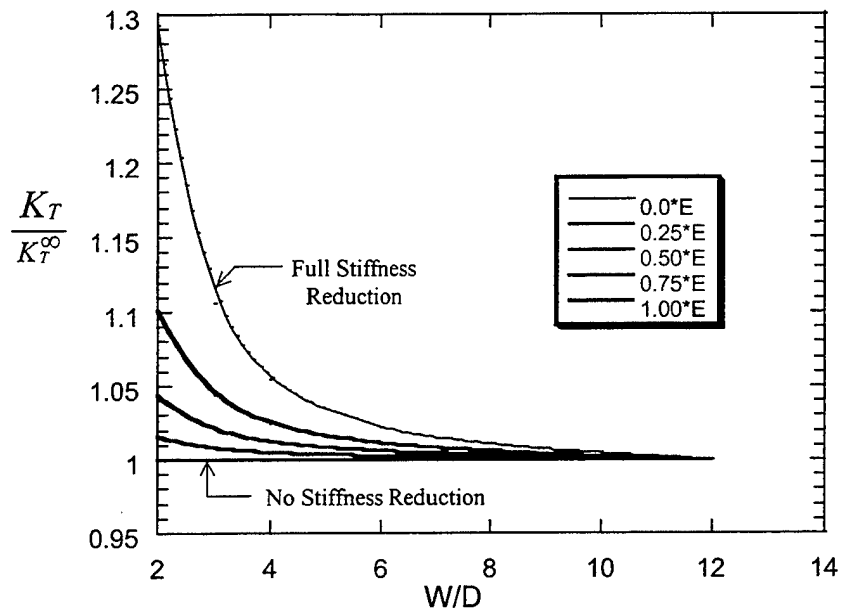
Figure 42. Effect of Inclusion Stiffness and Finite Width on Stress Concentration. For the Open Hole Case $\dfrac{\sigma_N}{X_C} = \dfrac{1}{K_T}$ With $d_0 = 0$.

inclusion stiffness, K_T is highest and decreases asymptotically until K_T equals K_T^∞. Thus, for high stiffness reductions in a plate with a large inclusion, there is significant difference between K_T and K_T^∞.

In summary, CABI strength corresponding to membrane failure is given by $\dfrac{\sigma_N}{X_C} = \dfrac{1}{K_T}$, where K_T can be determined from the results given in Figures 41 and 42.

From Figure 42 it becomes apparent that high stiffness losses due to severe fiber damage greatly increases $\dfrac{K_T}{K_T^\infty}$, which, in turn, can lead to in-plane failure. Therefore, a good ballistic-tolerant design should be one that dissipates the impact energy in such a manner that stiffness losses in the damaged region are minimized. As mentioned in section 1, current solutions include the use of hybrid armor structures where a ceramic tile and layer of urethane rubber are placed in front of the composite laminate. While this approach may minimize fiber damage, it can lead to extensive multi-layer delaminations, in which case failure strength is governed by unstable delamination growth. This failure mode is discussed in the following section.

3.2.2 Delamination Growth. As discussed in section 1, the compressive strength in composite laminates is significantly reduced by local instabilities that arise in the presence of interlaminar defects. When a composite plate with an interlaminar defect is loaded in compression, instability-related delamination growth may occur. In ballistically impacted panels, significant initial out-of-plane deformations exist. Delaminated plies will deform out of plane under the action of the compression load and will result in Mode I (G_I) and Mode II (G_{II}) crack surface displacements at the interlaminar crack tip as shown in Figure 43 (Gillespie and Carlsson 1991). Figure 43 shows a relatively thick composite plate with an embedded through-width delamination near the surface. Once the compressive load reaches a critical strain level, the thinner sublaminate buckles out of plane causing tensile (Mode I) and shear (Mode II) deformations to develop at the crack tip. Thus crack extension will occur when the combination

64
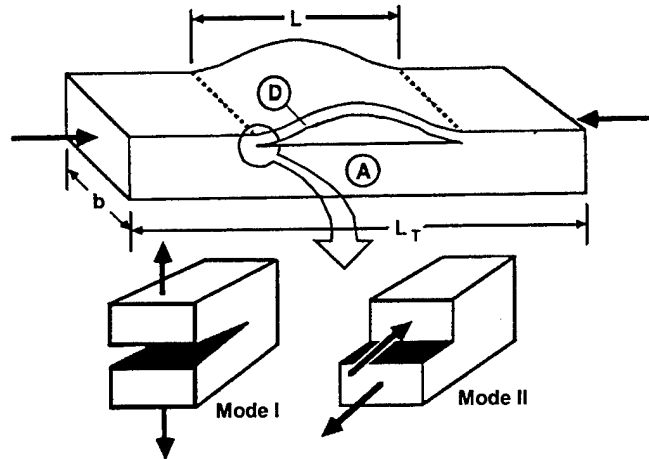
Figure 43. **Composite Plate With an Interlaminar Defect. The Delamination Divides the Plate Into Two Parts: (D) the Buckled Sublaminate and (A) the Parent Laminate. At the Crack Tip, Both Normal and Shear Stress Develop Causing Mode I and Mode II Crack Displacements, Respectively (Gillespie and Carlsson 1991).**

of Mode I and Mode II strain energy release rates exceeds the critical strain energy release rate of the material using an appropriate mixed-mode failure criterion as discussed in section 2.

The complex state of stress at the crack tip has been investigated by Gillespie and Pipes (1984) using analytical and linear finite element analysis and by Whitcomb (1981) using nonlinear finite element analysis. Whitcomb (1981) and Ashizawa (1981) have demonstrated that delamination growth is dominated by Mode I crack extension for short deeply embedded defects. Later work (Gillespie et al. 1988) has shown, however, that Mode II may dominate delamination growth for relatively long near surface delaminations. Thus there is need for a combined crack-growth criterion that includes both Mode I and Mode II loading, when examining a through-width delamination (Gillespie et al. 1988). A conservative failure criteria used in the study is that the total $G_C = G_{IC} + G_{IIC} \approx G_{IC}$, which is typically much lower than the fracture toughness in the shear modes.

Embedded delaminations are generally the result of processing defects or impact-type damage. The through-width analysis has been extended to the embedded delamination case by

several authors (Flanagan 1988; Chai 1982; Yin and Fei 1985; Cairns 1987; Chatterjee et al. 1986). Most models study delamination growth by assuming a postbuckled shape and then using that to determine an expression for the strain energy release rate around the delamination edge, for given loading conditions (Wanthal et al. 1993). This strain energy release rate is then compared to the critical strain energy release rate of the material to determine what loads cause unstable delamination growth.

A closed-form solution for the postbuckled shape of a loaded sublaminate is available only for relatively simple assumed shapes (Wanthal et al. 1993). Thus, for more complex postbuckled shapes, which may be encountered in anisotropic plates with noncircular delaminations, finite element analysis is required to obtain an accurate solution. For circular or elliptical delamination geometries in orthotropic or isotropic plates, the closed-form analytical solutions can provide reasonably good predictions and are much less time consuming than finite element analyses.

The CSDS model employs Flanagan's criteria to examine the delamination growth failure mode. Flanagan's delamination growth model states that compression failure can be predicted by looking at a single delamination ply, located at the most critical ply interface. Thus multilevel delaminations can be simply modeled in the same way as single ply delaminations. The case of a single delamination will be examined first, and then extended to multidelaminations. Figure 44(a) shows a schematic of an elliptical delamination with major and minor axes, a and b, embedded within a square composite panel with far-field loads N_x and N_y being applied. This single ply delamination divides the panel into two sublaminates, one thick and one thin, as shown in Figure 44(b).

This is an acceptable assumption to make for thick composites, since it is unlikely that delaminations near the center will fail due to unstable delamination growth (Wanthal et al. 1993). Application of compressive loads will cause the thinner of the two sublaminates to buckle. The strain energy equation due to the applied load for a region S that includes the delaminated region, is given by (Flanagan 1988).
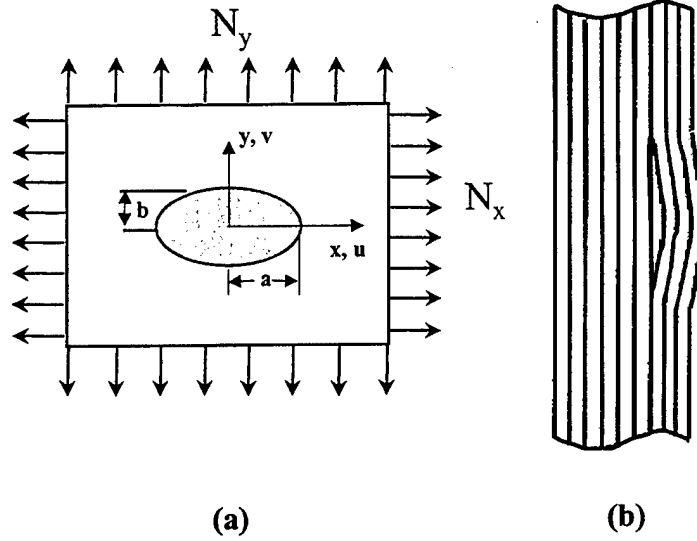
Figure 44. **Elliptical Delamination Embedded Within Square Laminate With (a) Far-Field Loads N_x and N_y and (b) Laminate Divided by Delaminate Ply Into Two Sublaminates, One Thick and One Thin.**

$$U = \frac{1}{2} \int_{-1}^{1}\int_{0}^{r}\left(\overline{\varepsilon}^T \left|A\right|\overline{\varepsilon} + 2K^T\left|B\right|\overline{\varepsilon} + K^T\left|D\right|K\right)\overline{dxdy}$$
$$+ \left(S - ab\pi\right)\left(A_{11} + 2\upsilon A_{12} + \upsilon^2 A_{22}\right){\varepsilon_x}^{02}, \tag{26}$$

where

$$\overline{\varepsilon}^T = \left(u_{,x} \quad v_{,y} \quad u_{,y} + v_{,x}\right), \tag{27}$$

$$\kappa^T = \left(-w_{,xx} \quad -w_{,yy} \quad -2w_{,xy}\right), \tag{28}$$

$$\overline{Y} = Y/b, \quad \overline{X} = X/a, \tag{29}$$

$$r = \left(1 - \overline{Y}^2\right)^{1/2}, \tag{30}$$

and

67

$$\upsilon = -\varepsilon_y^0 / \varepsilon_x^0 . \tag{31}$$

The symbols u, v, and w represent the x, y, and z out-of-plane displacements, respectively (Figure 44[a]). The A, B, D matrices are defined in the usual sense from lamination theory, and ε_x^0 and ε_y^0 represent the x and y directional strains in the parent laminate, respectively. The commas in equations 27 and 28 denote differentiation. Figure 44(a) shows the geometry and coordinate system for the elliptical delamination.

The energy equation previously derived is based on the assumption that the delaminated ply behaves as a thin membrane, with clamped boundary conditions. Therefore, the parent laminate does not bend under the compressive loading. This is a realistic assumption for thick-section laminates. Gillespie et al. (1988) investigated the effect of boundary conditions of instability-related delamination growth and found that the clamped conditions provide conservative predictions of experimental critical loads over a wide range of delamination depths and sizes. In addition, the clamped boundary conditions mean that the deflections in the elliptical delamination are governed by the strains in the parent laminate. For a more detailed mathematical explanation concerning the derivation of the strain energy equation 26, see Flanagan (1988).

Assuming that the parent laminate strains are constant and that the delamination remains elliptical as it grows, the strain-energy-release rate is obtained from the well-known equations:

$$G^a = \frac{-1}{b\pi} \frac{\partial U}{\partial a} \text{ and } G^b = \frac{-1}{a\pi} \frac{\partial U}{\partial b}, \tag{32}$$

where G^a is the total strain energy release in the a direction, and G^b is the strain-energy-release rate in the b direction (Figure 44(a)). If G^a or G^b exceeds the critical strain energy release rate (G_{IC}) for the material, the delamination will grow due to the applied loads. If G^a or G^b does not exceed G_{IC}, the load will be incremented until the failure load criterion is satisfied. For orthotropic laminates, delamination growth is predicted to occur perpendicular to the applied load, as shown in Figure 45.
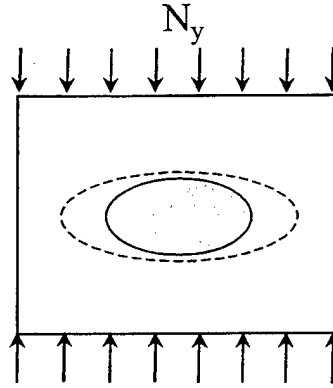
Figure 45. Delamination Growth in an Orthotropic Laminate Subjected to Unidirectional Compression.

Typical impact damaged plates will have multiple interlaminar defects. For this multidelamination scenario the analysis is quite similar, the difference being that the algorithm must now apply the aforementioned analysis for every ply interface that has delaminated. The most critical interface will be the one that gives the lowest compression load to failure. If the critical delamination is located well within the laminate, there will be other delaminations located above and below this location that could affect the sublaminate bending stiffness matrix, [D]. In order to account for the bending stiffness reduction, an empirical factor is introduced into the model that has provided excellent correlation with thin section graphite/epoxy laminates as well as thick-section S-2 glass/vinyl ester. Wanthal et al. (1993) has shown that for thin-section graphite/epoxy laminates, a 50% knockdown of the [D] matrix provides good correlation to experimental data. A 50% knockdown is also applied to the thick-section S-2 glass/vinyl-ester laminates examined in the present study.

3.3 Analysis and Verification. In this section, the analytical program is verified for the two predominant CABI modes of failure. The algorithm combines both Lekhnitskii's in-plane failure criterion and Flanagan's delamination growth failure criterion for predicting the residual compressive strength. The model requires as input the undamaged material and strength properties (E_x, E_y, v_{xy}, G_{xy}, X_c, Y_c), the Mode I fracture toughness (G_{IC}), and the size and location of the delamination. The model assumes that the damage is elliptical or circular, which

is a valid assumption as will be seen in the experimental section of this report. The model is also capable of solving for the multiple delamination case.

Two empirical factors are also needed to simulate the effects of in-plane stiffness loss due to fiber damage, and bending stiffness losses due to multiple delaminations. The in-plane stiffness knockdown is used to simulate fiber damage due to the impact event. The knockdown is entered as a percent reduction of the [A] matrix in-plane stiffness properties of the undamaged material. The bending stiffness knockdown is used to reduce the [D] matrix of the sublaminate to simulate bending stiffness losses due to multiple delaminations. For the cases presented herein, a 50% knockdown was applied to the [D] matrix based on previous results (see section 2).

Once the material properties and empirical knockdown factors are entered for the in-plane and bending stiffness loss, the CSDS algorithm begins the analysis. The code first examines the in-plane failure case. Using Lekhnitskii's complex variable solution, the model calculates the in-plane stresses at incrementally higher loads. The PSC is then used to determine failure. The failure load is taken to be the load at which the local stress exceeds the ultimate strength of the material. For the cases examined in this study, the damage size is large $\left(\dfrac{d_0}{R} << 1 \right)$ and thus the characteristic distance, d_0, is taken to be zero. In this case, the in-plane failure analysis simplifies to $\dfrac{X_C}{K_T}$, where K_T is a function of the inclusions stiffness.

Next, the CSDS code examines the delamination growth case, using Flanagan's criteria. For the multidelamination scenario, the program examines every ply interface that has delaminated at successive loads. The loads required for delamination growth at each interface are recorded, and the interface yielding the lowest delamination growth load is taken to be the delamination growth load of the laminate. Thus, as mentioned in Flanagan's postulation, failure is assumed to be controlled by a single delamination located at some critical ply interface (Wanthal et al. 1993). Ultimate failure of the laminate is taken to occur shortly after unstable delamination growth. Previous experimental studies have shown that this is a valid assumption (Flanagan 1988; Wanthal et al. 1993).

The model then compares the failure loads predicted for both the in-plane analysis and the delamination growth analysis. The lower of the two loads is taken to be the residual strength. The program gives the critical loads and strains in both the longitudinal and transverse directions, along with the failure mode. The user may specify the applied loading condition to be either one or two directional (N_x, N_y, or N_{xy} as defined in Figure 44).

3.3.1 Numerical Verification—In-Plane Analysis.

The CSDS code was numerically verified for the in-plane failure scenario using finite element analysis and experimentally verified for the delamination growth scenario. To determine the accuracy of the in-plane case, the stress concentration factor was evaluated for the case of an open hole and compared with known analytical solutions for simple plate geometries and layups. In addition, finite element analysis was used to evaluate and compare the stress concentrations for inclusions of various stiffness reductions.

Table 8 shows stress concentration values determined by the CSDS model and the theoretical solution for various notched graphite/epoxy layups. The stress concentration was determined at the hole edges normal to the direction of applied load. As expected, there is no difference between the two, since Lekhnitskii's analysis converges to the theoretical solution for an infinite plate with an open hole. The fact that the CSDS code agrees for numerous layups lends confidence to the program's validity.

Table 8. **Stress Concentration Comparison of CSDS and Theoretical Solution for Open Hole Graphite/Epoxy Systems**

Layup	K (at Hole Edge)		
	From CSDS Model	K_T^∞	% Difference
Isotropic	3.0	3.0	0.00
$[\pm 45]$	2.1	2.1	0.00
$[0_2/\pm 45]$	3.5	3.5	0.00
$[0_4/\pm 45]$	4.1	4.1	0.00
$[0_6/\pm 45]$	4.4	4.4	0.00

It must be kept in mind that the CSDS code is valid only for plates of infinite width or for plates with a width-to-hole ratio greater than four. For W/D < 4, it has been found (Wanthal et al. 1993) that significant error may accumulate.

Finite element analysis was used to determine the stress concentrations at the hole edges for various inclusion stiffnesses. See Table 8 for properties used in the analysis. The results are compared to the CSDS code in Figure 46. The FEA analysis used a width-to-hole ratio of 12 to approximate the infinite plate solution employed in the CSDS code. The notation, X*E, in Figure 46 indicates the stiffness knockdown with respect to the parent in-plane stiffnesses, where X is the knockdown factor. Thus, an X*E value of 0.4, for example, indicates that the inclusion's in-plane stiffness matrix is 60% less than that of the parent laminate. Again, the CSDS program shows good agreement for the entire range of stiffness reductions. However, comparing Figure 46 to the FEA plot of stress distribution in Figure 40, we see that there is a 13% deviation in the stress concentration factor, for W/D = 3.
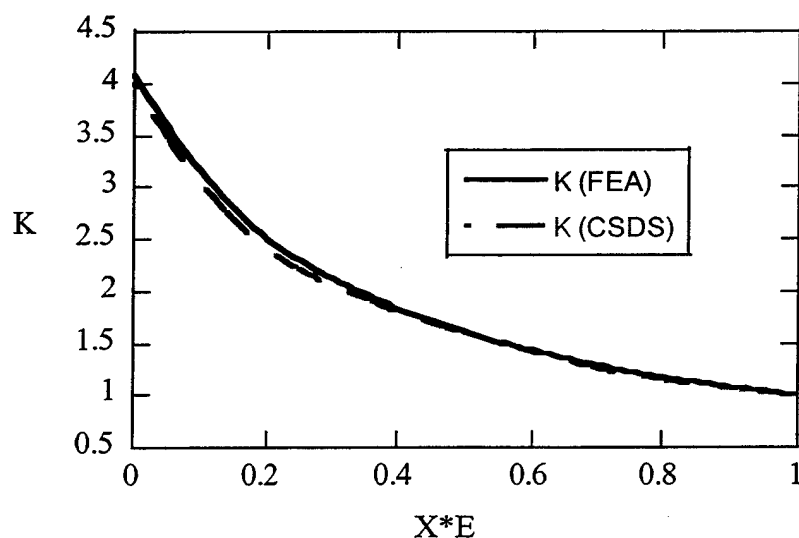
Figure 46. Stress Concentration for Various Inclusion Stiffnesses at Hole Edge Normal to Direction of Loading for Both Finite Element Analysis and CSDS. Analysis Properties Based on S-2 Glass/Vinyl-Ester Panel With an Orthotropic Layup.

To achieve good correlation with experimental data, finite element analysis was used for membrane failure predictions in order to account for finite width effects. Failure is taken to occur when, $\sigma_N = \dfrac{X_C}{K_T}$, where K_T is determined using FEA.

3.3.2 Experimental Verification—Delamination Growth Analysis.

The CSDS code was experimentally validated for the delamination growth failure analysis. Flanagan has shown that for moderate impact energies, energy levels sufficient to produce interlaminar defects without significant fiber damage, the delamination growth analysis yields good agreement with compression after impact test data of thin-section AS4/3501-6 plates (Flanagan 1988).

Compression-after-impact tests have also been conducted by Wanthal et al. (1993) on carbon IM7/977-3-toughened epoxy plates of two different layups and their strengths compared to CSDS strength predictions. Figure 47 shows a comparison of the actual compression strength vs. the CSDS predictions for various delamination sizes. The notation 48/48/4 means that 48% of the plies are 0° plies, 48% are ± 45°, and 4% are 90° plies. Similarly, the notation 32/64/4 represents the relative percentages of the 0°, ± 45° and 90° plies, respectively. Figure 47 shows that the CSDS predictions agree quite well for the fiber-dominated 48/48/4 laminate and are somewhat conservative for the matrix-dominated 32/64/4 laminate with large delaminations. A 50% bending stiffness knockdown was found to give the best correlation for this and similar carbon/epoxy systems (Wanthal et al. 1993).

The CSDS program seems to provide reasonably accurate predictions for residual compression strength for both the in-plane and delamination growth failure criteria. Up to this point the code has been used entirely on thin-section composites (less than a 6-mm thickness). In the following section, the CSDS code will be utilized in predicting residual strength and mode of failure for thick-section S-2 glass/polyester resin laminates (>18-mm thicknesses).

3.3.3 Case Study: Composite Structural Armor.

In this study, monolithic laminates of S-2 glass/polyester were impact damaged by fragment-simulating projectiles. The panel geometry
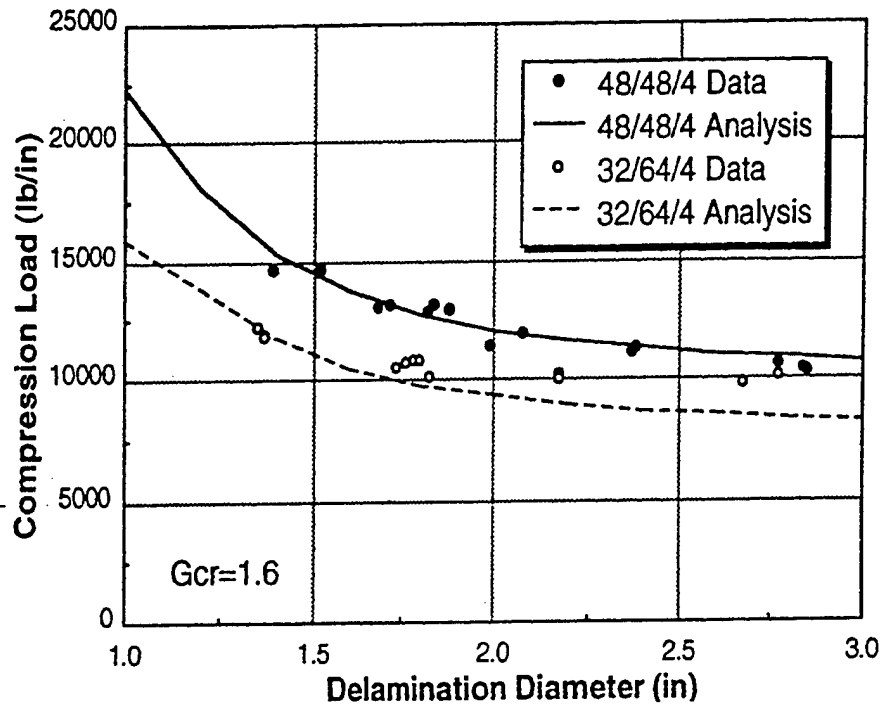
Figure 47. Compression Strength of IM7/977-3 Laminates Compared to CSDS Predictions. (For Material and Strength Properties, See Wanthal et al. [1993].)

was 0.508 m × 0.508 m × 0.044 m (20 in × 20 in × 1.73 in), or 70 plies of the glass-reinforced CYCOM prepreg. Each panel was subjected to a single shot with fragment simulators of mass 207 gr (12.7 mm in caliber) (Chou and De Luca 1993). The strike velocity ranged between 580 and 914 m/s (1,900–3,000 ft/s) to obtain different levels of damage. The damaged panels were then nondestructively inspected by CT. In essence, the CT image is a representation of x-ray attenuation at specific slice planes through the thickness. The attenuation is almost entirely due to density variations caused by the impact and hence can also be viewed as a density map.

After ballistic testing and inspection, compression tests were performed. The fixture used to test the panels is a modified version of a compression fixture developed by NASA. The panels were placed in the fixture and gripped on all four sides. The side grips provide stability to avoid global buckling. The top and bottom grips are used to prevent premature failure by end crushing. The panels were tested by edge-wise compression. In other words, the long axis of the panel was parallel to the direction of loading (Chou and De Luca 1993).

74

Results from the experimental study were then compared to the CSDS predictions. Material properties and fracture toughness values were readily available from the literature and are listed in Table 9 (Chou and De Luca 1993; Martin 1997). From the CT scans, damage profiles at different depths were generated from each panel (Figure 48). The image in Figure 48 was taken in 2.0-mm intervals through-thickness, for a total of 19 slices. To compare the experimental and predicted residual strengths, average delamination sizes were taken over all slices and an equivalent diameter defined.

Table 9. Material and Strength Properties for S-2 Glass/Polyester

S-2 Glass/Polyester	Plain Weave Fabric
G_{IC}	100–550 J/m^2
E_x, E_y	27.6 GPa
E_z	8.00 GPa
v_{xy}, v_{yz} v_{xz}	0.28
G_{xy}, G_{yz}, G_{xz}	3.03 GPa
X_T, Y_T	542 MPa
X_c, Y_c	150 MPa
Ply thickness	0.64 mm
Ply count	69

Once material/strength properties and delamination diameters were obtained, the model was used, assuming multilevel delaminations. The compression strengths were then compared to actual CAI data taken from Chou and De Luca (1993). Figure 49 shows a plot of compression strength vs. delamination diameter for the various G_{IC} values and stiffness reductions. The experimental results are superimposed on this figure. The model strength prediction of 153 MPa (22.2 ksi) agrees well with the no-defect panels tested, with a variance of 8.3%.

Figure 49 indicates that good agreement exists between the experimental results and the model predictions for small G_{IC} values. These smaller G_{IC} values are often termed the "initiation toughness regime," since they represent G_{IC} values for small crack lengths (Figure 50). Results in Figure 49 show that residual strength drops 50 to 73% of ultimate strength for delamination diameters ranging from 4 to 12 in (0.10 m to 0.30 m), respectively.
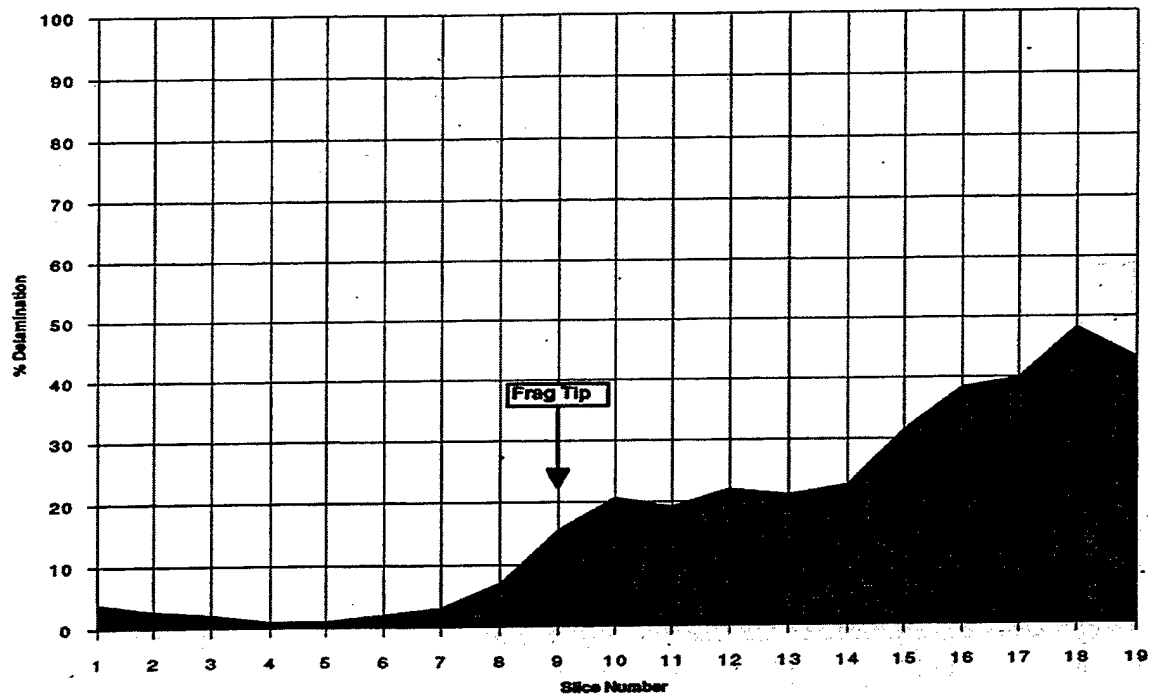
Figure 48. Delamination Profile Through the Thickness (Chou and DeLuca 1993).
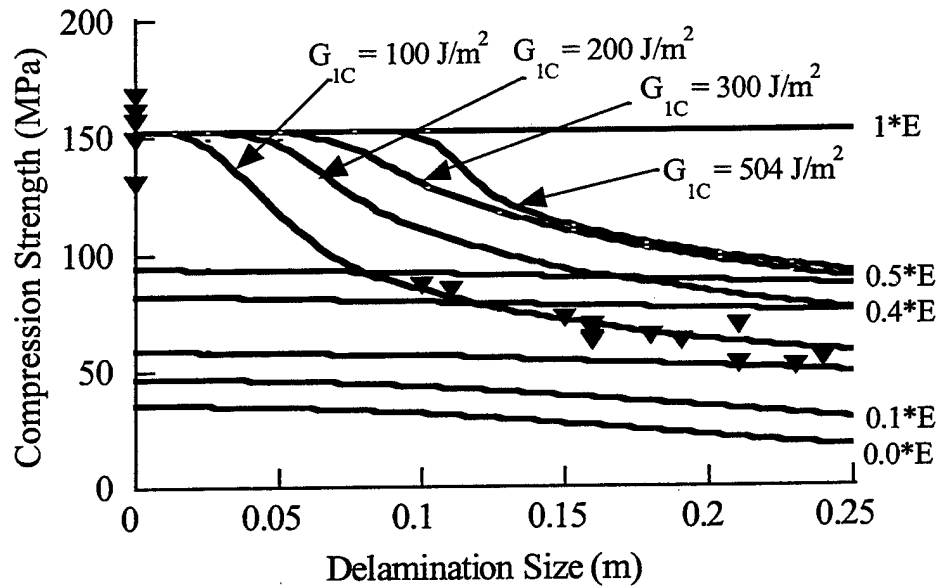
Figure 49. Model Predictions for Strength vs. Delamination Diameter. Points Represent Experimental Results.
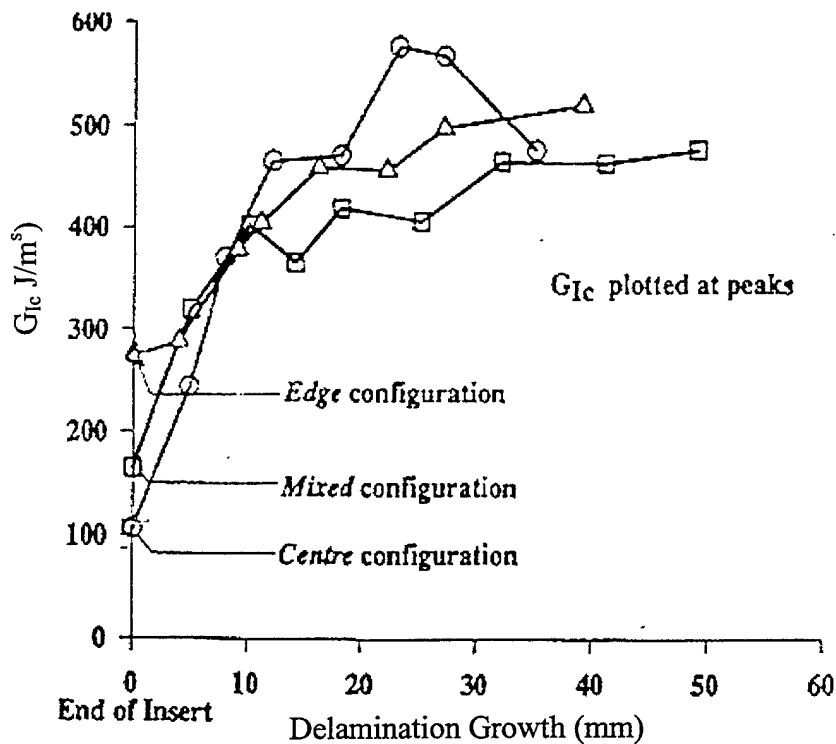
Figure 50. G_{IC} (J/m^2) vs. Delamination Growth (Millimeters) for Nonstitched Double Cantilever Beam (DCB) Specimens (Martin 1997).

Figure 49 also shows the model predictions for in-plane failure. Each of the relatively flat lines represents a different stiffness knockdown for the damaged area. For example, the designation 0.1 × E indicates that the inclusion stiffness is reduced 90% from that of the parent laminate. The experimental data falls between the lines representing 0.25 × E and 0.5 × E stiffness reductions. Data on the stiffness losses in the damaged region is unavailable from these references to determine whether the model is indicating membrane failure as a possible failure mode. The trend of the data would seem to indicate however, that the predominant failure mode is unstable delamination growth.

The previous case study indicates that improving G_{IC} by methods such as through-the-thickness stitching can improve residual strength when the predominant failure mode is delamination growth. In addition, improving G_{IC} improves the multihit capabilities of a composite component by reducing the damage area, as will be shown in section 4.

77

3.3.4 Critical Defect Size for S-2 Glass/Polyester CYCOM. The analytical algorithm was used to determine the critical defect size for the S-2 glass/polyester CYCOM system discussed in the previous section. It is assumed that delamination growth failure governs failure. Recall that a critical defect is defined as the extent of damage that a structure may withstand and still be structurally functional (i.e., maintain its compression strength to above the design allowable). Figure 51 shows the compression strain in the load direction (x) as a function of delamination size, for a range of biaxial loading conditions. A G_{IC} value of 500 J/m^2 (2.87 in lb/in^2) is used in conjunction with the properties for an S-2 glass/polyester CYCOM laminate (see section 4). A N_y/N_x value of 0.0 indicates unidirectional compression loading in the x direction (Figure 44), while $0 < N_y/N_x < 1$ indicates biaxial compression loading in both the x and y directions. A value of -0.5 indicates tension loading in the y direction and compression loading in the x direction.
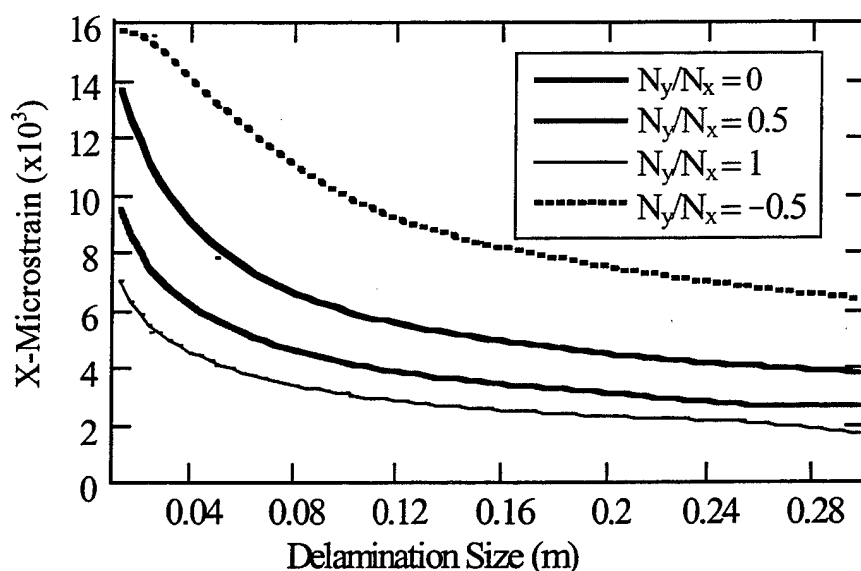
Figure 51. **Influence of Delamination Size and Loading Condition on Failure Strain for the Case of an S-2 Glass/Polyester CYCOM Laminate. The Failure Mechanism Is Assumed to Be by Delamination Growth.**

Taking a 5,000 microstrain to failure, which is the compression design allowable used for the CAV, Figure 51 shows the critical delamination sizes that initiate instability-related delamination growth. Depending on the loading condition, critical delamination size can range from 0.0762 m

78

(3 in) for the biaxial compression (N_y/N_x = 1) to 0.3048 m (12 in) for unidirectional loading (N_y/N_x = 0). Thus biaxial loading can cause a severe reduction in the critical delamination size. Figure 52 shows the effect of fracture toughness and delamination size on the critical strain to failure for a fixed loading condition of N_y/N_x = 0 (unidirectional compression). For any given delamination size, increasing G_{IC} increases the critical strain to failure. This is the main motivation for the use of stitching, since through-the-thickness stitching provides a significant increase in G_{IC}, as will be shown in section 4.
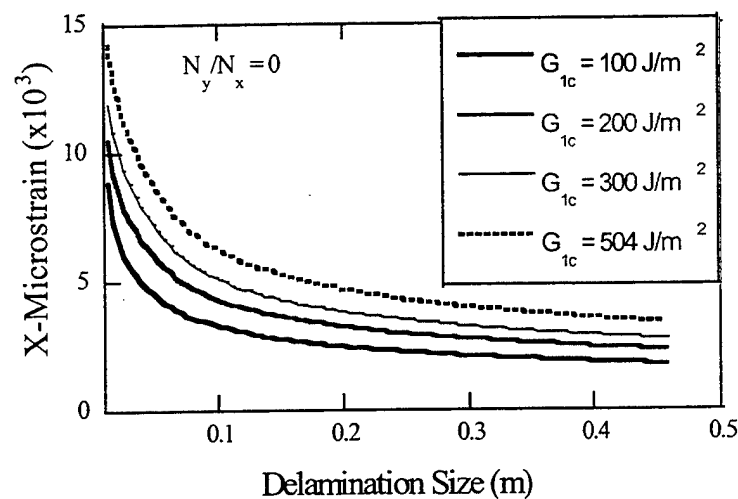
Figure 52. Effect of Fracture Toughness and Delamination Size on Delamination Growth.

By varying G_{IC} and taking the critical delamination size at 5,000 microstrain for each of the different loading conditions, a plot of critical delamination size vs. G_{IC} is generated as shown in Figure 53. The intermediate loading condition of N_y/N_x of 0.5, for example, indicates that for a fracture toughness between 100–500 J/m^2 (0.57–1.71 in lb/in^2) for the S-2 glass/polyester, the critical delamination size is roughly between 0.03–0.08m (1–3 in) in diameter. In all cases for loading condition, as G_{IC} increases so does the tolerable damage size. Experimental testing in section 4 has shown that the fracture toughness for vinyl-ester systems is between 1,000 and 1,200 J/m^2. In this case, the critical delamination sizes range from 0.11–0.15 m (3.7–5 in). Data also shows that for stitched vinyl-ester systems, G_{IC} can reach values as high as 10,000 J/m^2, depending on the stitch spacing.
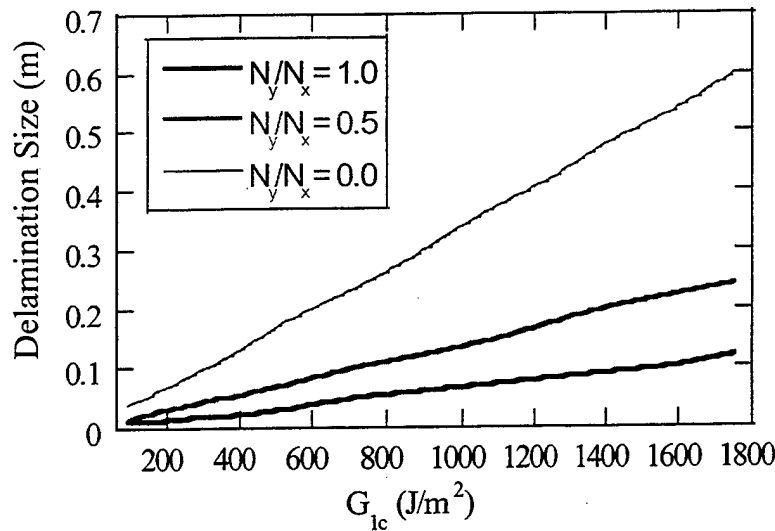
Figure 53. **Critical Delamination Size vs. Strain Energy Release Rate for 5,000 Microstrain (0.5% Strain to Failure).**

Although improving G_{IC} greatly increases residual strength for instability related delamination growth failure mode, higher fracture toughness may cause extensive stiffness reductions in the damaged region upon ballistic impact. This results in the development of a high stress concentration, which may lead to membrane failure upon compression loading. Thus achieving the maximum fracture toughness is not necessarily advantageous. The desired degree of improvement in fracture toughness depends on the relative importance of ballistic tolerance to residual strength.

One possible means of improving both ballistic tolerance and residual strength is with the use of through-the-thickness stitching. A high stitch density leads to large increases in G_{IC}. but may also cause a reduction in the in-plane inclusion stiffness. The stiffness reduction leads to an increase in K_T and a transition in failure mode from unstable delamination growth to membrane failure. Since K_T is inversely related to notched strength $\left(\sigma_N = \dfrac{X_C}{X_T} \right)$, further increases in K_T result in lower strength. Therefore, the optimal stitch density is such that G_{IC} is increased to the

80

transition point from delamination growth failure to membrane failure. Further increases in G_{IC} are not beneficial and in fact may be detrimental to CABI strength.

The following section presents an experimental study conducted to examine methods of improving damage tolerance and residual strength, with particular emphasis on the effects of through-the-thickness stitching. The analytical and finite element models are also utilized to gain an understanding of the CABI modes of failure.

4. Experimental Study

4.1 Introduction. In the previous section an analytical technique was introduced and validated numerically and experimentally for thin-section carbon/epoxy laminates. In addition, a case study was considered in which S-2 glass/CYCOM 4102 prepreg panels were ballistically impacted and tested under unidirectional compression. From this work and the analysis, it was concluded that further experimental work is needed to determine the CABI modes of failure. In addition, experiments have been carried out to determine the effect of through-the-thickness stitching and ceramic tiles on arresting damage development upon ballistic impact and on improving residual strength.

Three different resin systems were investigated for their ballistic performance in various combinations with two different S-2 glass fabrics. The resin systems and glass preforms were chosen based on previous usage on military vehicles as well as for proposed usage on future vehicles. A comparison is also made between the S-2 glass/polyester CYCOM prepeg and the SCRIMP-processed S-2 glass/vinyl-ester panels. The 18-oz twill weave S-2 glass/resin systems were tested with ceramic tiles bonded. Detailed descriptions of the laminate types tested follow. Further studies were performed with the S-2 glass/vinyl-ester systems to determine the stress distribution under compression loading. This was done in an effort to determine the CABI failure modes.

In this section, details of the experimental testing are presented. Subsection 4.2 describes the types of panels tested and the ballistic testing specifications. Subsection 4.3 discusses the results of the NDE studies to determine the state of damage through the thickness of the panels, and in order to evaluate the effect of different resin types and through-the-thickness stitching in reducing damage size. In addition, the 24-oz S-2 glass/CYCOM polyester prepreg laminates are also compared to the SCRIMP-processed 20-oz S-2 glass/vinyl-ester 411-C50 laminates, for their ballistic performance. Subsection 4.4 presents the results of the CABI tests.

Further tests to determine material and strength properties were also performed on the 24-oz S-2 glass/vinyl-ester laminates to examine the extent of stiffness loss and the CABI modes of failure. The baseline compression strength properties are presented in subsection 4.4 along with the CABI results, and the material properties are presented in subsection 4.5. In subsection 4.5.2, the in-plane stiffness loss is measured by experimentally measuring the strain distribution under compression loading and superimposing the data with FEA calculations. Subsection 4.6 summarizes the main results of section 4.

4.2 Impact Testing.

4.2.1 Panel Specifications and Types Tested. Five composite systems were investigated for their ballistic performance and compression after impact properties. In addition, through-the-thickness Kevlar stitching and in some cases, ceramic tiles were used with the vinyl ester and SC-4 resin systems. Table 10 summarizes the different panel types investigated.

Table 10. Panel Types and Number of Panels Tested

Panel Type	No Tile, No Stitch	No Tile, Stitched	Tiled, No Stitch	Tiled, Stitched
18-oz S-2 Glass/Vinyl Ester	5	4	2	2
24-oz S-2 Glass/Vinyl Ester	5	5	0	0
18-oz S-2 Glass/SC-4	4	2	2	2
24-oz S-2 Glass/SC-4	5	5	0	0
24-oz S-2 Glass/CYCOM 4102 Prepreg	3	0	3	0

Due to the limited supply of fabric, it was not possible to perform a complete ballistic study on panels with ceramic tiles. However, a few tiled panels were tested for explanatory purposes. Panels were made with 18-oz S-2 glass/vinyl ester used in the CAV and its performance compared with the 24-oz S-2 glass/CYCOM polyester prepreg used in the CIFV. In addition, the SCRIMP process was used to manufacture 18-oz and 24-oz S-2 glass systems using both SC-4 epoxy resin and vinyl-ester 411-C50. The SCRIMP technique has been shown (Fink et al. 1998) to have lower manufacturing costs compared to manual layup of CYCOM prepreg. In this study, the ballistic and CABI performances of the SCRIMP panels are shown to be equivalent to those of the CYCOM prepreg.

The manufacturer's fabric designation of 24-oz or 18-oz indicates that the fabric weighs 24-oz and 18-oz/yd^2, respectively. The 24-oz S-2 glass is a 5 × 5 plain weave fabric, while the 18-oz S-2 glass is a 2 × 2 twill weave (shown in Figure 9). The CYCOM 4102 resin is a polyester resin manufactured by Cytec Fiberite.

Panels made with the vinyl-ester and SC-4 epoxy resins were manufactured using the SCRIMP process. Details of the SCRIMP process and the cure cycles for the different resin systems were given in section 2. The stacking sequence of the fabric weave was taken to be unidirectional yet with orthotropic properties, since each ply has approximately the same properties in the longitudinal and transverse directions, discounting the effects of fiber undulations. The CYCOM polyester resin panels were manufactured using prepreg material. An overall areal density of 7 psf was maintained for all panels. To achieve this, 40 layers of fabric were laidup for the 18-oz fabric, and 30 layers for the 24-oz fabric.

The stitched panels were fabricated using a MIL-T-87128 (Department of Defense 2000), 3-cord, soft, Kevlar thread (2,000 denier). The dry preform was stitched in both the longitudinal and transverse directions forming a 1-in square grid pattern. Further details on the stitching procedure can be found in subsection 2.1.2.

Tiled panels were manufactured in the same manner previously mentioned, with the addition of a single AD95 alumina hex tile bonded to center of the panel surface using a two-part epoxy-based adhesive (Figure 54) cured at room temperature. Glass beads (0.4 mm–0.6 mm) were used as spacers to control the thickness of the bondline.
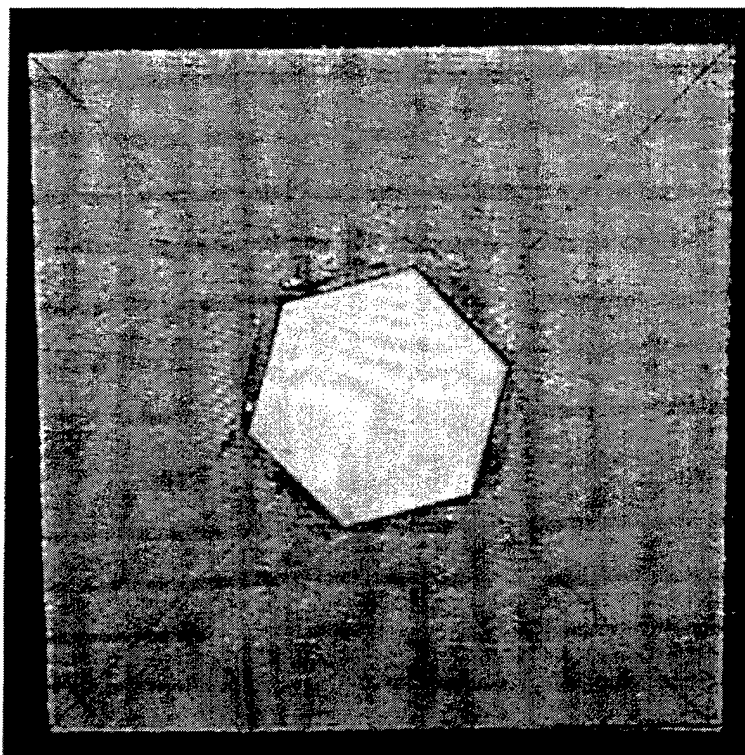
Figure 54. Front Surface of a Stitched 18-oz S-2 Glass/Vinyl Ester With AD95 Alumina Hex Tile Bonded to the Center.

The fiber volume fraction of the different panel types was also measured for the 24-oz S-2 glass panels to compare the SCRIMP process to manual layup of the polyester CYCOM prepreg, which also used 24-oz S-2 glass. Stitched panels exhibited the highest fiber volume fraction and the SCRIMP panels showed the least volume of void content, while the CYCOM prepreg exhibited the highest void content. Stitching causes the dry preform to be compressed, thus resulting in a higher fiber volume fraction. The results follow in Tables 11–13.

Table 11. Fiber Volume Fraction, 24-oz S-2 Glass/Vinyl-Ester Panels

Sample ID	Fiber Volume (%)	Resin Volume (%)	Void Volume (%)
Sample 1	47.1	52.1	<1.0
Sample 2	46.7	52.6	<1.0
Sample 3	46.8	52.5	<1.0
Sample 4	46.9	52.3	<1.0
Sample 5	46.7	52.7	<1.0
Average	46.8	52.5	<1.0

Table 12. Fiber Volume Fraction, Stitched 24-oz S-2 Glass/Vinyl-Ester Panels

Sample ID	Fiber Volume (%)	Resin Volume (%)	Void Volume (%)
Sample 1	54.61	44.93	<1.0
Sample 2	54.59	44.91	<1.0
Sample 3	54.98	44.44	<1.0
Sample 4	54.19	45.17	<1.0
Sample 5	55.11	44.35	<1.0
Average	54.7	44.76	<1.0

Table 13. Fiber Volume Fraction, 24-oz S-2 Glass/Polyester CYCOM 4102 Panels

Sample ID	Fiber Volume (%)	Resin Volume (%)	Void Volume (%)
Sample 1	54.45	39.76	5.80
Sample 2	54.41	39.60	5.98
Sample 3	54.56	39.09	6.35
Sample 4	54.34	39.60	6.06
Sample 5	54.41	39.28	6.31
Average	54.43	39.47	6.10

4.2.2 Ballistic Specifications. All nontiled panels were shot using a 12.7 mm (.50 cal.) FSP. All panels were shot at a constant velocity of 1,550 ft/s. The velocity chosen was based on V50 testing reported by Fink and Gillespie (2000). V50 testing is done in order to determine the

velocity at which a projectile has a 50% chance of perforating a target at normal incidence (Hetherington and Lemieux 1994). Once the V50 values were determined, the velocity was reduced by approximately 200 ft/s to guarantee incomplete penetration. Incomplete penetration is desired to simulate damage that would occur in an armor system where the projectile is arrested and causes extensive back surface delaminations. Detailed compilation of the V50 results can be found in Fink and Gillespie (to be published). All ballistic tests were performed in accordance with NIJ Standard 0101.03 (U.S. Department of Justice 1987). Velocity was determined using light screens and a chronograph as described in section 2.

Because of the light powder charge in the projectile case, impact velocity varied somewhat. The average V50 value for all resin systems is 1,710 ft/s, with a standard deviation of 84 ft/s. For the constant velocity testing, an average value of 1,590 ft/s was used with a standard deviation of 41 ft/s. A summary of the V50 test results is presented in section 2. The testing velocity for the tiled panels was 2,700 ft/s raised 1,150 ft/s from the non-tiled case, in addition to increasing the projectile size to a 20-mm FSP to impart a significant level of damage for subsequent CABI testing.

4.3 NDE. Once the composite panels were ballistically tested, NDE was performed to determine the state of damage through the thickness of the panel. Before scanning each panel with a 5-MHz-focused transducer, it was necessary to scrub the surface while the panel was fully immersed in the water tank to remove any air bubbles that could affect the quality of the signal. From these inspections, comparisons can be made as to the relative effectiveness of stitching and different resin systems at arresting damage growth.

4.3.1 Vinyl-Ester Panels. NDE was performed on the various vinyl-ester composite systems. Damage evaluations were made at three different depth locations, or gates. The location of gate 1 was taken just below the impact surface, at a depth approximately 10% of total thickness. Gate 2 was located at the middle of the panel, while gate 3 was located near the back face at a depth approximately 80% of total thickness. Figure 55 shows a C-scan of a nonstitched 18-oz S-2 glass/vinyl-ester system, at the various depth locations. The damaged areas seen in

(a)   (b)

(c)
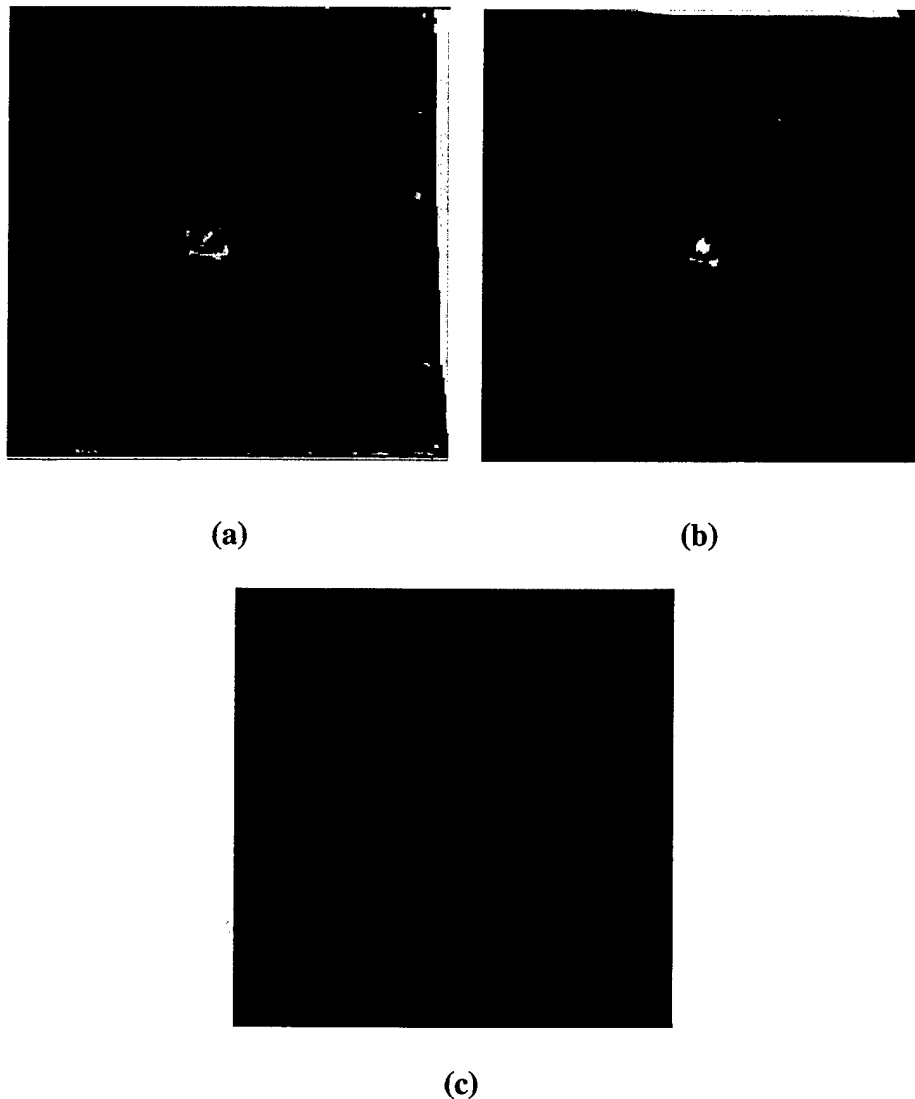
Figure 55. Ultrasonic Image at (a) Gate 1, (b) Gate 2, and (c) Gate 3 for the 18-oz S-2 Glass/Vinyl-Ester Panel. Shot With .50 cal. FSP at 1,550 ft/s.

these C-scans are most representative of delamination damage. It is difficult to see other types of damage, such as fiber pullout and fiber breakage, using ultrasonic scans. Thus, other means are necessary to determine the extent of fiber damage and stiffness loss, as will be discussed subsequently. The scans (all shown with a scale of 1:5) indicate that the largest delaminations are near the back face, at gate 3 (Figures 55–58). The delamination pattern through the thickness seems to be conical, with the smallest delaminations near the projectile entry surface and the largest delaminations near the back surface. At each ply location, the damaged area is
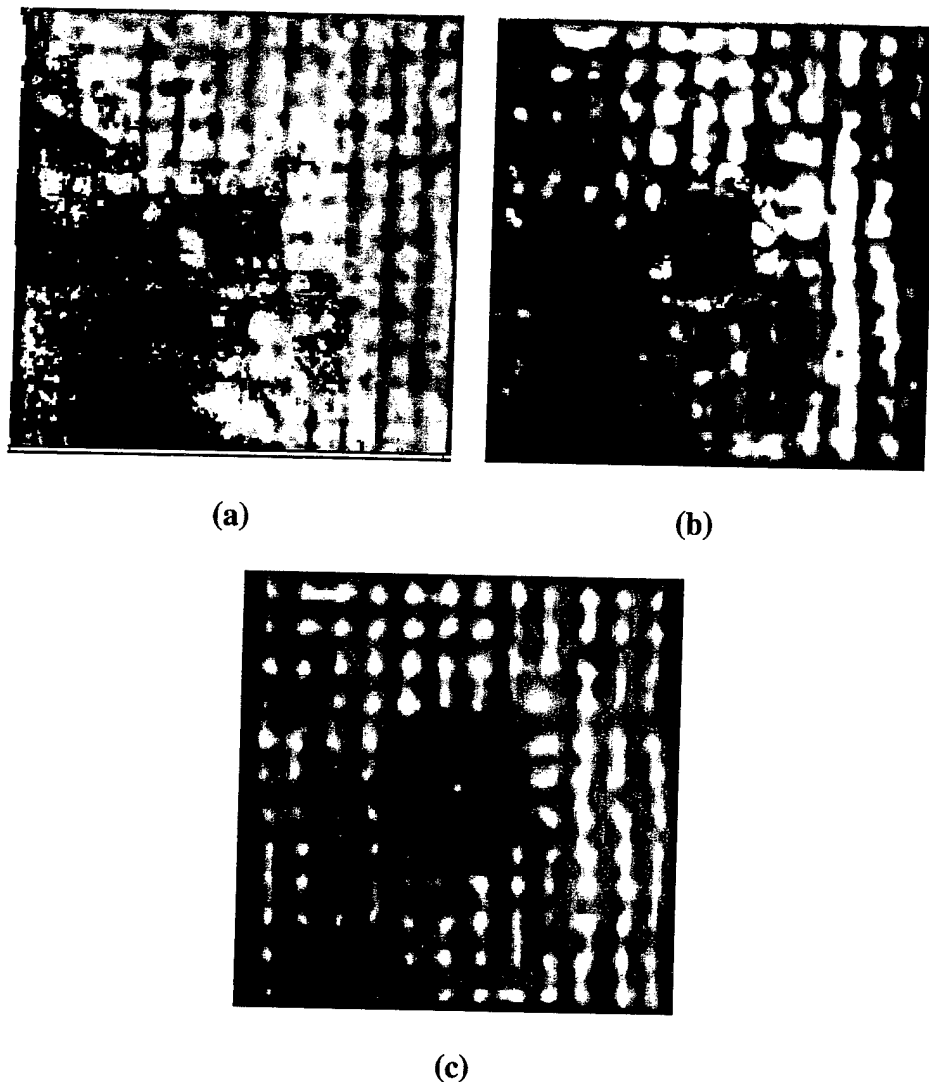
Figure 56. Ultrasonic Image at (a) Gate 1, (b) Gate 2, and (c) Gate 3 for an 18-oz S-2 Glass/Vinyl-Ester Panel, Stitched in a 1-in-Square Grid Pattern. Shot With .50 cal. FSP at 1,550 ft/s.

approximately circular and located near the center of the panel. The damage pattern was similar for the 24-oz panels, although the average damage size was slightly smaller. Tabulated results of the damage percentages at each gate location in the various laminate systems are presented in Tables 14 and 15 of subsection 4.3.3.

Figure 56 shows ultrasonic images for an 18-oz S-2 glass-stitched vinyl-ester panel. The damage pattern through the thickness for the stitched panels is similar to the nonstitched panels

88

(a)   **(b)**

(c)
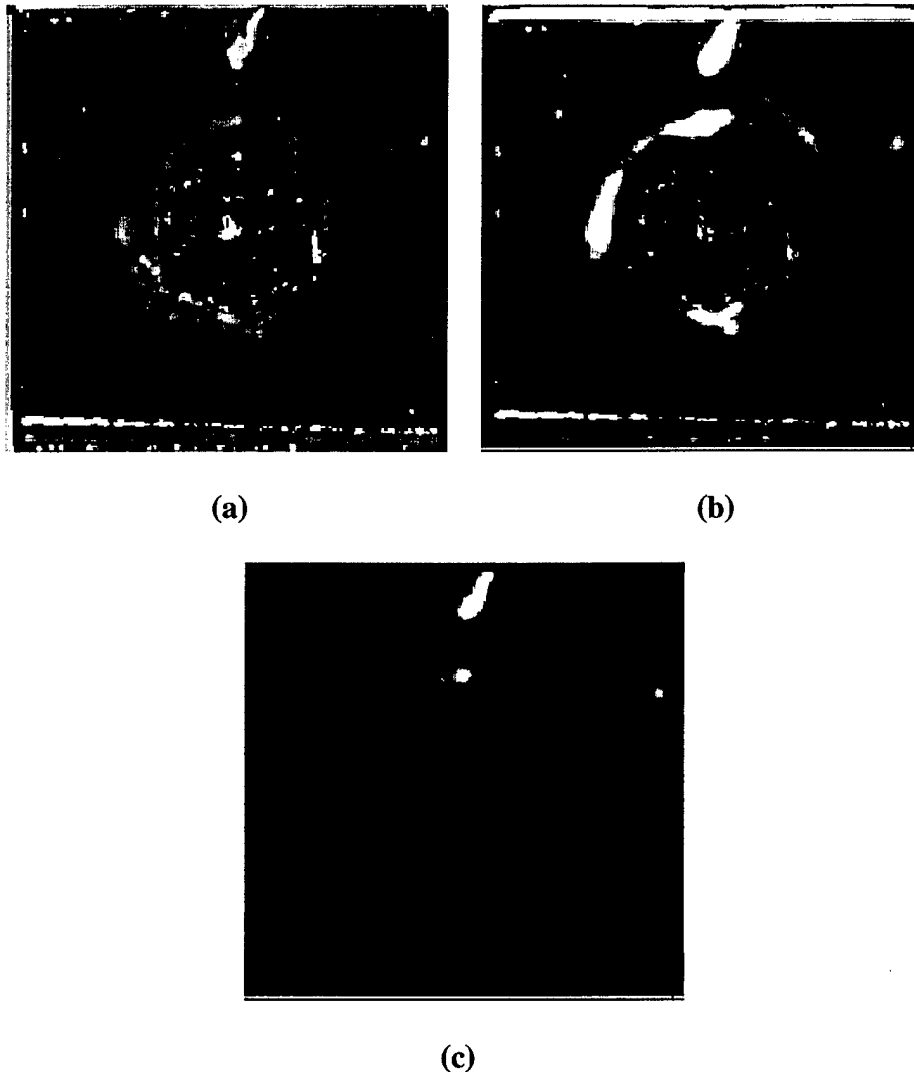
Figure 57. **Ultrasonic Image of (a) Gate 1, (b) Gate 2, and (c) Gate 3 of 18-oz Vinyl-Ester Panel With Tile. Shot With 20-mm FSP at 2,700 ft/s.**

although the damage size is smaller. On average, the stitched panels reduced the average delamination diameter by 21.4–28.6%. Some stitched rows near the center of the panels and on the back surface were broken and pulled out from the matrix.

Figures 57 and 58 show the effect of the ceramic tile on damage size for both the nonstitched and stitched 18-oz/vinyl-ester cases, respectively. The hexagonal shape seen in gate 1 is the outline from the epoxy adhesive of the ceramic tile. Damage from gate 2 can be faintly seen on the C-scan image of gate 1.

(a)   (b)

(c)
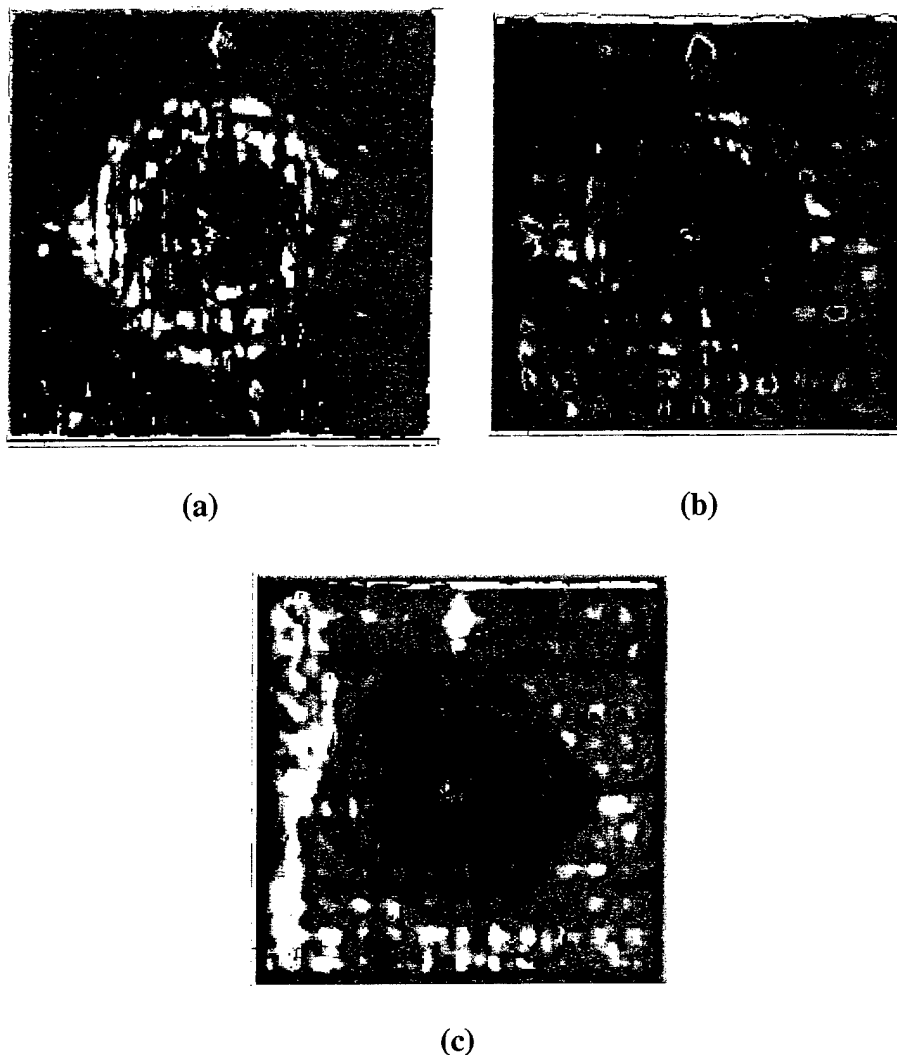
Figure 58. Ultrasonic Image of (a) Gate 1, (b) Gate 2, and (c) Gate 3 of 18-oz Vinyl-Ester Panel With Tile and Stitches. Shot With 20-mm FSP at 2,700 ft/s.

Comparing these images to the nontiled panel shown in Figure 55, it can be seen that the delamination size distribution through the thickness tends to be cylindrical rather than conical, as was the case for the nontiled panels. Figure 58 shows a C-scan of a vinyl-ester panel with both stitching and tile. The stitching reduces the delamination size when compared to the nonstitched/tiled panel of Figure 57, and again the damage size distribution through the thickness is fairly uniform and circular. A more detailed discussion and comparison of the damage profiles is given in subsection 4.3.3.

Table 14. Percent Damage Area at Each Gate Location for 18-oz S-2 Glass Systems

Panel Type	Projectile Size (FSP)	Gate 1 (%)	Gate 2 (%)	Gate 3 (%)
Vinyl Ester	.50 cal.	3.7	16.7	17.1
Vinyl Ester, With Stitching	.50 cal.	3.3	9.8	12.8
Vinyl Ester, With Tile	20 mm	26.7	29.9	33.3
Vinyl Ester, With Stitching and Tile	20 mm	2.8	11.4	25.4
SC-4	.50 cal.	3.3	15.8	31.8
SC-4, With Stitching	.50 cal.	2.2	11.7	14.98
SC-4, With Tile	20 mm	—	40.3	46.6
SC-4, With Stitching and Tile	20 mm	—	22.1	36.9

Table 15. Percent Damage Area at Each Gate Location for 24-oz S-2 Glass Systems

Panel Type	Projectile Size (FSP)	Gate 1 (%)	Gate 2 (%)	Gate 3 (%)
Vinyl Ester	.50 cal.	2.7	12.6	14.0
Vinyl Ester, With Stitching	.50 cal.	2.1	8.8	9.4
SC-4	20 mm	5.0	12.4	14.6
SC-4, With Stitching	20 mm	3.3	10.4	10.99
CYCOM	.50 cal.	7.0	43.5	70.0
CYCOM, With Tile	20 mm	13.9	33.6	48

4.3.2 SC-4 and CYCOM Panels. The delamination patterns through the thickness for the SC-4 systems are very similar to those of the vinyl-ester panels, although the 18-oz S-2 glass/ SC-4 panels showed much larger delaminations near the back surface (see the Appendix). As with the vinyl-ester systems, panels made with the 24-oz S-2 glass exhibited slightly smaller delamination sizes when compared to 18-oz S-2 glass. The delamination sizes of the CYCOM panels were significantly larger than the SCRIMP-processed vinyl-ester and SC-4 epoxy laminates. The Appendix shows ultrasonic images of the various SC-4 panels and CYCOM panels at gate 3, which is located at a depth approximately 80% of total thickness. Subsection 4.3.3 will present a summary and comparison of the delamination sizes for the various systems.

4.3.3 Delamination Size Comparisons. Figures 59–61 show plots of damage distribution through the thickness for the stitched and nonstitched 18-oz and 24-oz S-2 glass/systems, and the stitched and nonstitched tiled 18-oz S-2 glass/systems. Figures 59 and 60 depict plots of the nontiled 18-oz and 24-oz S-2 glass/systems (.50 cal. FSP at 1,550 ft/s), respectively. Figure 61 shows the case for the tiled 18-oz S-2 glass/systems (20 mm FSP at 2,700 ft/s). The damage is recorded as percent area at each gate location.
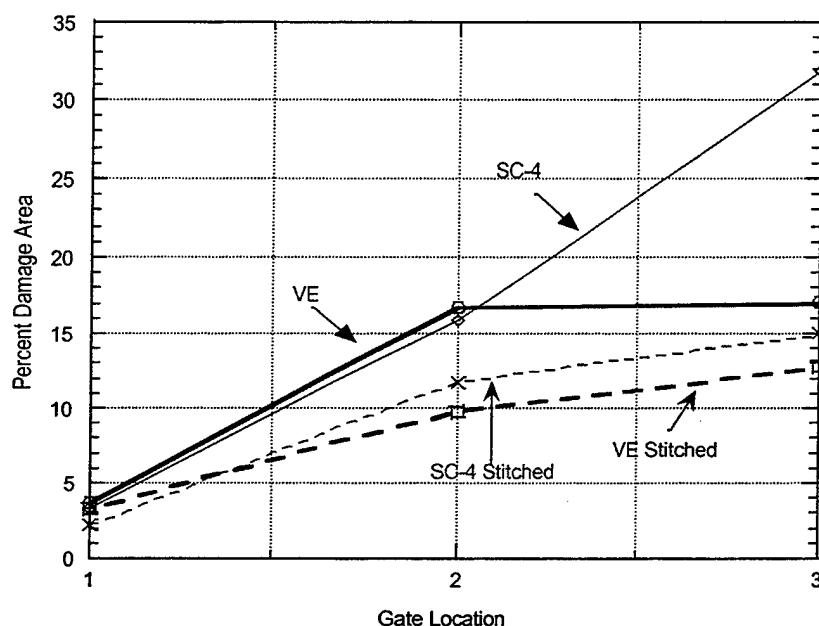
Figure 59. Damage Distribution Through the Thickness for 18-oz S-2 Glass Systems With No Tile Bonded Impacted With .50 cal. FSP at 1,550 ft/s.

For the nontiled systems in Figures 59 and 60, the damage size increases rapidly from the entry point to the midpoint and tapers off near the back surface, giving the damage area a conical shape through the thickness. The only exceptions were the nonstitched 18-oz SC-4 panels (Figure 59), which delaminated significantly near the back surface. Stitching in both the vinyl-ester and SC-4 cases reduced damage area. The damage area at gate 3 on the nonstitched 18-oz vinyl ester is 17% less than that of the nonstitched SC-4. This indicates that the fracture toughness significantly influences the distribution of damage through the thickness. Results for the stitched panels are also shown in Figure 59. The extent of damage is reduced and the
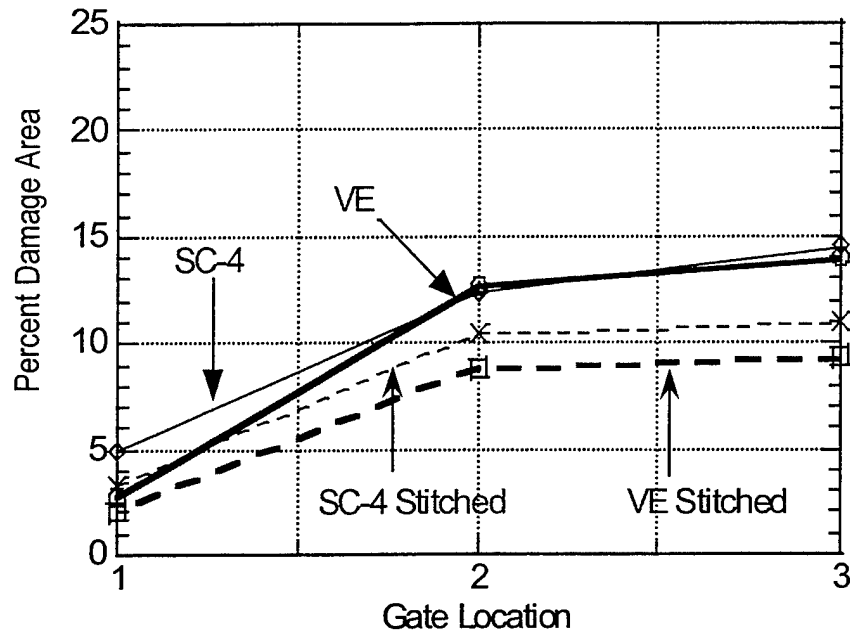
Figure 60. Damage Distribution Through the Thickness for 24-oz S-2 Glass Systems With No Tile Bonded Impacted With .50 cal. FSP at 1,550 ft/s.
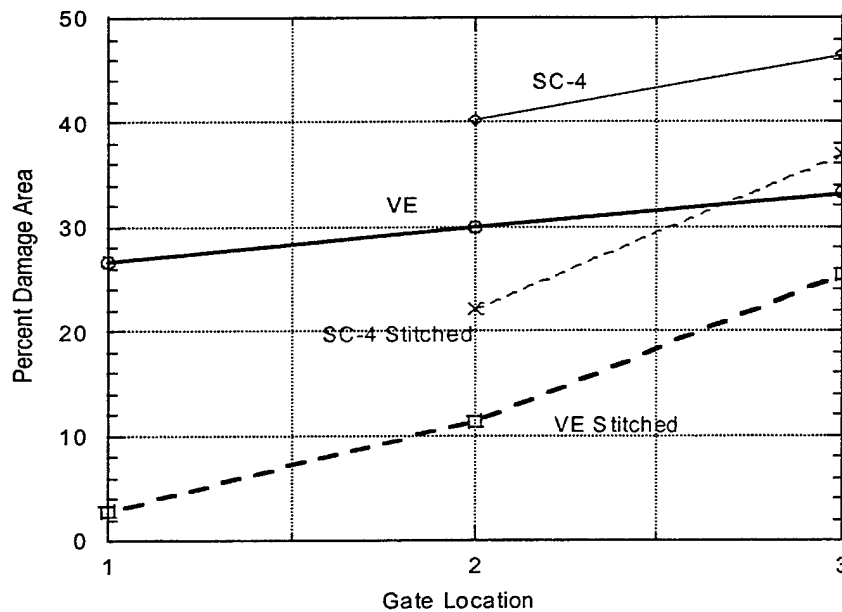
Figure 61. Damage Distribution Through the Thickness for 18-oz S-2 Glass Systems With Tile Bonded Impacted With 20-mm FSP at 2,700 ft/s.

difference between the vinyl ester and epoxy is decreased and the large back surface delamination is arrested by the stitching.

Figure 60 presents the results for the 24-oz S2-glass fabric. Results in Figure 59 indicate that this fabric provides superior damage tolerance compared to the 18-oz fabric.

In Figure 61, the damage area for tiled panels subjected to 20 mm FSP at 2,700 ft/s is presented. In this case, the projectile does not penetrate the backing plate. Overall damage area is less and stitching provides modest improvement. Figure 61 shows that the damage area through the thickness increases linearly and more uniformly than in the nontiled cases, giving the damage a cylindrical shape through the thickness. The difference in damage profile is likely because the projectile did not penetrate the specimen in the tile case as it did in the nontiled case. Thus, the damage in the tile case is mostly due to the stress wave propagation, whereas in the nontile case the penetration of the projectile causes interlaminar cracks to propagate. Stitching is found to be effective in this case as well.

Figure 62 shows the damage distribution in the 24-oz CYCOM systems—both with and without tiles. The damaged area is significantly higher in the CYCOM panels, indicating that the SCRIMP process offers superior ballistic performance. In the case of the CYCOM panels (Figure 62) both tiled and nontiled panels exhibited a conical damage distribution through the thickness.

Tables 14 and 15 (see subsection 4.3.1) summarize the percent area of damage at each gate location for the various systems. The delamination area at each gate location was calculated by using Corel PHOTO-PAINT imaging software. The software first calculates the number of pixels in the entire gate image and then divides by the number of pixels in the damaged region to give a percentage. The damaged region must of course be specified through the users own assessment of the image.
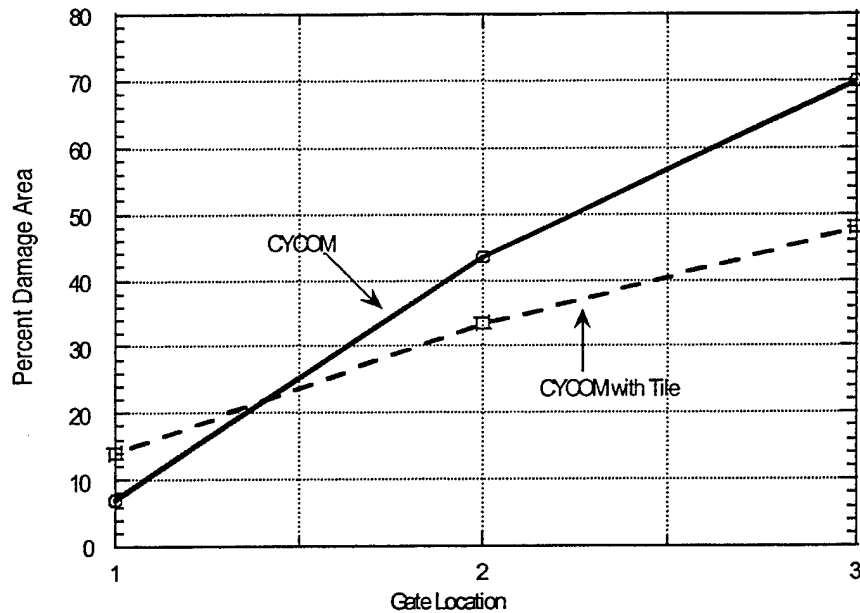
Figure 62. Damage Distribution Through the Thickness for 24-oz S-2 Glass/CYCOM Polyester Systems With and Without Tile Bonded Impacted With .50 cal. FSP at 1,550 ft/s for Nontiled Panels and 20-mm FSP at 2,700 ft/s for Tiled Panels.

To make bar chart comparisons (Figures 63–65) of the average delamination size through the thickness for the various composite systems, averages were taken from the gate 2 and gate 3 readings. The image from gate 1 was excluded, since the damage near the front face is not significant in any of the panels. Since the damage in the panels is roughly circular and the analytical models used to predict compression strength assume that the damaged region is elliptical, the percent damaged area was plotted in terms of delamination diameter.

Figure 63 shows a bar graph comparison for the various non-tiled resin systems with the 18-oz S-2 glass fabric. On average, the stitched vinyl-ester panels showed the least amount of delamination followed by the stitched SC-4 panels. This difference is mostly due to the extensive back-surface delamination in the SC-4 panels, as indicted in Figure 59. The use of Kevlar stitching reduced the delamination diameter in both the vinyl-ester and SC-4 systems. Stitching was slightly more effective with the 18-oz SC-4 epoxy system, reducing damage diameter on average by 24% as compared to an 18% reduction in the vinyl-ester systems. However, the absolute damage size in both stitched systems varied by only 2%.
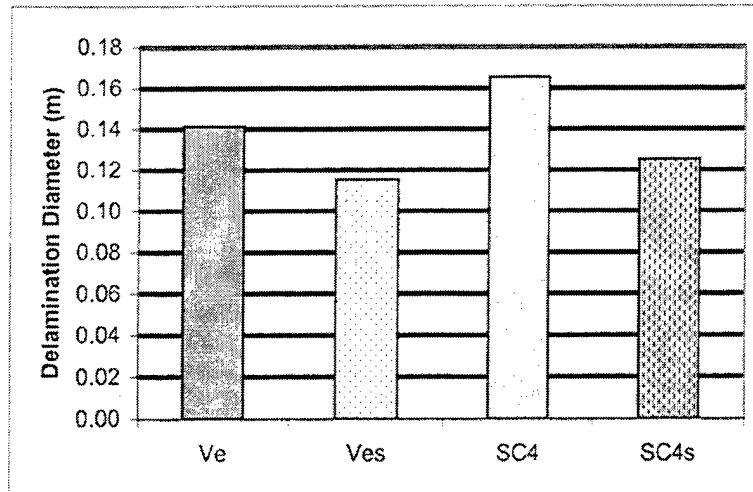
Figure 63. Delamination Size Comparison for Nontiled, 18-oz S-2 Glass/Resin Systems.
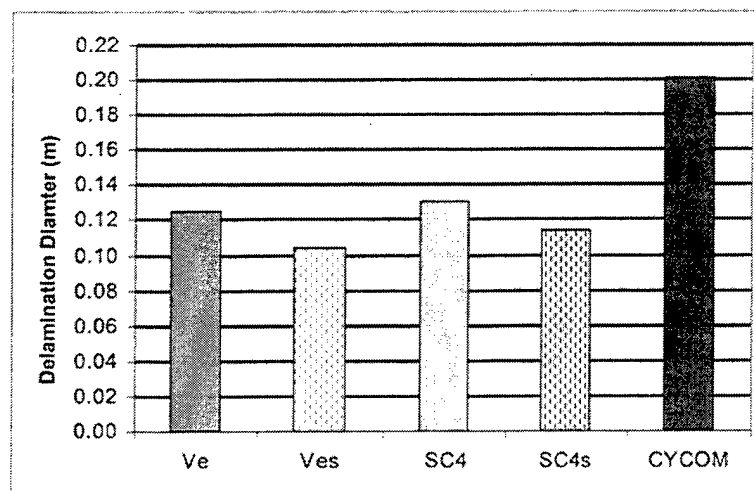
Figure 64. Delamination Size Comparison for Nontiled, 24-oz S-2 Glass/Resin Systems.

Figure 64 shows the size comparison for the 24-oz systems, including the polyester CYCOM 4102. The CYCOM 4102-polyester panels exhibited the most extensive amount of damage and delamination. In many instances, the backside of the CYCOM panels was delaminated all the way to the panel edge. Average damage diameters for the vinyl-ester and SC-4 resins were virtually the same, with the SC-4 panels exhibiting only slightly higher damage diameters.

96

0.24
0.22
0.20
0.18
0.16
0.14
0.12
0.10
0.08
0.06
0.04
0.02
0.00

Delamination Diameter (m)

Vet   Ves-t   SC4t   SC4s-t   CYCOMt
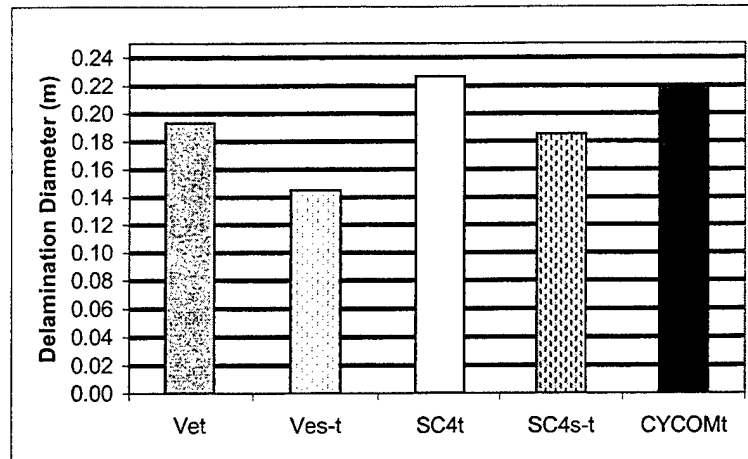
Figure 65. Delamination Size Comparison for Tiled, 18-oz S-2 Glass/Resin Systems and the 24-oz S-2 Glass/CYCOM Polyester.

On average, the 24-oz systems exhibit smaller delaminations than the 18-oz systems. Average delamination diameters were 9–25% less than that of the 18-oz systems. The reduction is particularly noteworthy for the SC-4 epoxy systems, where the use of 24-oz glass led to an over 25% reduction in average delamination diameter. In the 18-oz systems, the damage sizes tended to be the same for the vinyl-ester systems when compared to the SC-4 epoxy except near the back face, where the SC-4 panels delaminated significantly. In both the 24-oz and 18-oz systems, stitching has shown potential in reducing damage size.

Figure 65 shows the tabulated results for the 18-oz tiled panels and the 24-oz-tiled CYCOM panels. The tiled vinyl-ester systems contained, on average, delamination diameters 28–34% greater than the panels without tiles due to the higher impact velocity and larger projectile used. The tiled SC-4 epoxy systems contained delaminations as much as 40–46% greater. As before, the CYCOM panels showed extensive delaminations. The reduction in delamination size with the use of stitching is consistent with the other systems.

Figures 63–65 demonstrate the effectiveness of stitching on reducing damage size. In addition, relatively inexpensive resin systems such as the vinyl ester demonstrate equivalent or slightly smaller damage areas when compared to epoxy resin systems such as SC-4 and pre-impregnated systems such as the CYCOM panels. The reduction in damage size associated

with the use of stitching may also lead to greater stiffness loss in the damaged region, since more energy is being absorbed over a smaller area. The extent of fiber damage in the damaged region may play a significant role in the effectiveness of stitching to improve residual strength. As seen in section 3, stitching is most effective in improving residual strength when the dominant failure mode is delamination growth. In the following section, the CABI modes of failure and the extent of fiber damage in the stitched and non-stitched specimens will be examined.

4.4 CABI. After ballistic impact and damage determination, the panels were tested to determine residual strength. For the 24-oz S-2 glass/vinyl-ester systems the modes of failure were also determined using analytical and finite element analysis. The effect of stitching on compression strength is quantified and comparisons were made between the different composite systems. The effect of damage size on residual strength is also considered.

To use the analytical model for strength predictions and to determine the CABI modes of failure in the 24-oz S-2 glass/vinyl-ester systems, baseline strength and material properties were needed. Strength and modulus data were also collected for the 24-oz S-2 glass/SC-4 epoxy systems. Due to material limitations, it was not possible to determine the baseline properties for the 18-oz S-2 glass systems or the CYCOM systems.

4.4.1 Baseline Strength. Baseline compression strength was determined using American Society for Testing and Materials (ASTM) standard, designation D3410M-95 (ASTM 1995a). A brief description will be given here. For further details refer to the ASTM standards.

With this test procedure, in-plane compression strength is measured by introducing a compression load through shear at wedge grip interfaces (ASTM D3410M-95). The specimen, a flat strip of material with constant rectangular cross section (Figure 66), is inserted into a special fixture.

The "ITRII fixture," as it is commonly known (Figure 67), is then placed within the platens of the Instron machine and loaded in compression. The fixture consists of two rectangular
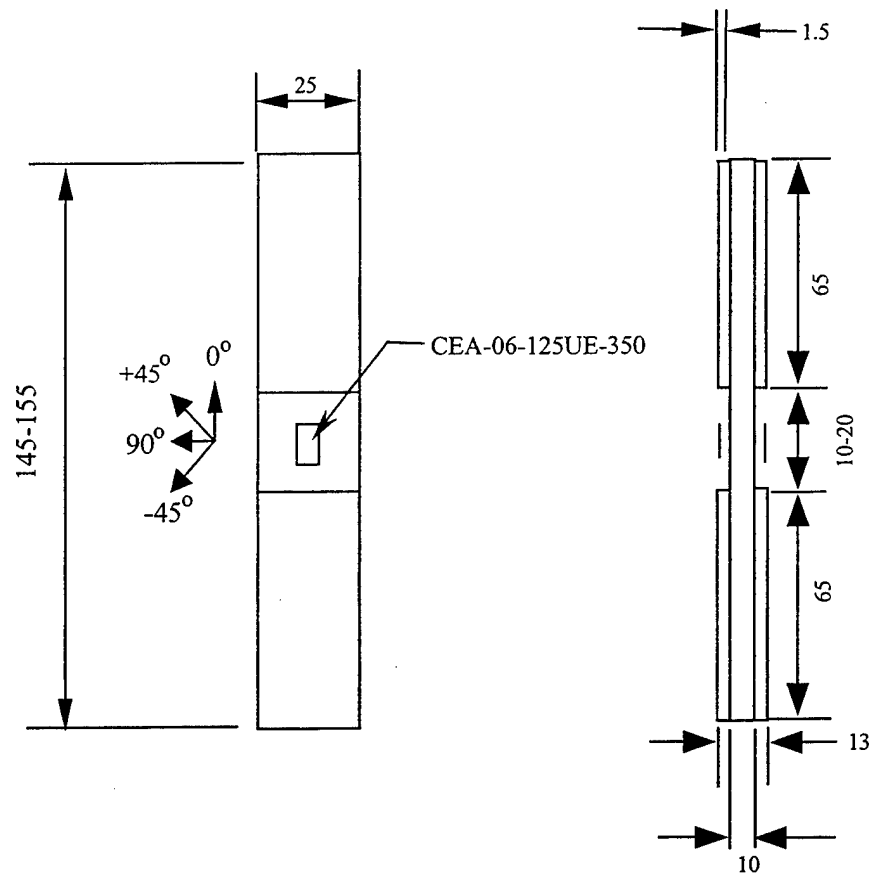
Figure 66. Baseline Compression Test Specimen. Dimensions Are in Millimeters.

wedges. Each set of wedges fits into a mating set of wedges that comprise the upper and lower housing blocks. The upper housing block is attached to the upper crosshead of the test machine while the lower block rests on the lower platen. The specimen is aligned and placed within the two inner wedges. The inner wedges can be adjusted with clamping screws to accommodate specimens of varying thickness.

Ultimate compressive strength is determined from the maximum load carried prior to failure divided by the specimen cross-sectional area. In order to avoid premature failure in the end grips and to have proper load introduction into the specimen, E-glass polymer matrix tabs are bonded to the specimen (Figure 66). Strain gauges were also bonded to both sides of the sample to
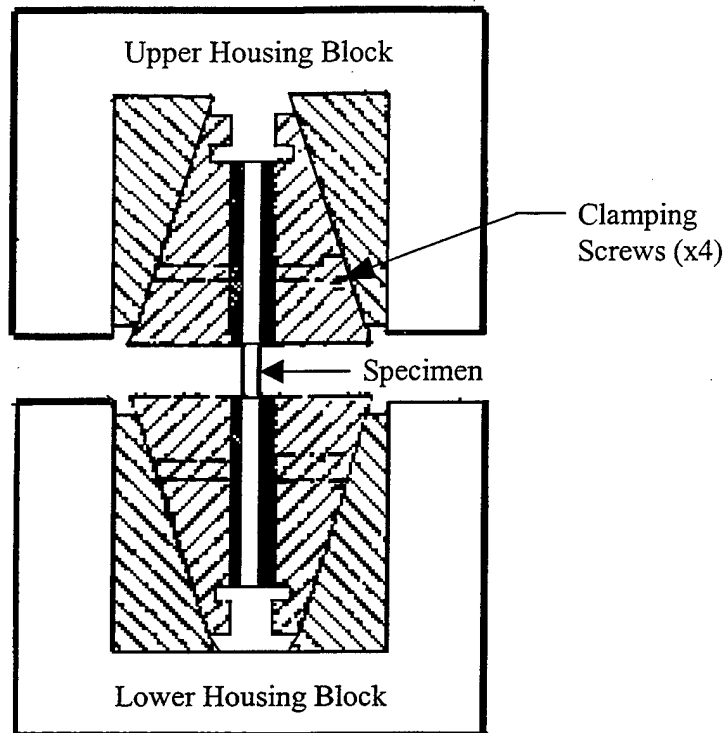
Figure 67. ITRII Test Fixture (or Test Fixture B in ASTM Standard).

measure compressive modulus. Results for the compressive modulus are shown in section 4.5 and compression strength results are shown in Table 16. The table shows that the baseline strength of the vinyl-ester and SC-4 panels are within one standard deviation of each other.

Table 16. Baseline Compression Strength for 24-oz S-2 Glass Systems

Vinyl-Ester Specimen ID	Strength (MPa [ksi])		SC-4 Specimen ID	Strength (MPa [ksi])	
VE_It1	(385.7)	[55.9]	SC-4_It1	(420.2)	[60.9]
VE_It2	(404.0)	[58.6]	SC-4_It2	(441.8)	[64.1]
VE_It3	(409.8)	[59.4]	SC-4_It3	(434.1)	[63.0]
VE_It5	(360.0)	[52.2]	SC-4_It4	(404.6)	[58.7]
VE_It7	(360.4)	[52.3]	SC-4_It5	(424.2)	[61.5]
Average	(384.0)	[55.7]	Average	(416.7)	[60.4]
Standard Deviation	(23.46)	[3.4]	Standard Deviation	(13.5)	[3.5]

4.4.2 Residual Strength.

4.4.2.1 Fixture Assembly. In order to determine the residual compressive strength of the shot panels, a large-scale compression fixture was designed that could support 12-in × 12-in panels of varying thickness (0.72 in–1.7 in). Details on the fixture assembly are given in section 2. The completed assembly is shown in Figure 68.
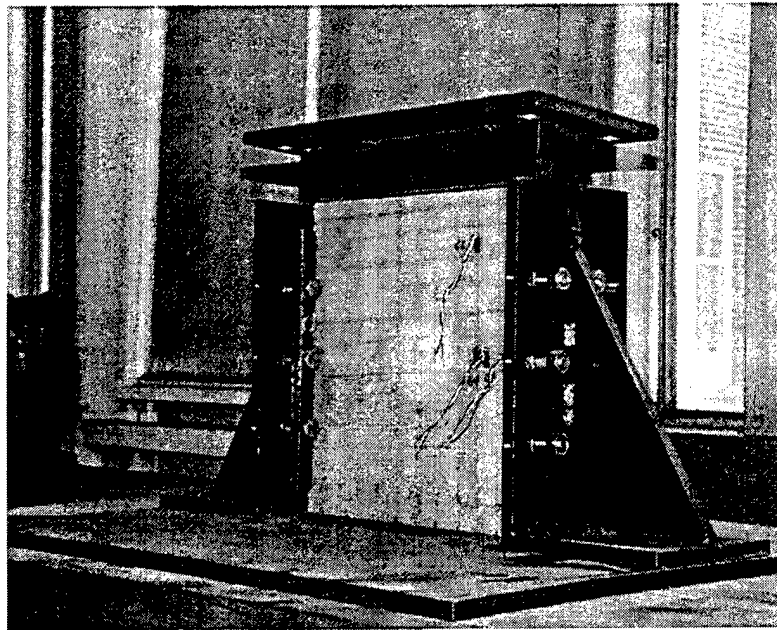
Figure 68. Compression Fixture Assembly With 0.31 m × 0.31 m × 0.02 m (12 in × 12 in × 0.72 in) Panel.

4.4.2.2 Residual Strength Results. The damaged panels were inserted into the compression fixture and tested on the Tinius Olsen compression machine. Compression strength was determined for the various panel systems as load to failure divided by cross-sectional area. Two displacement probes where placed on either side of the panel near the center to measure the extent of global buckling under loading. Strain gauges were also placed on various panels to measure the strain distribution normal to the direction of applied load. This was done in an effort to determine stiffness loss in the damaged region. Results from the strain measurements will be shown in section 4.5.2.

101

The lateral deflection at the center of the impacted specimens was measured as the panels were loaded in compression. A positive value for deflection corresponds to an outward deflection away from the panel centerline for each probe on opposite sides of the panel. Thus, a positive deflection on one side of the panel and a negative deflection on the other would indicate global bending of the panel (Figure 69[a]). A positive reading on both sides of the panel is an indication of delamination buckling (Figure 69[b]). A negative reading of the probe indicates the compression surface, while a positive reading indicates the tension surface (Figure 70).

(a)   (b)
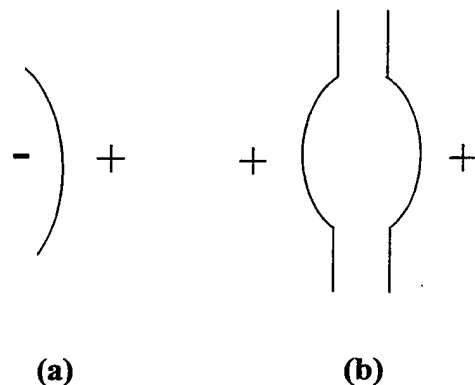
Figure 69. Lateral Deflection at Panel Center Under Compression Loading. Deflections of Opposite Sign Indicate (a) Global Buckling, While Deflections of Same Sign Indicate (b) Delamination Buckling.

Figures 71 and 72 show the lateral deflection at the center of the impact damaged nonstitched and stitched vinyl-ester panels, respectively. The thinner lines represent the deflection of the probe on the front face (projectile entry side), and the thick line represents the back face.

Figure 71 shows that, at small loads, both panel surfaces undergo positive deflections, indicating that delamination buckling is occurring (see Figure 69[b]). At higher loads the front surface deflection reverses direction while the back face continues to deflect positively. From Figure 69(a) there is an indication of global bending. However, the magnitude of global bending is small and is thus assumed not to have significantly affected the compression strength. This is a valid assumption since CABI panels failed across the midsection rather than at the edges as

102

(a)   (b)
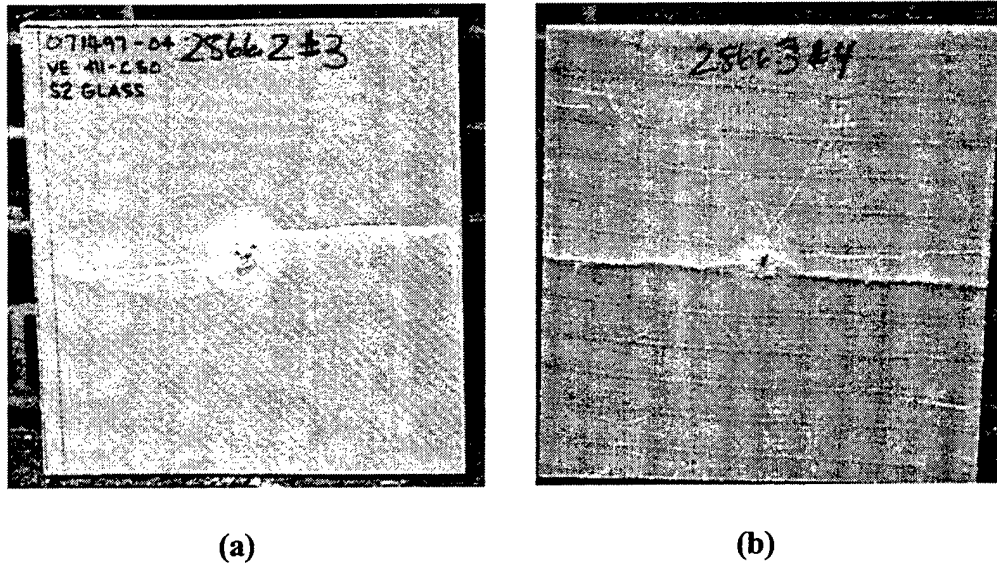
Figure 70. CABI Panels: (a) Nonstitched Vinyl-Ester Panel and (b) Stitched Vinyl-Ester Panel. Failure Occurs Across Panel Midsection.
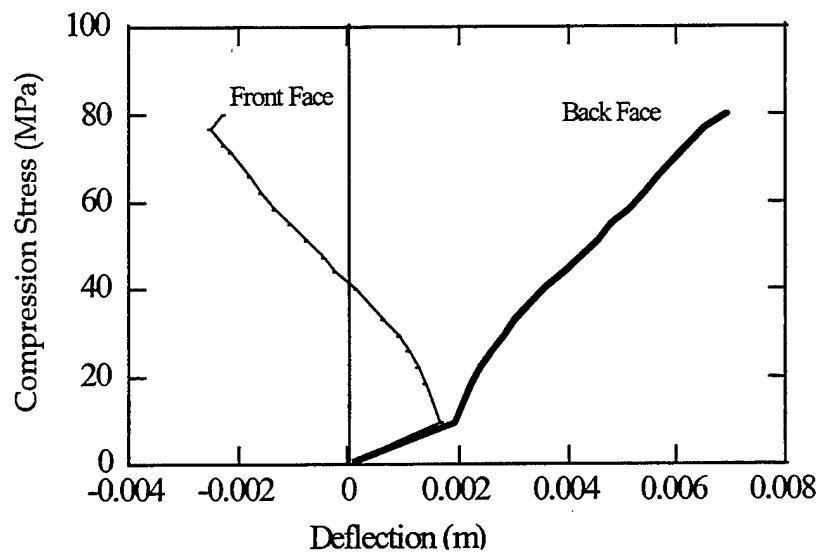
Figure 71. Lateral Deflection for Nonstitched Vinyl-Ester Panels.

would occur had global bending occurred (see Figure 70). Results from the stitched panel follow a similar pattern as that of the non-stitched panel as indicated in Figure 69. Again, deflections were small, indicating minimal bending.

103
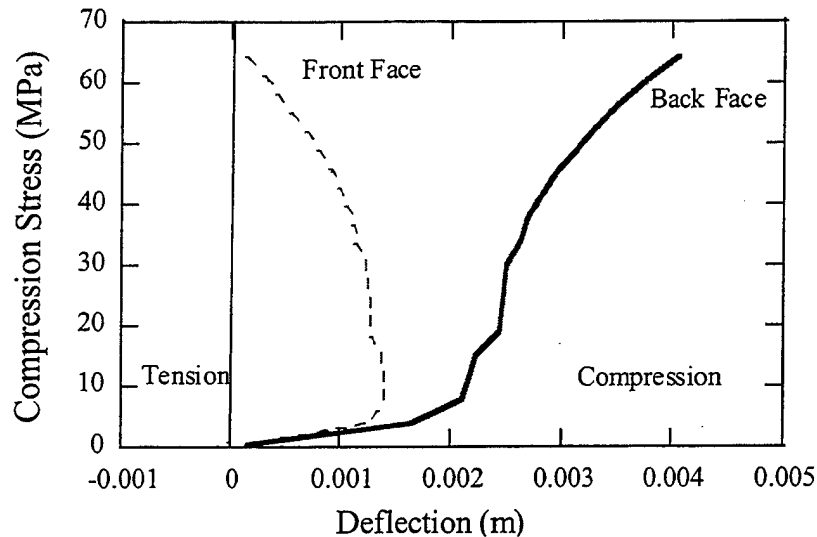
Figure 72. Lateral Deflection for Stitched Vinyl-Ester Panels.

After eliminating failure due to end crushing, and confirming minimal global bending, CABI strength can be accurately determined. As the panels were loaded, acoustic emissions were emitted that correspond to matrix cracking and fiber fracture in the panel. At progressively higher loads, all panels failed catastrophically with sudden load drop. In all cases, failure occurred across the midsection of the panel normal to the direction of applied load, as shown in Figures 70(a) and 70(b).

Four panels each of the 18-oz S-2 glass panels were tested for their residual strength, and five panels each of the 24-oz S-2 glass panels. Tables 17–22 summarize the compression strength results for the nontiled and tiled cases. The bar graphs shown in Figures 73 and 74 compare the effect of stitching and resin type on residual strength for the two different glass preforms. In the 18-oz systems shown in Figure 73, the stitched SC-4 systems showed the highest residual strength. Despite the large back-surface delaminations in the SC-4 panels, their overall strength was 6% greater than that of the vinyl-ester systems. The stitched SC-4 strength was 6% higher than the nonstitched SC-4, while the stitched vinyl ester was 5% higher than the nonstitched vinyl ester. However, these increases are not statistically significant since the standard deviation from the average is between 8–12%.

104

Table 17. Summary of CABI Results for 18-oz S-2 Glass/Vinyl-Ester Systems

Vinyl-Ester Specimen ID	Strength (MPa [ksi])		Vinyl-Ester Stitched Specimen ID	Strength (MPa [ksi])	
VE_1	(100.5)	[14.6]	VEs_1	(98.7)	[14.3]
VE_2	(113.2)	[16.4]	VEs_2	(125.0)	[18.1]
VE_3	(107.6)	[15.6]	VEs_3	(105.1)	[15.2]
VE_4	(109.2)	[15.8]	VEs_4	(123.7)	[17.9]
Average	(107.7)	[15.6]	Average	(113.1)	[16.4]
Standard Deviation	(5.3)	[0.8]	Standard Deviation	(13.2)	[1.9]

Table 18. Summary of CABI Results for 18-oz S-2 Glass/SC-4 Systems

SC-4 Specimen ID	Strength (MPa [ksi])		SC-4 Stitched Specimen ID	Strength (MPa [ksi])	
SC-4_1	(112.3)	[16.3]	SC-4s_1	(118.7)	[14.3]
SC-4_2	(102.1)	[14.8]	SC-4s_2	(121.4)	[18.1]
SC-4_3	(108.8)	[15.8]	SC-4s_3	(125)	[15.2]
SC-4_4	(136.3)	[19.8]	SC-4s_4	—	—
Average	(114.9)	[16.6]	Average	(121.7)	[17.6]
Standard Deviation	(14.9)	[2.2]	Standard Deviation	(3.2)	[0.5]

Table 19. Summary of CABI Results for 24-oz S-2 Glass/Vinyl Ester

Vinyl-Ester Specimen ID	Strength (MPa [ksi])		Vinyl-Ester Stitched Specimen ID	Strength (MPa [ksi])	
VE_5	(137.3)	[19.9]	VEs_5	(138.0)	[20.0]
VE_6	(121.5)	[17.6]	VEs_6	(139.9)	[20.3]
VE_7	(129.6)	[18.8]	VEs_7	(126.7)	[19.4]
VE_8	(118.9)	[17.2]	VEs_8	(139.3)	[20.2]
VE_9	(124.3)	[18.0]	VEs_9	(117.2)	[17.0]
Average	(126.3)	[18.3]	Average	(132.2)	[19.2]
Standard Deviation	(7.3)	[1.1]	Standard Deviation	(10)	[1.4]

Table 20. Summary of CABI Results for 24-oz S-2 Glass/SC-4 Systems and CYCOM System

SC-4 Specimen ID	Strength (MPa [ksi])	SC-4 Stitched Specimen ID	Strength (MPa [ksi])	CYCOM Specimen ID	Strength (MPa [ksi])
SC-4_5	(109.1) [15.8]	SC-4s_4	(144.6) [21.0]	CYCOM_1	(54.6) [7.92]
SC-4_6	(109.4) [15.9]	SC-4s_5	(147.0) [21.3]	CYCOM_2	(44.4) [6.43]
SC-4_7	(97.3) [14.1]	SC-4s_6	(109.8) [15.9]	—	— —
SC-4_8	(102.2) [14.8]	SC-4s_7	(140.2) [20.3]	—	— —
SC-4_9	(111.5) [16.2]	SC-4s_8	(113.4) [16.4]	—	— —
Average	(105.9) [15.3]	Average	(131.0) [19.0]	Average	(49.5) [7.2]
Standard Deviation	(5.9) [0.9]	Standard Deviation	(17.9) [2.6]	Standard Deviation	(7.3) [1.1]

Table 21. Summary of CABI Results for Tiled 18-oz Systems and 24-oz CYCOM Systems

Vinyl-Ester Specimen ID	Strength (MPa [ksi])	SC-4 Specimen ID	Strength (MPa [ksi])	CYCOM Specimen ID	Strength (MPa [ksi])
VEt_1	(80.1) [11.61]	SC-4t_1	(69.5) [10.07]	CYCOM_1	(34.4) [4.99]
VEt_2	(69.7) [10.1]	SC-4t_2	(57.4) [8.32]	CYCOM_2	(34.5) [5.0]
Average	(74.9) [10.9]	Average	(63.4) [9.2]	Average	(34.5) [5.0]
Standard Deviation	(7.4) [1.1]	Standard Deviation	(8.5) [1.2]	Standard Deviation	(0.0) [0.0]

Table 22. Summary of CABI Results for Stitched With Tile 18-oz Systems

Vinyl-Ester Specimen ID	Strength (MPa [ksi])	SC-4 Specimen ID	Strength (MPa [ksi])
VEts_1	(87.0) [12.61]	SC-4ts_1	(103.2) [14.95]
VEts_2	(75.9) [11.0]	SC-4ts_2	(91.3) [13.23]
Average	(81.5) [11.8]	Average	(97.2) [14.1]
Standard Deviation	(7.9) [1.1]	Standard Deviation	(8.4) [1.2]
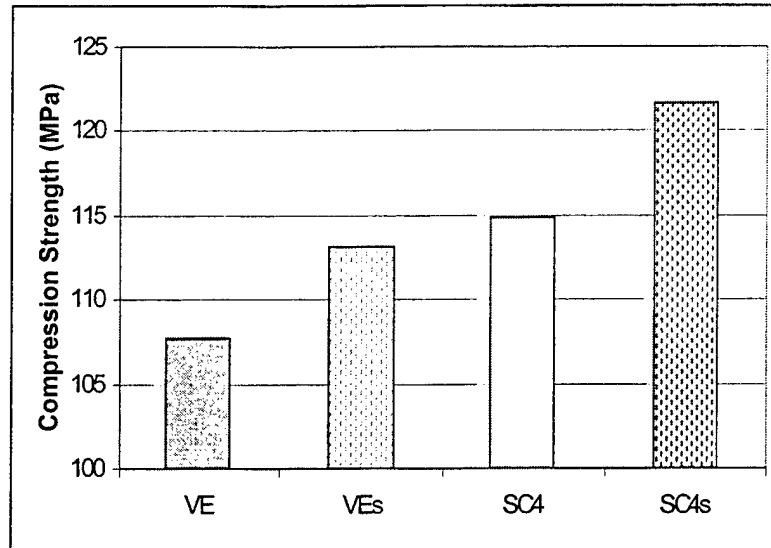
Figure 73. CABI Strength for 18-oz S-2 Glass Panels. Shot With 12.7 mm Projectile at 1,550 ft/s.
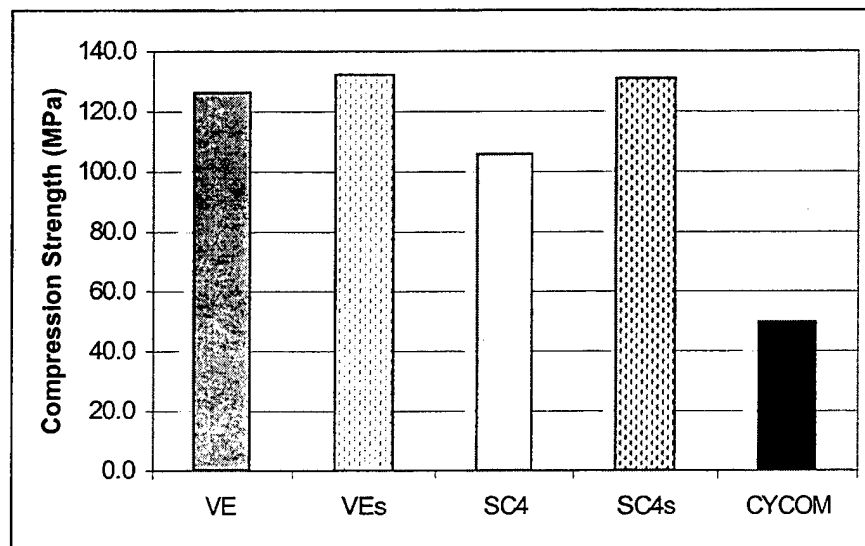
Figure 74. CABI Strength for 24-oz S-2 Glass Panels. Shot With 12.7 mm Projectile at 1,550 ft/s.

In the 24-oz systems (Figure 74), the vinyl-ester and SC-4 panels show little difference in residual strength, although the nonstitched SC-4 was slightly lower. The vinyl-ester panels demonstrated a 13–14% improvement in residual strength when the 24-oz S-2 glass fabric was

used. The CYCOM panels processed by the hand layup method showed the lowest compression strength. All VARTM resins (i.e., vinyl ester and SC-4 epoxy) showed significant improvement (2–3x) in residual strength compared to the original CYCOM material used for armor in the CIFV.

A plot of residual strength vs. average damage diameter is shown in Figure 75 for all the various systems. The systems with the highest residual strength and smallest damage size demonstrate the best multihit performance and damage tolerance. The points within boxes in Figure 75 represent the stitched specimens. In general, the 24-oz stitched systems gave the best results for both criteria, although the improvements are within one standard deviation. All systems tested in this study are far superior to the CYCOM composite armor.
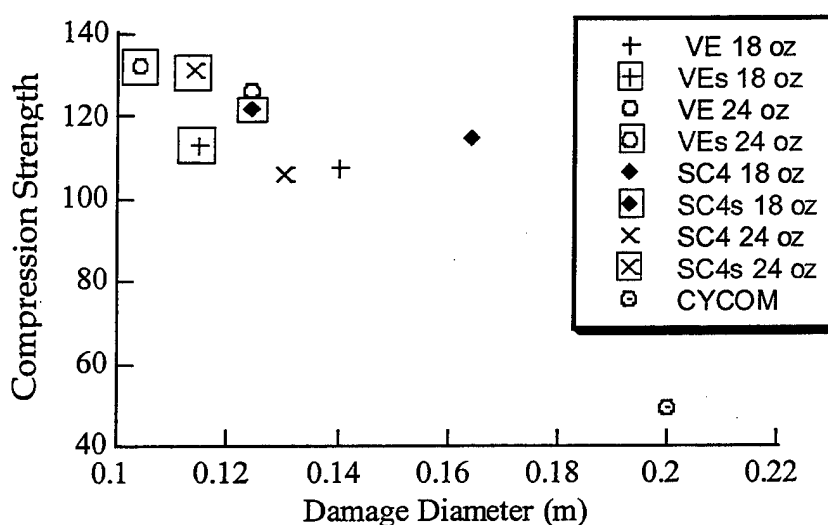
Figure 75. CABI Strength vs. Average Damage Diameter.

Figure 76 shows the tiled case. Tiled panels were made using the 18-oz S-2 glass preform, except for the CYCOM prepreg, which used the 24-oz S-2 glass preform. The vinyl-ester systems exhibited an average residual strength 9% higher than the SC-4 systems, while the stitched SC-4 systems demonstrated a 16% improvement in residual strength over the stitched vinyl-ester systems. The tiled CYCOM panels displayed the lowest residual strength: 54% less than the vinyl-ester systems and 46% less than the SC-4 systems.
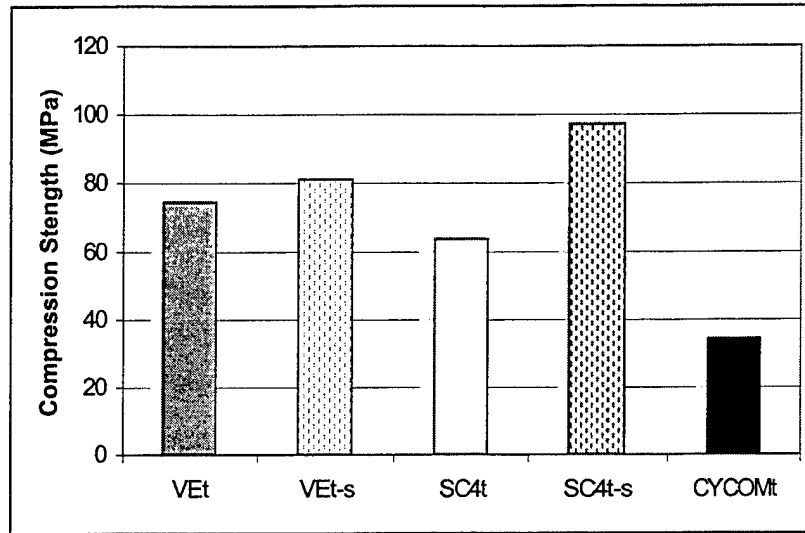
Figure 76. CABI Strength for Tiled, 18-oz S-2 Glass Panels and 24-oz CYCOM Panel. Shot With 20 mm Projectile at 2,700 ft/s.

From the baseline data obtained in section 4.4.1, a normalized plot was generated for the 24-oz systems (Figure 77). No baseline data was generated for the CYCOM prepreg panels. However, it was assumed that their baseline strength is equivalent to that of vinyl-ester systems. This is a reasonable assumption considering the similarities between the two matrix materials, as explained in section 2.
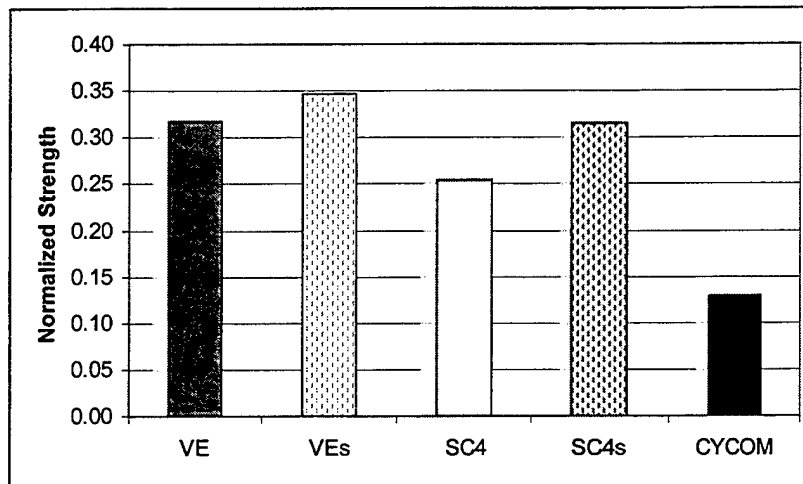
Figure 77. Normalized CABI Strength; 24-oz S-2 Glass Panels Shot With 12.7-mm FSP at 1,550 ft/s.

109

The normalized strength values shown in Figure 77 indicate that panels most likely failed by the in-plane failure mode. In section 3, it was shown that the stress concentration factor, K_T, had a value of 4.1 for notched orthotropic plates of infinite width. Thus, the notched strength of an orthotropic panel is 25% that of an undamaged plate. An examination of Figure 77 shows that the normalized strength also has values ranging between 25–35% of the undamaged strength. In the case of the CYCOM prepreg panels, damage areas were significantly larger (see Figure 64) and therefore, finite width effects may have resulted in higher stress concentrations and consequently, lower strengths; or failure may be due to unstable delamination growth.

Another indication that the governing mode of failure is in-plane, is the lack of significant strength improvement with through-the-thickness stitching. As will be shown in the following section, stitching can improve fracture toughness 10–20 times. If the dominant failure mode was unstable delamination growth, the residual strength would have been significantly higher. In section 4.6, an analysis is performed to evaluate in further detail, the modes of failure in the 24-oz S-2 glass/vinyl-ester systems.

4.5 Modes of Failure for S-2 Glass/Vinyl-Ester Systems. In this section, the two competing mechanisms of failure, in-plane and unstable delamination growth, are examined in light of the experimental data presented herein. A closer examination of the 24-oz S-2 glass/vinyl-ester systems was performed to determine CABI failure mechanisms and the effect of stitching on residual strength and in-plane stiffness. In order to analyze and predict CABI modes of failure using the CSDS methodology and finite element analysis, it was first necessary to determine key input variables. Based on these input variables along with experimental observations noted previously, conclusions could be reached concerning the modes of compression failure. As mentioned in section 3, the analytical model and FEA analysis require delamination size and location, G_{IC}, in-plane stiffness reductions, and strength and material properties. Delamination sizes were determined by use of ultrasonic evaluation (section 4.3), while the compressive strength properties are summarized in Table 16. In this section, compression modulus, fracture toughness, and inclusion stiffness are determined for the 24-oz S-2 glass/vinyl-ester systems.

4.5.1 Material Properties. Material properties used in the analysis are summarized in the following sections.

4.5.1.1 Compression Modulus. The compression modulus for the 24-oz S-2 glass/vinyl ester was determined using the IITRI compression test described in section 4.4.1. Two strain gauges were placed on either side of the specimen and the average modulus was determined. Figure 78 shows the stress-strain plots for the nonstitched and stitched vinyl-ester specimens. Average modulus for the nonstitched systems was approximately 24.0 ± 1.0 GPa, while the stitched specimens averaged 27.2 ± 1.2 GPa. The higher modulus in the stitched specimens is consistent with the higher fiber volume fraction due to the fabric compression from stitching.

4.5.1.2 Mode I Fracture Toughness. The mode I fracture toughness, or G_{IC}, is determined using the DCB test in accordance with ASTM D 5528 (ASTM 1995b). The DCB specimen (Figure 79) is a rectangular specimen (2.45 cm × 22.0 cm) of uniform thickness (0.62 cm). The specimen contains a piece of Teflon film at the midplane to initiate delamination growth. Opening loads are applied to the DCB specimen by means of blocks that are adhesively bonded at the edge of the specimen. As load is applied the delamination lengthens. By measuring the flexural energy input into the beam as a function of crack growth, a value of G_{IC} is determined. If linear elastic behavior is assumed, the fracture toughness is

$$G_{IC} = \frac{P^2}{2W} \frac{dC}{da},$$ (33)

where P is the applied load at the onset of crack growth, W is the width of the specimen, a the initial crack length, and C the compliance. The compliance, C, was determined experimentally using the Berry method (Berry 1963). Compliance gives the relationship between load, P, and displacement, v (Broek 1986):

$$C = \frac{v}{P}.$$ (34)

111
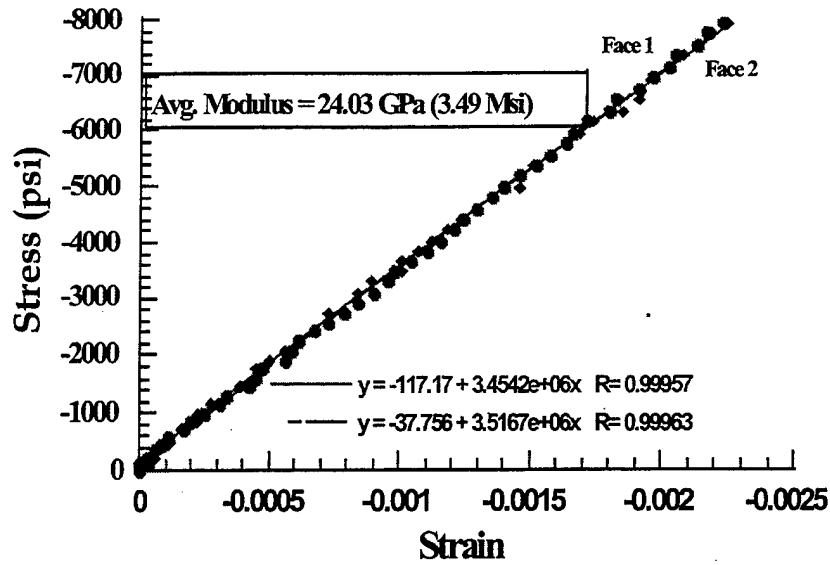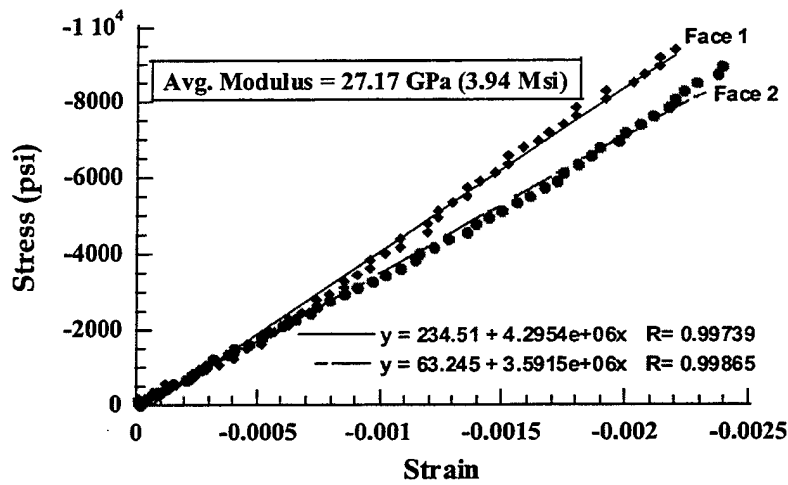
Figure 78. Typical Stress vs. Strain Curve for (a) Nonstitched S-2 Glass/Vinyl-Ester Systems and (b) Stitched S-2 Glass/Vinyl-Ester Systems.

Experimentally, the compliance takes into account the effects of specimen thickness, crack length, and the moduli of the cantilever beam. According to Berry, the curve for compliance is given by

112
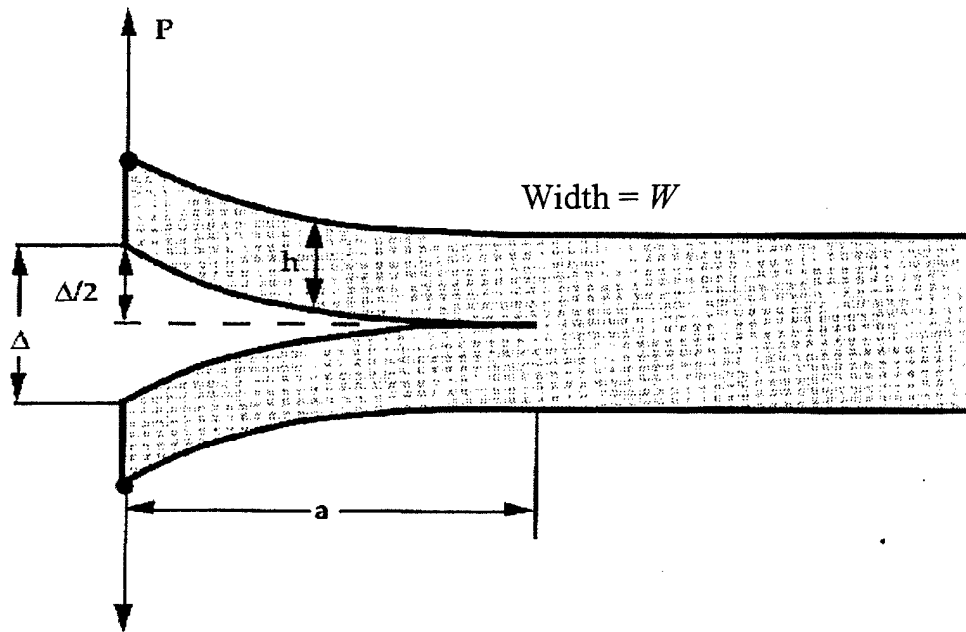
Figure 79. DCB Specimen.

$$C = Ka^n, \qquad (35)$$

where a is the crack length and K and n are unknown constants. Taking the log of equation 35:

$$LogC = LogK + nLoga. \qquad (36)$$

Thus, n is the slope of the log-log plot of equation 36. The fracture toughness is now given by:

$$G_{Ic} = \frac{nP_{cr}v_{cr}}{2Wa}, \qquad (37)$$

where P_{cr} is the critical load and v_{cr} is the critical displacement.

Fracture toughness results are shown in Figures 80 and 81 for nonstitched and stitched vinyl-ester systems, respectively. The crosshead speed was set at 0.2 in/min, in order to produce

113
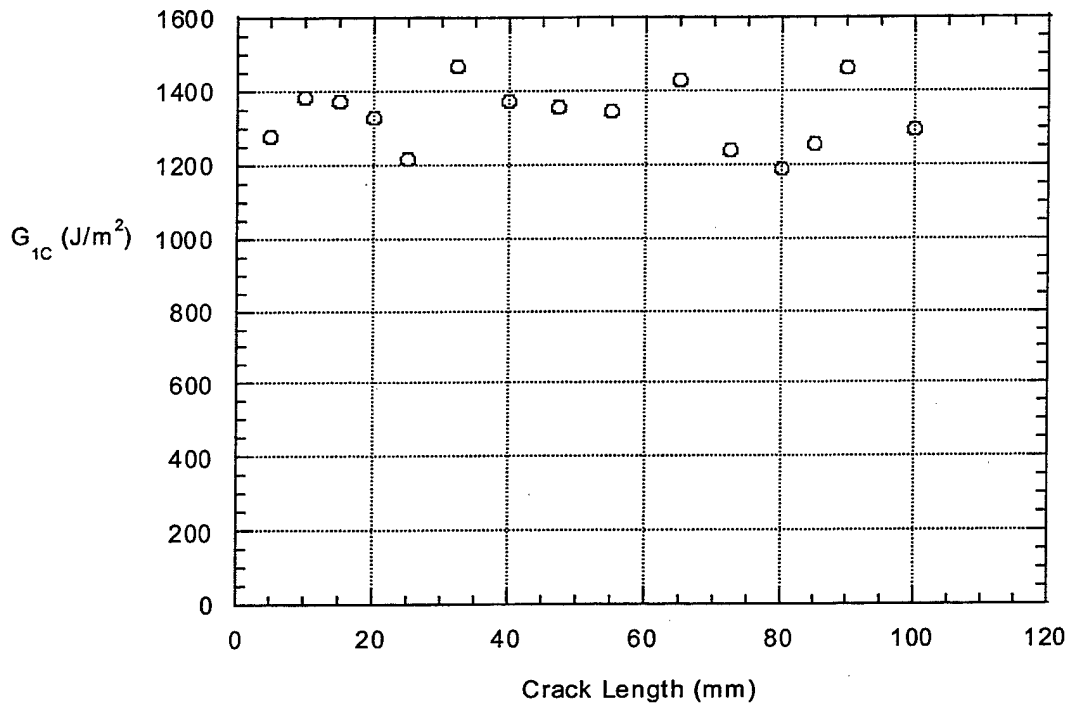
Figure 80. **Typical DCB Fracture Toughness Curve for Nonstitched 24-oz S-2 Glass/Vinyl-Ester Systems.**

static loading. For the nonstitched specimens, G_{IC} values ranged between 1,200 and 1,550 J/m^2. The average G_{IC} is 1,250 ± 101 J/m^2.

Stitched systems showed a significant increase in fracture toughness, between 6 and 10 times over the nonstitched systems (Figure 80). Unlike the nonstitched DCB specimens, the crack grows unstably in the stitched DCB specimens. The sequence of crack growth is shown in Figure 82. Initially, the crack grows steadily until it passes the first stitch row (Figure 82[a]). The stitch in the crack wake is extended until the crack tip is approximately 9 mm beyond the first stitch row, labeled a_1 (stitches are spaced, approximately 25.4 mm apart). At this point, the first stitch breaks and is pulled out. The stored elastic energy in the cantilever beam is released and the crack jumps approximately 2 mm beyond the second stitch row, labeled a_2. The process continues in this manner with the crack advancing unstably.
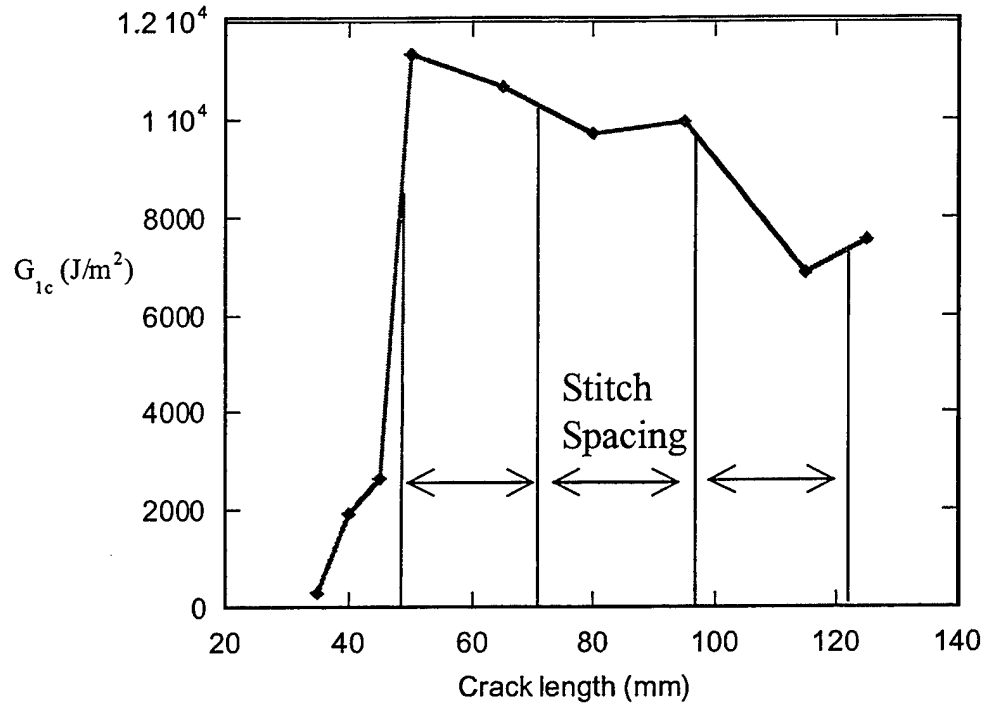
Figure 81. DCB Fracture Toughness Curve; Stitched Systems.

(a)   (b)
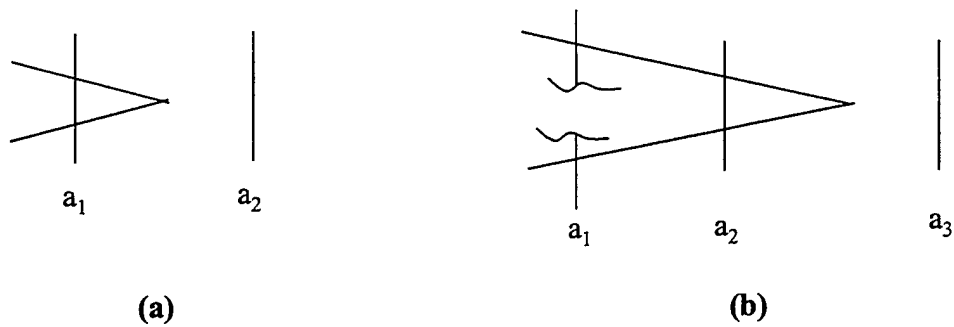
Figure 82. Schematic of Crack Progression in Stitched DCB (a) Before Stitch Breaks and (b) After Stitch Breaks.

The average G_{IC} for the stitched specimens was 8000 J/m^2 ± 2000 J/m^2. The stitch spacing is indicated on the figure. The drop in G_{IC} values at larger crack lengths (Figure 81) is due to stitches breaking in the crack wake.

4.5.2 Determining Inclusion Stiffness. Stitching has shown effectiveness in reducing damage size and improving multi-impact performance. However, it is unclear whether this

115

improvement comes at the sacrifice of in-plane properties such as stiffness and strength. In an undamaged panel, stitching is known to reduce stiffness, strength, and fatigue life, simultaneously significantly improving interlaminar properties. During ballistic impact, stitching reduces damage size; therefore increasing CABI strength provided that failure is dominated by unstable delamination growth. However, stitching may reduce inclusion stiffness properties since projectile energy is absorbed as the stitches break and pull out from the impact event. This results in high stress concentrations adjacent to the inclusion that may lead to in-plane failure. Thus, a trade off exists, and methodology must be developed to optimize stitch spacing to reduce damage size and determine the inclusion stiffness needed.

The in-plane stiffness loss in the damaged region due to fiber breakage upon ballistic impact was measured for two vinyl-ester laminates and two stitched laminates. To determine the in-plane stiffness reduction of the damaged region, three strain gauges where placed along the centerline of the panel normal to the direction of applied load, and one strain gauge was placed near the top of the panel away from the damaged region. The normalized strain distribution was then plotted and superimposed with FEA runs for various inclusion stiffnesses (Figure 83). The boundary conditions and mesh used in the FEA is shown in section 3.2.

Each curve in the plot shown in Figure 83(b) represents a different in-plane stiffness knockdown from the undamaged parent laminate. Thus, for example, the curve labeled 0.50*E represents a 50% reduction in the in-plane stiffness matrix from the undamaged state. Superposition of the averaged experimental data shows that the vinyl-ester panels suffered an 80 ± 5% loss in stiffness. The stiffness losses for both stitched and nonstitched specimens were within one standard deviation of each other.

It should be noted that determining the distance from the edge of the damaged region is somewhat arbitrary, since the size of the damaged region varies through the thickness. In these experiments, the hole edge was taken from the largest delamination at the back face.

116

Ny

X-R (m)

(a)   (b)
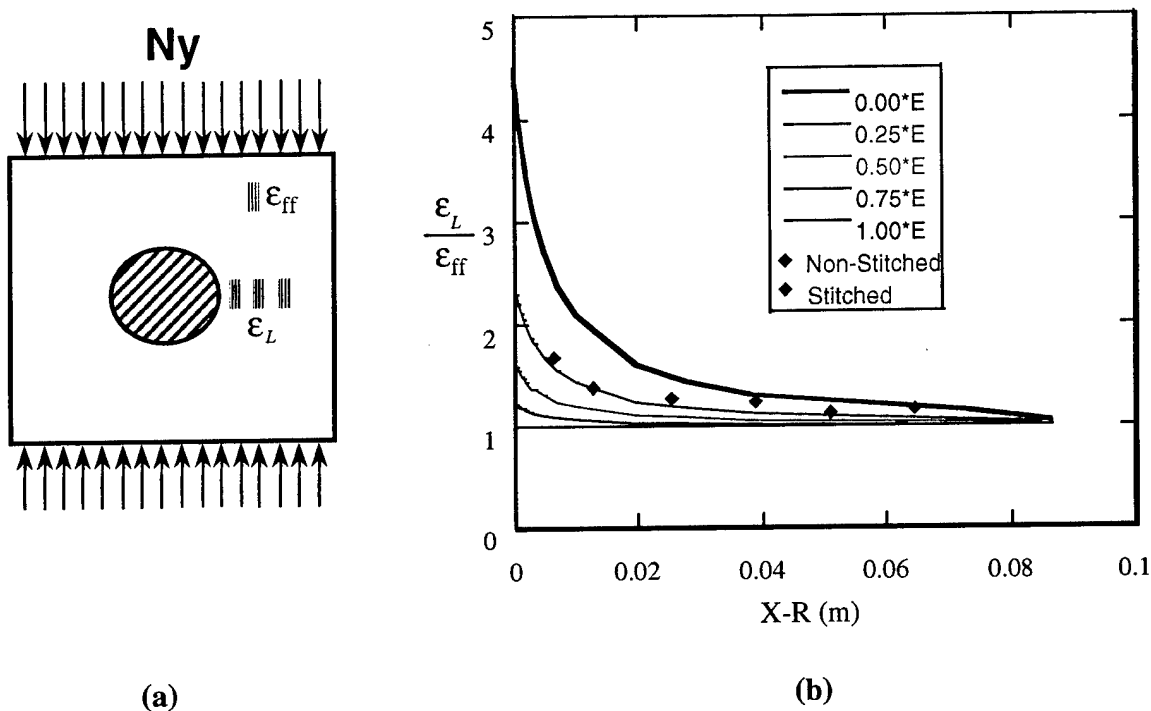
Figure 83. **Experimental Setup for Determining Strain Distribution: (a) Three Strain Gauges Are Placed Along Panel Centerline Normal to Direction of Applied Load, and One Gauge Is Placed Far From the Damaged Region; (b) FEA Plot of Normalized Strain Distribution for Various Inclusion Stiffnesses With Experimental Data Superimposed.**

It is unclear from these preliminary investigations as to whether stitching has an adverse effect on in-plane stiffness of the inclusion when compared to the nonstitched panels. Stiffness losses in the nonstitched panels are so severe that it does not allow for a statistically significant comparison to the stitched panels. Therefore, further experiments are necessary to determine conclusively, the effects of various stitch parameters on postimpact stiffness loss of the inclusion.

4.6 Theoretical vs. Experimental Correlation. The data obtained in this experimental study provides the baseline properties, fracture toughness, damage size, and inclusion stiffnesses for the vinyl-ester systems required to predict failure modes and residual strength. Figures 84 and 85 show plots of residual compression strength vs. damage size based on model predictions superimposed with experimental data for both non-stitched and stitched vinyl-ester systems, respectively. The relatively flat lines represent membrane failure for various stiffness reductions

117
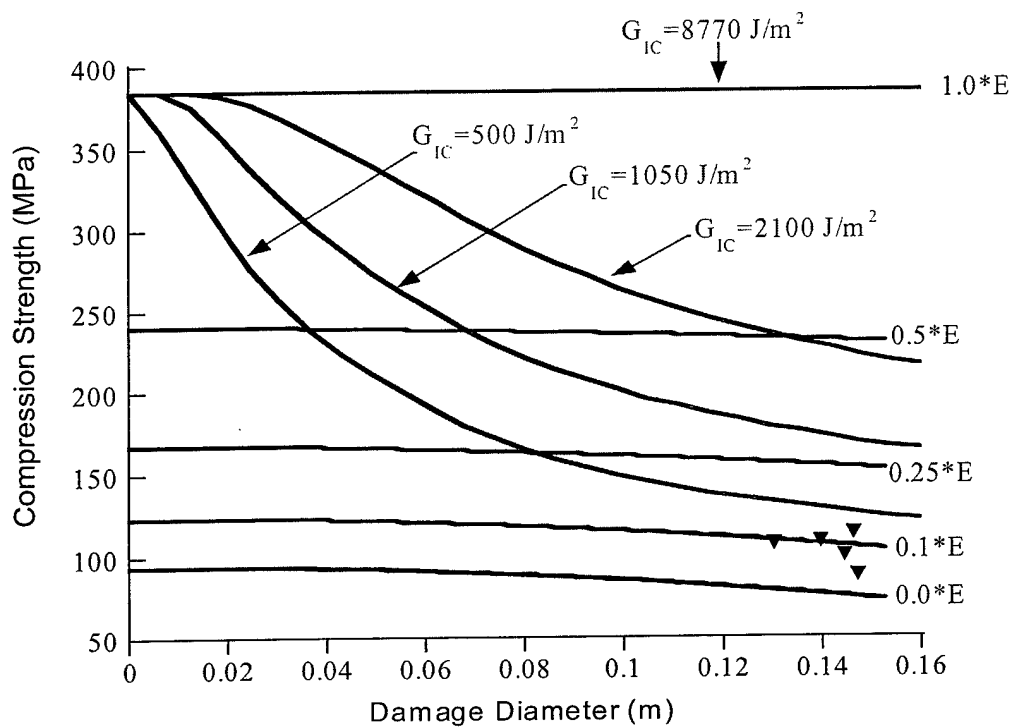
Figure 84. Analytical Predictions and Experimental Results for Nonstitched Vinyl-Ester Systems.

in the damaged region. For example, the curve represented by 0.10*E in the figures, indicates that the in-plane stiffness in the inclusion is only 10% of the parent laminate's stiffness. The steeply curved lines represent failure due to delamination growth and each curve represents a different fracture toughness.

From the experimental data, it was found that the nonstitched vinyl-ester specimens had an inclusion stiffness between 0.15 × E and 0.25 × E, and an average G_{IC} of 1,250 ± 101 J/m^2. Using these values in the analysis and comparing with the experimental compression strength data, Figure 84 shows that the dominant failure mode is most likely in-plane failure. The inclusion stiffness in the stitched vinyl ester-systems was the same as that of the nonstitched systems, although the fracture toughness was significantly higher (8,000 J/m^2 ± 2,000 J/m^2). The higher fracture toughness values in the stitched specimens lead to smaller damage sizes, yet no improvement in residual strength was seen. The analytical predictions shown in Figure 85

118
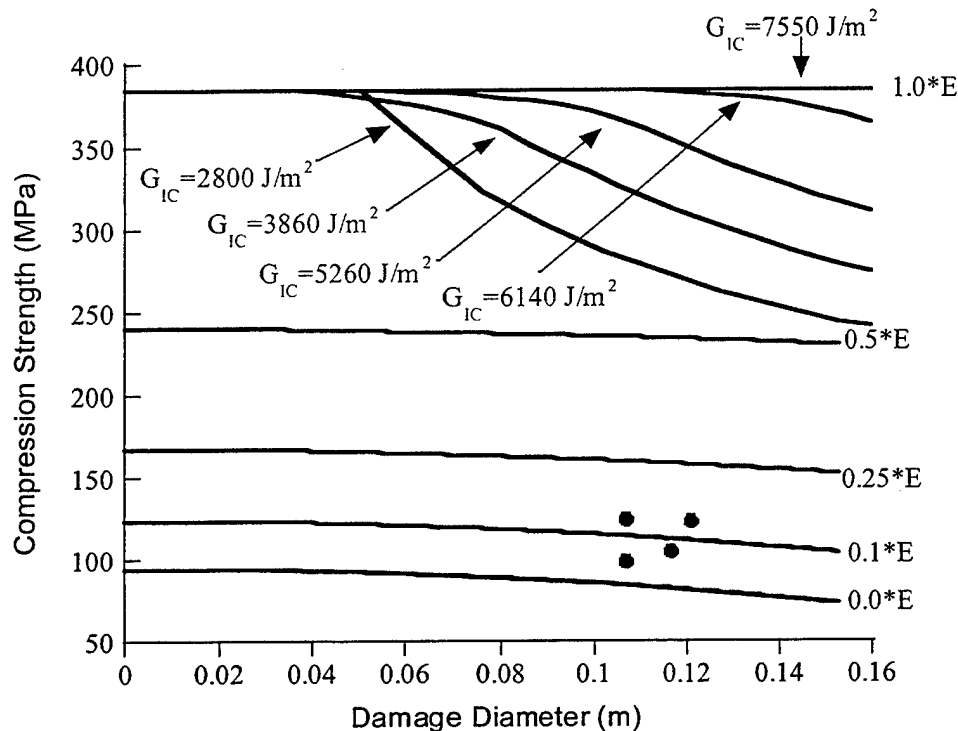
Figure 85. **Analytical Predictions and Experimental Results for Stitched Vinyl-Ester Systems.**

show that the lack of improvement in residual strength, despite higher fracture toughnesses, is due to the failure mode being in-plane.

Figures 84 and 85 and experimental observations indicate that the dominant failure mode is membrane failure. As the panels were compressively loaded, both the stitched and nonstitched panels exhibited slight amounts of delamination buckling at low loads (Figures 71 and 72). As the load progressed higher, acoustic emissions were emitted that correspond to matrix cracking and fiber fracture. Ultimate failure typically occurred with a catastrophically loud noise, typical of membrane failure due to local stress concentrations. In addition, all the panels failed across the midsection, the regions of highest stress concentration in an orthotropic layup.

Examination of the various resin systems indicates that the low-cost vinyl-ester systems achieved superior ballistic performance and multihit capability with the typically more expensive SC-4 epoxy systems (Figures 59–61, 73, and 74). Both systems outperformed the CYCOM

prepreg panels. The use of through-the-thickness stitching reduced damage diameter 18–24% in both the vinyl ester systems and SC-4 epoxy systems compared to the non-stitched baseline.

Comparing residual strength, it can be seen that statistically significant differences do not exist between the vinyl-ester and SC-4 epoxy laminates. The CYCOM panels exhibited CABI strengths 50% lower than that of either the vinyl ester or SC-4 systems. Both the SC-4 and vinyl-ester panels were manufactured using SCRIMP, while the CYCOM panels were manufactured by hand layup and consolidated under vacuum pressure. Tables 11–13 show that the void content is significantly larger for the CYCOM panels when compared to the vinyl-ester and SC-4 epoxy systems. Previous work has shown that for an increase in void content from 1% to 4% may cause a 50% reduction in compression strain to failure (Olson et al. 1995). This seems to suggest that the SCRIMP process yields higher quality parts, and consequently, superior mechanical properties compared to hand layup.

Stitching has been shown to reduce ballistic damage by introducing new energy-absorbing mechanisms related to stitch fracture and pullout. However, the precise effects of stitch density on ballistic performance are not well understood and further investigations are still needed. The failure mode analysis has shown that increasing fracture toughness through stitching improves CABI strength, provided that stiffness reductions in the inclusion are not severe. Yet stitching may cause severe reductions in inclusion stiffness as projectile energy is absorbed through the fiber breakage and pullout mechanisms. Thus, an optimum stitch density must be achieved to maximize both multi-impact performance and CABI strength. A parametric study is conducted in the following section to examine the effect of inclusion stiffness and fracture toughness on damage size and residual strength. From this analysis, recommendations will be made in order to optimize multihit ballistic performance and CABI strength based on design requirements.

5. Parametric Study

5.1 Introduction. From the experimental study, it was found that improving fracture toughness by through-the-thickness stitching results in a reduction in damage size. However, while stitching improves multi-impact performance it may also lead to an increase in fiber

120

damage, causing the failure mode to shift from delamination growth to membrane failure. Thus a design trade-off exists between maximum fracture toughness and damage-induced in-plane stiffness reduction.

The degree of stiffness loss in the damaged region depends on the nature of the ballistic impact and the response of the material to high-amplitude, high-strain-rate loadings. Currently, it is not possible to analytically predict the extent of damage that will occur in a ballistically impacted panel. This information must be obtained experimentally, as was shown in section 4.

In this section, the effects of inclusion stiffness and fracture toughness on residual strength and multi-impact performance are examined. From this study, recommendations will be made in order to optimize multihit ballistic performance and residual strength based on design requirements.

5.2 Effect of Fracture Toughness and In-Plane Stiffness on Residual Strength. In section 3, a case study was presented in which failure occurred due to instability-related delamination growth. From this failure mode it was recommended that multi-impact performance and residual strength could be improved by increasing G_{IC}, through the use of through-the-thickness stitching. Figure 86 shows the plot generated in section 3 for the S-2 glass/polyester CYCOM prepreg. The horizontal lines represent membrane failure for various inclusion stiffnesses, while the curves represent failure by delamination growth. The critical failure mode corresponds to the lowest predicted compression strength at a given damage size. For example, delamination sizes less than 0.1 m and inclusion stiffnesses less than 0.4 × E fail due to membrane stress concentration. For large delamination sizes, materials exhibiting low fracture toughness will fail due to instability related delamination growth (e.g., consider G_{IC} = 100 J/m^2 and 0.4 × E). In this regime, improvements in G_{IC} can lead to increases in CABI up to the level where the failure mode transitions back to membrane stress concentration that is governed by inclusion stiffness.

To further illustrate this interaction, consider Figure 87 where a typical plot of CABI strength vs. damage size is shown for two different panels, both damaged in the same manner. One
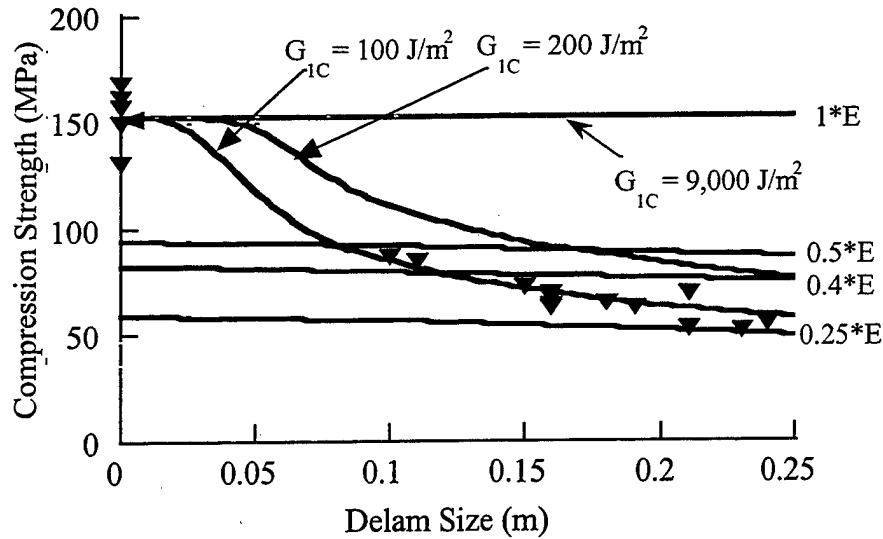
Figure 86. Model Predictions for Strength vs. Damage Diameter for S-2 Glass/Polyester CYCOM Prepreg. Points Represent Experimental Results.
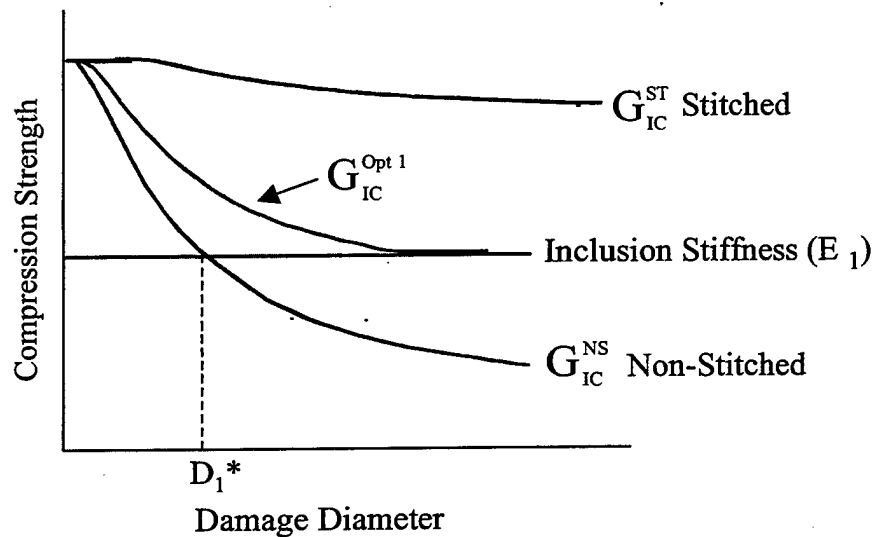
Figure 87. Typical Plot of CABI Strength vs. Damage Size for Two Laminates. One Laminate Is Stitched Through-Thickness, and the Other Is Nonstitched. Both Laminates Have Identical Inclusion Stiffnesses.

laminate is stitched through the thickness and the other is unstitched. Otherwise, the material properties and layup are identical. The stitched laminate is taken to have a much higher G_{IC}^{ST} than the unstitched laminate (i.e., G_{IC}^{NS}). The in-plane stiffness of the damaged region is taken to

be the same in both cases. From Figure 87, it can be seen that if the damage size is $D < D_1^*$, failure will occur in the in-plane mode before unstable delamination growth can occur. This is true for both the stitched and nonstitched laminates. If the damage size is $D > D_1^*$, then failure will occur in the nonstitched panel by instability-related delamination growth and by membrane failure in the stitched laminate. Thus in either case, the highest residual strength that can be achieved is governed by the stress concentration factor uniquely defined by the in-plane stiffness of the inclusion. An optimal $G_{IC}^{Opt\ 1}$ achieved through stitching is shown in Figure 87 where delamination growth asymptotically approaches membrane failure as damage size increases for inclusion stiffness, E_1. Increasing G_{IC} values above this optimal level does not lead to additional improvements in residual strength in this example and would further increase the cost of preforming.

If G_{IC} is held constant (i.e., the nonstitched case, G_{IC}^{NS}) and the in-plane stiffness of the inclusion is varied (as shown in Figure 88) when the inclusion stiffness is E_1, membrane failure will occur when $D < D_1^*$, and delamination growth failure will occur for $D > D_1^*$. If the inclusion stiffness is increased to E_2 as shown in Figure 88, membrane failure will occur at a higher strength when $D < D_2^*$, and delamination growth failure will initiate for $D > D_2^*$. Thus increasing in-plane inclusion stiffness increases the CABI strength and the transition to unstable delamination growth occurs at lower damage sizes. In this case, increasing G_{IC} by stitching will lead to improvements in residual strength as shown in Figure 89. However, increasing G_{IC}^{ST} above the optimum ($G_{IC}^{Opt\ 2}$) will not provide any further improvement in residual strength and the situation of Figure 87 results.

5.3 Multiple Impact Performance and Damage Size. In order to improve multiple impact performance of composite armor, it is necessary to reduce the damage size caused by a ballistic impact. In section 4, through-the-thickness stitching was shown experimentally to be effective. Furthermore, the previous section showed that CABI strength can be improved by stitching by reducing the damage size and increasing G_{IC} up to an optimal level where the transition to the membrane failure occurs. Recall that this transition is governed by the stress concentration and
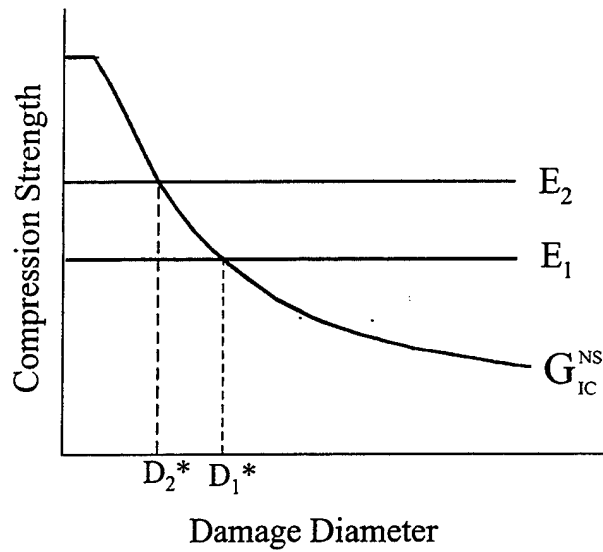
Figure 88. CABI Failure Modes for Varying Inclusion Stiffness Holding G_{IC} Constant.
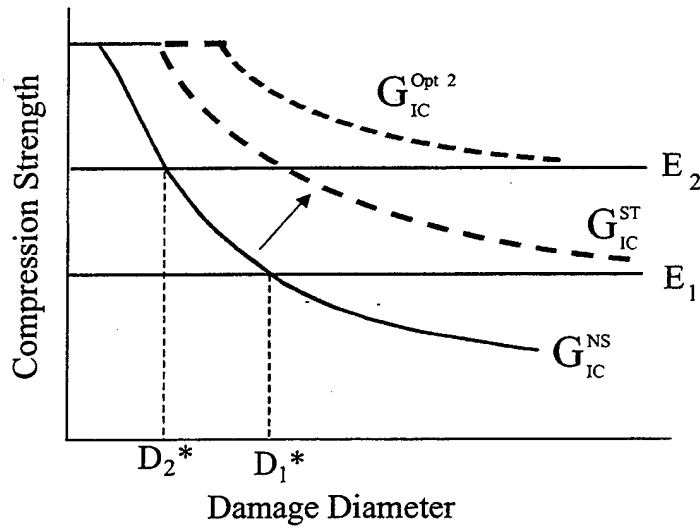
Figure 89.   Increasing the Inclusion Stiffness From E_1 to E_2 Allows for Improvements in Residual Strength to Be Obtained by Increasing G_{IC} for $D > D^*$.

inclusion stiffness (see section 3.2.1.4). One of the assumptions in the previous section was that the inclusion stiffness was independent of damage size.

In the case where ballistic impact damage is constrained to a smaller projected area by stitching, a greater degree of microdamage, such as fiber fracture and pullout and matrix

124

cracking, is expected. Consequently, higher specific energy absorption (i.e., energy/unit volume) will correspond to a higher density of damage and an overall reduction in inclusion stiffness. Based on the previous section, a reduction in inclusion stiffness will establish the upper bound on CABI strength defined as $\dfrac{1}{K_T(E)} X_C$. Recall that the finite-width stress-concentration factor is defined in Figures 41 and 42 in section 3.

To optimize both multiple impact performance and residual strength, the stitching parameters must be carefully designed such that fracture toughness is increased just enough to arrest ballistic damage within the allowable. Recall that in section 3 damage tolerance was defined in terms of the delamination growth failure mode, in which case smaller damage area increased compression strength. However, the potential for membrane failure tends to increase for smaller damage sizes, since the inclusion stiffness is reduced as ballistic energy is contained within a smaller area. In this case, additional increases in G_{IC} may only lead to further reductions in in-plane stiffness, and consequently lower strength.

Consider a material with a nonstitched baseline G_{IC} represented by curve A in Figure 90, and inclusion stiffness E_1. A damage size D^* is defined as the damage size at the intersection of the baseline G_{IC} and the in-plane failure curve. For delamination sizes less than D^*, failure will occur by the in-plane failure mode. As the delamination sizes increase beyond D^*, improvements in the material's fracture toughness will result in improvements in compression strength. Assuming an initial material fracture toughness represented by curve A, the maximum strength improvement, ΔX_A, that can be obtained at D_1, for example, is by increasing G_{IC} to curve B. Any further increases in G_{IC} above curve B will only result in membrane failure. This approach can be applied at all damage sizes so that the designer can determine how much G_{IC} increase is needed. For the more general case, the maximum strength improvement (defined as ΔX_C) at any given damage size above D^* can be found by generating a series of G_{IC} curves and measuring the distance between the baseline fracture toughness represented by curve A, and the intersection of E_1 and the improved G_{IC} curve. Figure 91 shows such a design chart, generated using the CSDS analytical code, for various inclusion stiffnesses. The material and strength properties used in the code were for the 24 oz S-2 glass/vinyl-ester system.
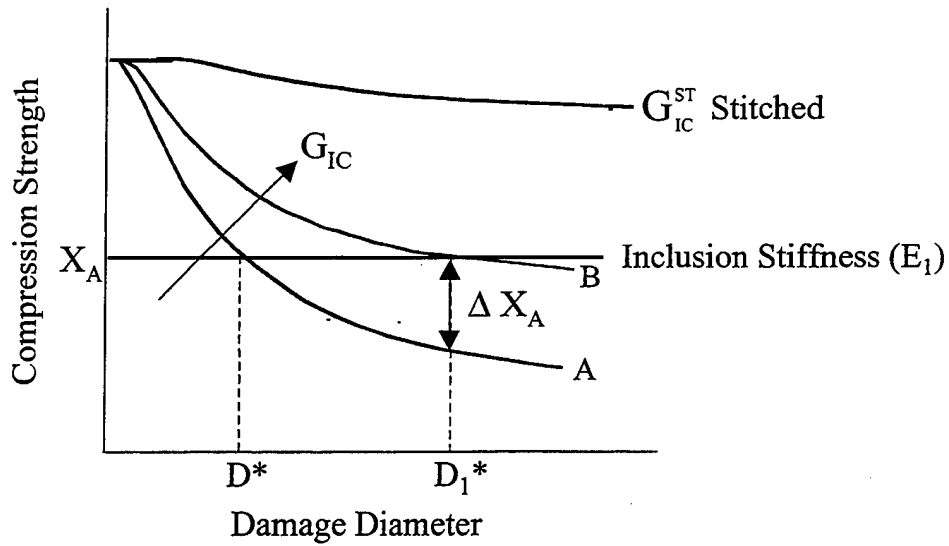
Figure 90. **Maximum Strength Improvement That Can Be Obtained at D_1 by Increasing Fracture Toughness to Curve B.**
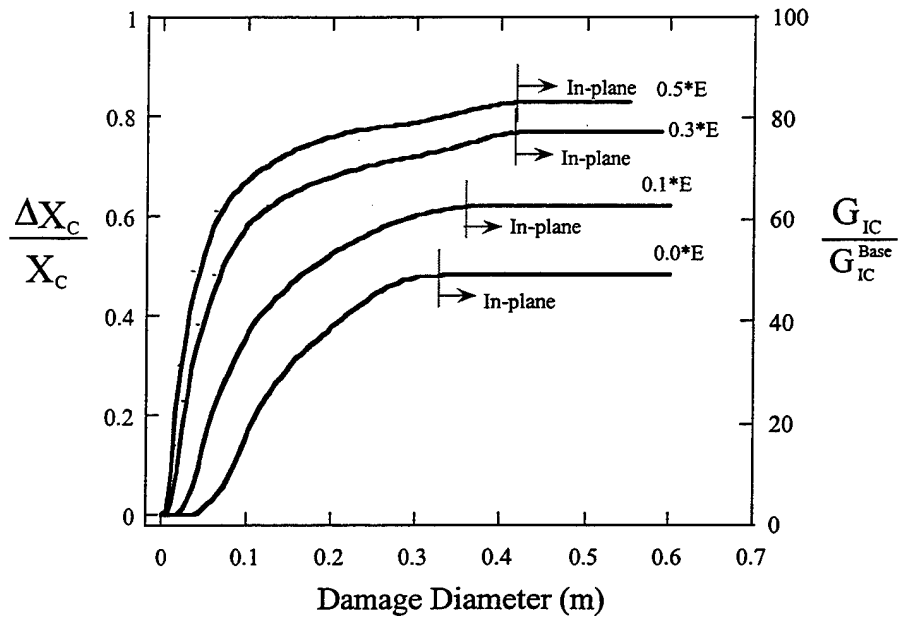
Figure 91. **Design Graph Indicating the Interdependent Effects of Inclusion Stiffness, Fracture Toughness, and Damage Size on Improving Residual Strength.**

126

In Figure 91, the strength improvement $\frac{\Delta X_C}{X_C}$, and fracture toughness is plotted as a function of damage diameter. The strength improvement is normalized by the maximum membrane strength achievable, X_C, for each inclusion stiffness. Mathematically, X_C can be expressed as:

$$X_C = X_C^0\left(1 + \frac{\Delta X_C}{X_C^0}\right), \tag{38}$$

where X_C^0 is the compression strength given by the baseline G_{IC} curve and ΔX_C is the optimal strength improvement for a given damage size, D.

The fracture toughness, $\frac{G_{IC}}{G_{IC}^{Base}}$, is normalized by the nonstitched baseline toughness, G_{IC}^{Base}, of the material (here taken to be 100 J/m^2). For very small damage sizes, Figure 91 shows that there is no improvement in residual strength that can be obtained by increasing G_{IC} because D < D* (see Figure 90). As the damage size becomes greater than D*, a rapid increase in $\frac{\Delta X_C}{X_C}$ results with improvements in fracture toughness. For D >> D*, the maximum $\frac{\Delta X_C}{X_C}$ is achieved and increasing G_{IC} further is no longer beneficial. For higher in-plane inclusion stiffness, the curves exhibit steeper slopes. Large inclusion stiffnesses allow for greater improvement in residual strength for larger increases in G_{IC} and damage size.

As further studies are conducted into the effect of stitching parameters on ballistic performance and fracture toughness, design charts similar to Figure 91 can be used to optimize fracture toughness, and consequently, to achieve the optimal solution for both multiple impact performance and residual strength. The desired G_{IC} depends on the relative importance of multihit capability and residual strength as specified in the design criteria.

6. Conclusions and Future Work

6.1 Conclusions. Damage tolerance of thick-section-composite armor has two main objectives: (1) to sustain multiple ballistic impacts, and (2) to retain structural functionality after impact induced damage has occurred. In order to achieve these objectives, an experimental study was conducted in section 4 to determine the effects of through-the-thickness stitching, ceramic tiles, matrix material, and processing on-damage tolerance. In conjunction with the experimental study, analytical and finite element analysis was conducted in an effort to achieve a fundamental understanding of the predominant CABI modes of failure. There are two primary competing mechanisms of failure in a CABI-loaded panel as discussed in section 3: (1) membrane failure due to stress concentrations around the damaged region and (2) unstable delamination growth due to interlaminar defects. The dominant mode of failure is determined by the relative importance of fracture toughness and in-plane inclusion stiffness. In section 5, a parametric study was conducted to determine the effects of inclusion stiffness and fracture toughness on residual strength and multi-impact performance. A methodology was then demonstrated by which design charts could be formed to achieve the optimum multihit ballistic performance and residual strength, based on functionality requirements.

6.1.1 Effect of Material System, Stitching, and Processing on Multiple Impact Performance and Residual Strength. As reported in section 4, three resin systems were investigated for their multi-impact performance and CABI strength in various combinations with two different S-2 glass fabrics. The resin system and glass preforms were chosen based on previous usage on military vehicles and proposed usage on future vehicles. Panels were made with a twill weave, 18-oz S-2 glass fabric used in the CAV and a plain weave 24-oz S-2 glass fabric prepreg used in the CIFV. The resin systems considered were vinyl ester 411-C50, SC-4 epoxy, and CYCOM polyester (prepreg). The SC-4 epoxy and polyester CYCOM prepreg were used in CAV and CIFV, respectively. The vinyl ester 411-C50 resin is proposed as an inexpensive alternative. The vinyl-ester and SC-4 laminates were manufactured using the SCRIMP process, while the CYCOM prepreg laminates were manufactured by hand layup. A

number of preforms were stitched through the thickness with Kevlar thread prior to resin injection, in order to improve multi-impact performance and residual strength.

Of the two fiber preforms, the 24-oz systems exhibited slightly better multi-impact performance regardless of the resin system. Average damage diameters were 9–12% less than that of the 18-oz systems. However, CABI strength for both 24-oz and 18-oz systems was virtually identical.

The vinyl-ester-resin system demonstrated equivalent multi-impact performance to the SC-4 resin. The CYCOM systems exhibited the poorest performance particularly near the back surfaces in which almost the entire area was delaminated. CABI strength for the vinyl-ester and SC-4 systems were within one standard deviation, while the CYCOM panels demonstrated CABI strengths 50–60% lower.

The relatively poor multi-impact and CABI strength properties of the CYCOM panels is most likely due to the hand layup manufacturing process, rather than the polyester resin system. As mentioned in section 2, the properties of polyester is comparable to that of vinyl ester and it is therefore unlikely that the matrix material would cause such a large difference in damage tolerance. The CYCOM panels manufactured by the hand layup process exhibited higher void content than panels made using SCRIMP. Olson et al. (1995) showed that high-void content can significantly reduce strength properties. Thus, relatively inexpensive manufacturing procedures such as SCRIMP can result in higher damage tolerant systems than laminates made using the hand layup procedure.

The stitched laminates proved beneficial in reducing damage size. In the vinyl-ester systems, Kevlar stitching reduced damage diameter on average by 18%, while in the SC-4 systems, stitching reduced damage diameter by 24%. However, despite the reduced damage size achieved through the large increase in G_{IC} from stitching, no gains in residual strength were obtained. This is due to the dominant compression failure mechanism and will be discussed in the next section.

Panels with a ceramic tile bonded showed a change in damage distribution upon impact. The damage was cylindrical rather than conical, as was the case in the nontiled systems. The difference in damage profile is likely due to the fact that the projectile did not penetrate the specimen in the tile case as it did in the nontiled case. Thus, the damage in the tile case is mostly due to the stress-wave propagation, whereas in the nontile case penetration of the projectile causes interlaminar cracks to propagate. The multi-impact benefits of stitching would be realized if targets are shot at higher velocity where penetration and arrest of the FSP would occur in the stitched composite panels. Results indicate that the backing plate would most likely be delaminated prior to arrival of the projectile. Further investigations are still needed to investigate the effect of ceramic tiles.

6.1.2 *CABI Failure Modes*.

6.1.2 CABI Failure Modes. Analytical and finite element analysis was conducted in this study to gain an understanding into the governing factors affecting CABI strength. Residual strength is primarily dependant on the critical Mode I fracture toughness, the in-plane inclusion stiffness, finite width effects and loading condition. The relative importance of these variables determines whether failure will occur due to stress concentrations in the vicinity of the damaged region, or due to unstable delamination growth.

The analytical technique combines Lekhnitskii's analysis and the PSC for in-plane failure, and instability-related delamination growth based on Flanagan's (1988) criteria. The analysis was experimentally validated for thin-section carbon/epoxy systems and thick-section glass/vinyl-ester and polyester systems. To account for finite width effects for the in-plane failure mode, it was necessary to employ finite element analysis to determine the stress distribution before applying the PSC.

In section 3, a case study was examined in which S-2 glass/polyester CYCOM prepreg panels were ballistically damaged and measured for residual strength. Analysis showed that the predominant failure mode was unstable delamination growth. Since delamination growth failure is a function of the fracture toughness, it was determined that increasing G_{IC} would lead to higher

residual strength. In addition, improving G_{IC} increases the allowable defect size, thus improving multi-impact performance.

To improve G_{IC}, through-the-thickness Kevlar stitching was used. DCB testing showed that stitching improved fracture toughness 6–10 times in S-2 glass/vinyl-ester laminates. Experimental work described in section 4 showed that the increase in G_{IC} due to stitching resulted in smaller damage sizes yet did not result in any improvement in compression strength. The normalized strength values shown in Figure 77 indicated that panels most likely failed by the in-plane failure mode. In section 3, it was shown that the stress concentration factor, K_T, had a value of 4.6 for notched orthotropic plates of finite width. Thus, the notched strength of an orthotropic panel is 22% that of an undamaged plate. An examination of Figure 77 shows that the normalized strength also has values ranging between 26% and 35% of the undamaged strength. Model predictions superimposed with experimental data also indicated that severe in-plane stiffness losses in the damaged region (80% stiffness loss) lead to high stress concentrations resulting in membrane failure. Since membrane failure is not dependent on fracture toughness, no strength improvements were gained with the use of stitching.

6.1.3 Optimization of Multi-Impact Resistance and CABI Strength. While stitching was shown to improve multi-impact performance, it may also lead to an increase in fiber damage, causing the failure mode to shift from delamination growth to membrane failure. In such a case, increasing G_{IC} beyond a certain point provides no further strength improvements and may, in fact, be detrimental. Thus, a design trade-off exists between maximum fracture toughness and damage induced in-plane stiffness reduction.

To optimize both multiple impact performance and residual strength, the stitching parameters must be carefully designed such that fracture toughness is increased just enough to arrest ballistic damage within the allowable. Recall that in section 3 damage tolerance was defined in terms of the delamination growth failure mode, in which case smaller damage area increased compression strength. However, the potential for membrane failure tends to increase for smaller damage

sizes, since the inclusion stiffness is reduced as ballistic energy is contained within a smaller area. In this case, additional increases in G_{IC} may only lead to further reductions in in-plane stiffness, and consequently lower strength. Through the analytical model presented in this study, design graphs indicating the interdependent effects of inclusion stiffness, fracture toughness and damage size on improving residual strength may be formed. From these charts, the designer may decide what degree of G_{IC} improvement is needed, and adjust the stitching parameters accordingly.

Optimization of multi-impact performance and residual strength is necessarily an iterative process since improving one may affect the other. The flow chart of Figure 92 shows the methodology of optimizing damage tolerance. Firstly, a panel with given material and strength properties is damaged ballistically. The damage size is then determined using NDE and the inclusion stiffness is determined through compression strain measurements as described in section 4. Using this data, a design chart is formed. At this point, a preliminary decision must be made: is the damage size larger than the critical damage size? Here a complication arises, since the critical defect size does not carry the same definition for membrane and delamination growth failure. In this instance, the critical defect size is taken to be the size by which multiple impacts may occur without the damaged areas overlapping. By this definition, if the critical defect size is exceeded, then the fracture toughness is increased by varying the stitch parameters. If the critical defect size is not exceeded, then an assessment is made based on the design chart as to whether increasing G_{IC} will improve residual strength. If it does not, then an assessment is made as to whether the residual strength is sufficient to meet the design requirements. If not, G_{IC} is reduced in order to increase the inclusion stiffness after impact. The process is then repeated until residual strength and multi-impact performance is optimized.

6.2 Recommendations for Future Work. In this study, the factors affecting damage tolerance of thick-section composites were examined. From the analytical and experimental work conducted, it was shown that a trade-off exists between multi-impact performance and
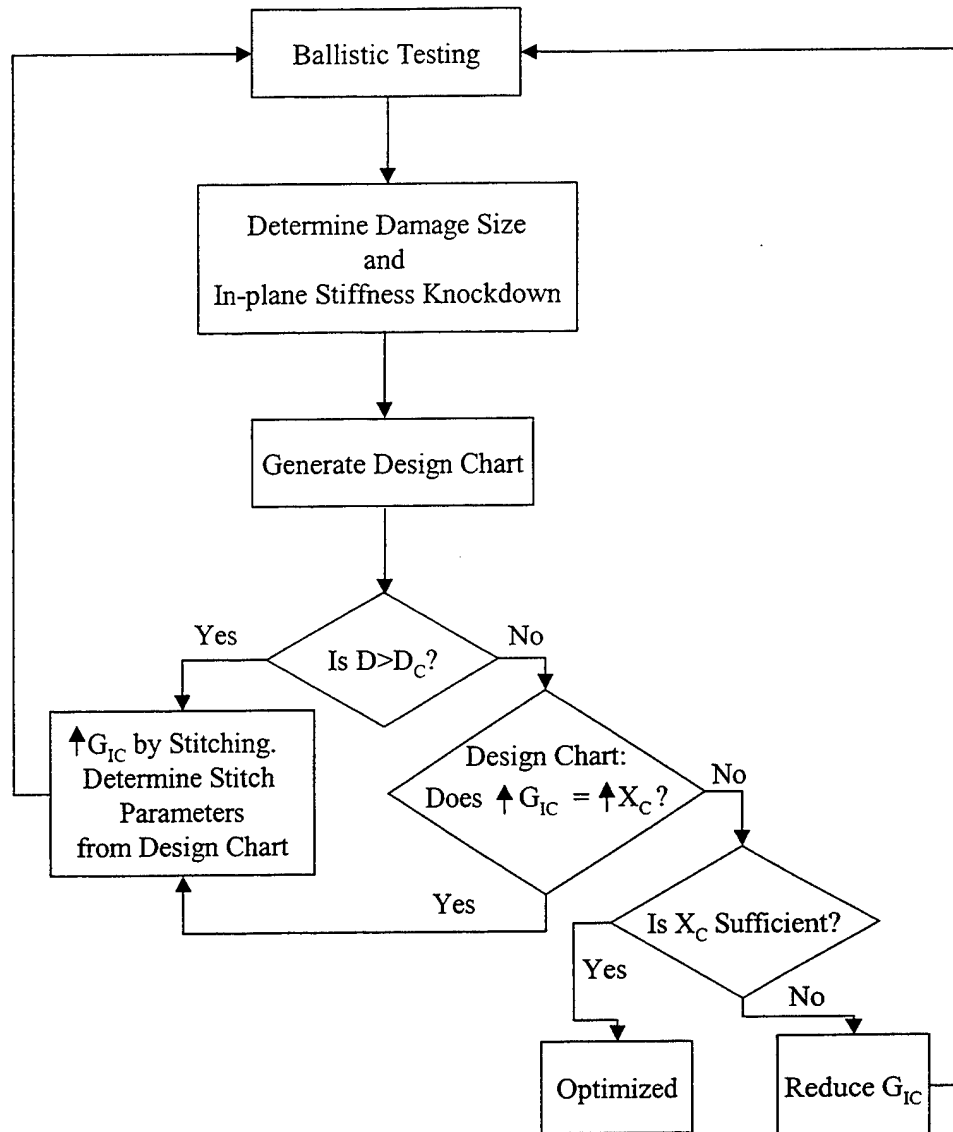
Figure 92. Flow Chart of Design Process for Multi-Impact and Residual Strength Optimization. D_C Is Defined in Terms of Multi-Impact Performance.

residual strength. A methodology was then developed to determine the fracture toughness required to optimize damage tolerance.

It is yet unclear as to how fracture toughness affects multi-impact performance. Experimental and analytical work is much needed to understand the damage evolution within composites during ballistic impact. Fracture toughness is also rate dependant and a distinction

must be made between the static fracture toughness affecting residual strength and the dynamic fracture toughness affecting ballistic performance.

On a smaller scale, additional experimental work is needed on S-2 glass/resin systems to determine the effects of stitch parameters on inclusion stiffness and fracture toughness. Optimization of damage tolerance is not possible without this understanding.

In addition to through-the-thickness stitching, other means of improving damage tolerance of thick-section composites need be examined. Chemical pretreatments and toughened matrix materials may be added to tailor the fiber matrix interface bonding, for optimal energy absorption. Improved processing techniques should be examined to improve part quality and minimize void content, in order to improve residual strength. Preliminary investigations performed in this study have shown that SCRIMP processing provides better part quality than hand layup.

7. References

Adanur, S., Y. P. Tsao, and C. W. Tam. "Improving Fracture Resistance of Laminar Textile Composites by Third Direction Reinforcement." *Composites Engineering*, vol. 5, no. 9, pp. 1149–1158, 1995.

American Society for Testing and Materials. "Standard Test Method for Compressive Properties of Unidirectional or Cross-Ply Fiber-Resin Composites." *Annual Book of ASTM Standards*, ASTM D3410M-95, Conshohocken, PA, 1995a.

American Society for Testing and Materials. "Standard Test Method for Mode I Interlaminar Fracture Toughness of Unidirectional Fiber-Reinforced Polymer Matrix Composites." *Annual Book of ASTM Standards*, ASTM D5528, Conshohocken, PA, 1995b.

Ashizawa, M. "Fast Interlaminar Fracture of a Compressively Loaded Composite Containing a Defect." *Fifth DOD/NASA Conference on Fibrous Composites in Structural Design*, New Orleans, LA, 1981.

Awerbuch, J., and M. S. Madhukar. "Notched Strength of Composite Laminates: Predictions and Experiments—A Review." *Journal of Reinforced Plastics and Composites*, vol. 4, p. 3, 1985.

Berry. J. P. "Determination of Fracture Surface Energies by Cleavage Technique." *Journal of Applied Physics*, vol. 34, no. 1, p. 62, 1963.

Blake, R. A., and R. B. Pipes. *Test Methods, Volume 6. Delaware Composites Design Encyclopedia*, Lancaster, PA: Technomic Publishing Co. Inc., 1990.

Bossi, R. H., K. D. Friddell, and A. R. Lowerey. *Non-Destructive Testing of Fibre Reinforced Plastics Composites*. Vol. 2, ch. 4, New York: Elsevier Applied Sciences Publishing Co., 1990.

Broek, D. *Elementary Engineering Fracture Mechanics*. Dordrecht: Martinus Nijhoff Publishers, 1986.

Cairns, D. S. "Impact and Post-Impact Response of Graphite/Epoxy and Kevlar/Epoxy Structures." TELAC Report 87-15, Massachusetts Institute of Technology, Cambridge, MA, August 1987.

Chai, H. "The Growth of Impact Damage in Compressively Loaded Laminates." Ph.D dissertation, California Institute of Technology, Pasadena, CA, 1982.

Chai, H., and C. D. Babcock. "Two Dimensional Modeling of Compressive Failure in Delaminated Laminates." *Journal of Composite Materials*, vol. 19, no. 1, pp. 67–98, 1985.

Chatterjee, S. N., W. A. Dick, and R. B. Pipes. "Mixed-Mode Delamination Fracture in Laminated Composites." *Composites Science and Technology*, vol. 25, no. 1, pp. 49–67, 1986.

Chou, S-C., and E. DeLuca. "Dynamic Response of S-2 Glass Reinforced Plastic Structural Armor—A Progress Report." ARL-SR-5, U.S. Army Research Laboratory, Aberdeen Proving Ground, MD, 1993.

Chou, T-W., and F. Ko. *Textile Structural Composites*. New York: Elsevier Applied Sciences Publishing Co., 1989.

Department of Defense. "Thread, Para-Aramid, Intermediate Modulus." DOD 4120.25-M, Defense Standardization Program Policies and Procedures, Washington, DC, March 2000.

Dow, M. B., and D. L. Smith. "Damage Tolerant Composite Materials Produced by Stitching Carbon Fibres." *Proceedings of 21st International SAMPE Technical Conference*, pp. 595–605, 1989.

Dow, M. B., D. L. Smith, and S. J. Luowinski. "An Evaluation of Stitching Concepts for Damage Tolerant Composites." NASA Conference Publication 3038, pp. 53–74, 1989.

Dransfield, K., C. Baillie, and Y. Mai. "Improving the Delamination Resistance of CFRP by Stitching—A Review." *Composites Science and Technology*, vol. 50, no. 3, pp. 305–317, 1994.

El-Denussi, A. K., and J. P. H. Weber. "Blister Delamination Analysis in Fiber Reinforced Plastics Using Beam-Column Theory With an Energy Release Rate Criterion." *Composite Structures*, vol. 5, pp. 125–131, 1986.

Fecko, D. L. "In-Situ Ultrasonic Porosity Monitoring for the Thermoplastic Matrix Pultrusion Process." CCM Report 96-10, Center for Composite Materials, University of Delaware, Newark, DE, 1996.

Fink, B. K., S. H. McKnight, and J. W. Gillespie, Jr. "Co-Injection Resin Transfer Molding for Optimization of Integral Armor." *Proceedings of the Army Science Conference*, Norfolk, VA, 15–17 June 1998.

Fink, B. K., E. F. Gillio, G. P. McKnight, J. W. Gillespie, S. G. Advani, R. F. Eduljee, and K. R. Bernetich. "Co-Injection Resin Transfer Molding of Vinyl-Ester and Phenolic Resins." ARL-TR-2150, U.S. Army Research Laboratory, Aberdeen Proving Ground, MD, January 2000.

Fink, B. K., and J. W. Gillespie. "Cost-Effective Manufacturing of Damage Tolerant Integral Armor." ARL-TR-2319, U.S. Army Research Laboratory, Aberdeen Proving Ground, MD, September 2000.

Fink, B. K. "Performance Metrics for Composite Integral Armor." *Journal of Thermoplastic Composite Materials*, vol. 13, pp. 417–431, September 2000.

Flanagan, G. "Two-Dimensional Delamination Growth in Composite Laminates Under Compression Loading." *Composite Materials Testing and Design (Eighth Conference)*, pp. 180–190, 1988.

Garg, A. C., and Y. W. Mai. "Failure Mechanisms in Toughened Epoxy Resin—A Review." *Composites Science and Technology*, vol. 31, no. 3, pp. 179–223, 1988.

Gillespie, J. W., Jr., and R. B. Pipes. "Compressive Strength of Composite Laminates With Interlaminar Defects." *Composite Structures*, vol. 2, no. 1, pp. 49–69, 1984.

Gillespie, J. W., Jr., and L. A. Carlsson. "Influence of Finite Width on Notched Laminate Strength Predictions." *Composites Science and Technology*, vol. 32, no. 1, pp. 15–30, 1988.

Gillespie, J. W., Jr., R. J. Rothschilds, and L. A. Carlsson. "Instability-Related Delamination Growth in Thermoset and Thermoplastic Composites." *Composite Materials Testing and Design*, ASTM-STP-972, pp. 93–98, Conshohocken, PA: American Society for Testing and Materials, 1988.

Gillespie, J. W., Jr., and L. A. Carlsson. "Buckling and Growth of Delamination in Thermoset and Thermoplastic Composites." *Journal of Engineering Materials and Technology*, vol. 113, pp. 93–98, 1991.

Gillespie, J. W., Jr. "Damage Tolerance of Composite Structures: The Role of Interlaminar Fracture Mechanics." *Journal of Offshore Mechanics and Arctic Engineering*, vol. 113, no. 3, pp. 247–252, August 1991.

Gillio, E. F. "Co-Injection Resin Transfer Molding of Hybrid Composites." CCM Report 97-23, Center for Composite Materials, University of Delaware, Newark, DE, 1997.

Gowariker, V. R., et al. *Polymer Science*. New Delhi: Wiley Eastern Limited, 1986.

Guenon, V. A. F. "Interlaminar Fracture Toughness of a Three-Dimensional Composite." CCM Report 88-01, Center for Composite Materials, University of Delaware, Newark, DE, January 1988.

Gum, W. F., W. Riese, and H. Ulrich. *Reaction Polymers*. Munich: Hanser Publishers, distributed in the USA by Oxford University Press, January 1992.

Guynn, E. G., and T. K. O'Brien. "The Influence of Lay-Up and Thickness on Composite Impact Damage and Compression Strength." AIAA Paper No. 85-0646, American Institute of Aeronautics and Astronautics, 1985.

Henshaw, J. M., J. R. Sorem, Jr., and E. H. Glaessgen. "Finite Element Analysis of Ply-by-Ply and Equivalent Stress Concentrations in Composite Plates With Multiple Holes Under Tensile and Shear Loading." *Composite Structures*, vol. 36, issue no. 1–2, pp. 45–58, September–October 1996.

Hetherington, J. G., and P. F. Lemieux. "The Effect of Obliquity on the Ballistic Performance of Two Component Composite Armours." *International Journal Impact Engineering*, vol. 15, no. 2, pp. 131–137, April 1994.

Hinrichs, S. C., D. C. Jegley, and J. T. Wang. "Structural Analysis and Test of a Stitched Composite Wing Box." Presented at the Sixth NASA/DOD Advanced Composite Technology Conference, Anaheim, CA, 1995.

Horton, R. E., and R. S. Whitehead. "Damage Tolerance of Composites, Volume I. Development of Requirements and Compliance Demonstration." AFWAL-TR-87-3030, U.S. Air Force, Wright Air Force Base, OH, 1988.

Huang, S. L., R. J. Richey, and E. W. Deska. "Cross Reinforcement in a GR/EP Laminate." Presented at the American Society of Mechanical Engineers, Winter Annual Meeting, 15 October 1978.

Huang, X. Personal communication. Center for Composite Materials, University of Delaware, Newark, DE, 1998.

Johnson, W. S., and P. D. Mangalgiri. "Influence of the Resin on Interlaminar Mixed-Mode Fracture." NASA Technical Memorandum 87571, National Aeronautics and Space Administration, Washington, DC, 1985.

Kan, H. P., and M. J. Graves. "Damage Tolerance of Composites—Volume III; Analysis, Methods, Development, and Test Verification." AFWAL-TR-87-3030, 1988.

Kim, J., and Y. Mai. *Engineered Interfaces in Fiber Reinforced Composites*. New York: Elsevier Applied Sciences Publishing Co., 1998.

Kinloch, A. J., and R. J. Young. *Structural Adhesives: Development in Resins and Primers*. London: Elsevier Applied Sciences Publishing Co., 1986.

Kinloch, A. J. "Rubber Toughened Thermosetting Polymers." *Structural Adhesives: Development in Resins and Primers*, London: Elsevier Applied Sciences Publishing Co., 1986.

Lee, C., and D. Liu. "Tensile Strength of Stitching Joint in Woven Glass Fabrics." *Journal of Engineering Materials and Technology*, vol. 112, pp. 125–130, 1990.

Lekhnitskii, S. G. *Anisotropic Plates.* New York: Gordon and Breach Science Publishers, 1968.

Liu, D. "Delamination Resistance in Stitched and Unstitched Composite Planes Subjected to Composite Loading." *Journal of Reinforced Plastics and Composites,* vol. 9, pp. 59–69, 1990.

Madan, R. C. "The Influence of Low-Velocity Impact on Composite Structures." *ASTM Third Symposium on Composite Materials,* Orlando, FL, 1989.

Mar, J. W., and K. Y. Lin. "Fracture Mechanics Correlation for Tensile Failure of Filamentary Composites With Holes." *Journal of Aircraft,* vol. 14, no. 7, pp. 703–704, 1977.

Marsh, G. "Getting it Together." *Aerospace Composites and Materials,* vol. 2, no. 4, pp. 10–12, 1990.

Martin, R. H. "Delamination Characterization of Woven Glass/Polyester Composites." *Journal of Composite Technology and Research,* vol. 19, no. 1, pp. 20–28, 1997.

Mignery, L. A., C. T. Sun, and T. M. Tan. "The Use of Stitching to Suppress Delamination in Laminated Composites." ASTM STP 876, American Society for Testing and Materials, pp. 371–385, Conshohocken, PA, 1985.

Monib, A. M., J. W. Gillespie, Jr., and B. K. Fink. "Damage Tolerance of Composite Laminates Subjected to Ballistic Impact." *Proceedings of the Annual Meeting of the Society of Plastics Engineers: ANTEC,* pp. 1463–1467, Brookfield, CT, 1998.

Morales, A. "Structural Stitching of Textile Preforms." Proceedings of the 22nd International SAMPE Technical Conference, 1990.

Naval Air Development Center. "Certification Testing Methodology for Composite Structure, Volumes I & II." NADAC-87042-60, Patuxent River, MD, 1986.

Nyman, T., A. Bredberg, and J. Schon. "Equivalent Damage and Residual Strength for Impact Damaged Composite Structures." *Proceedings of the 13th Annual Technical Conference of the American Society for Composites,* pp. 1759–1775, Los Angeles, CA: American Society for Composite Materials, 21–23 September 1998.

Ogo, Y. "The Effects of Stitching on In-plane and Interlaminar Properties of Carbon-Epoxy Fabric Laminates." Master's thesis, University of Delaware, Newark, DE, 1987.

Olson, B. D., J. W. Gillespie, Jr., and T. A. Bogetti. "The Effects of Non-Destructive Evaluation of Defects in Thermoplastic Compression-Loaded Composite Cylinders." *Journal of Thermoplastic Composite Materials,* vol. 8, no. 1, pp. 109–136, January 1995.

Pipes, R. B., R. A. Blake, J. W. Gillespie, Jr., and L. A. Carlsson. *Test Methods, Volume 6. Delaware Composites Design Encyclopedia.* Lancaster, PA: Technomic Publishing Co., Inc., 1990.

Pipes, R. B., R. C. Wetherhold, and J. W. Gillespie, Jr. "Notched Strength of Composite Materials." *Journal of Composite Materials*, vol. 12, pp. 148–160, April 1979.

Poe, C. C. "Fracture Mechanics Methodology for Two-Bay Crack in Stitched-RFI Wing Skin." *Presented at the 11th DOD/NASA/FAA Conference on Fibrous Composites in Structural Design*, Fort Worth, TX, 1996.

Portanova, M. A. "Evaluation of the Impact Response of Textile Composites." NASA Technical Report NASA-CR-198265, Langley, VA, December 1995.

Ramkumar, R. L. "Environmental Effects of Composite Damage Criticality, Final Technical Report." NADC-79067-60, Naval Air Development Center, Patuxent River, MD, 1982.

Rothschilds, R. J., J. W. Gillespie, Jr., and L. A. Carlsson. "Instability-Related Delamination Growth in Thermoset and Thermoplastic Composites." *Proceedings of Composite Materials: Testing and Design (Eighth Conference)*, Philadelphia, PA, pp. 161–179, 1988.

Sallam, S., and G. J. Simitses. "Delamination Buckling and Growth of Flat Cross-Ply Laminates." *Composite Structures*, vol. 4, no. 4, pp. 361–383, 1985.

Sankar, B. V. "Interlaminar Fracture Toughness of Stitched Graphite/Epoxy Laminates." Presented at the 11th DOD/NASA/FAA Conference on Fibrous Composites in Structural Design, Fort Worth, TX, 1996.

Seemann, W. H., III. "Plastic Transfer Molding Techniques for the Production of Fiber Reinforced Plastic Structures." U.S. Patent 4,902,215, February 1990.

Stone, M. "Thermo-Chemical and Thermo-Mechanical Response of Reacting Polymers." CCM Report 97-13, Center for Composite Materials, University of Delaware, Newark, DE, May 1997.

Strong, A. B. *Fundamentals of Composites Manufacturing: Materials, Methods, and Applications.* Dearborn, MI: Society of Manufacturing Engineers, 1989.

Susuki, I., and T. Takatoya. "Impact Damage Properties of 3-D Carbon/Bismaleimide Composites." Damage Mechanism Section, Airframe Division, National Aerospace Laboratory, 7-44-1, Jindaiji Higashi-Machi, Chofu, Tokyo 182, Japan, 1997.

Tan, S. C. *Stress Concentrations in Laminated Composites.* Lancaster, PA: Technomic Publishing Co., Inc., 1994.

Thomas, G., A. Larson, and J. Garces. "Composite Hull Program Final Technical Report." ARL-CR-179, U.S. Army Research Laboratory, Aberdeen Proving Ground, MD, prepared by United Defense, Ltd., Ground Systems Division, Santa Clara, CA, December 1994.

U.S. Army Research Laboratory. "V50 Ballistic Test for Armor." MIL-STD-662E, Aberdeen Proving Ground, MD, January 1987.

U.S. Department of Justice. "Ballistic Resistance of Police Body Armor." NIJ Standard 0101.03, National Institute of Justice, Washington, DC, 1987.

Wang, J. T., D. C. Jegley, H. G. Bush, and S. C. Hinrichs. "Correlation of Structural Analysis and Test Results for the McDonnell Douglas Stitched/RFI All-Composite Wing Stub Box." *Presented at the 11th DOD/NASA/FAA Conference on Fibrous Composites in Structural Design*, Fort Worth, TX, 1996.

Wanthal, S. P., C. A. Fracchia, H. Dill, and J. C. Goering. "Delamination Methodology for Composite Structures Volumes I & II, Final Technical Report." DOT/FAA Report No. DOT/FAA/CT-94/55-I NAWCADWAR P.O.C., Naval Air Warfare Center, Aircraft Division, Warminster, PA, 1993.

Whitcomb, J. D. "Finite Element Analysis of Instability Related Delamination Growth." *Journal of Composite Materials*, vol. 15, pp. 403–426, September 1981.

Whitcomb, J. D. "Three-Dimensional Analysis of a Postbuckled Embedded Delamination." *Journal of Composite Materials*, vol. 23, no. 9, pp. 862–889, September 1989.

Whitney, J. M., and R. J. Nuismer. "Stress Fracture Criteria for Laminated Composites Containing Stress Concentrations." *Journal of Composite Materials*, vol. 8, pp. 253–265, July 1974.

Williams, J. G. "Effect of Damage and Open Holes on the Compression Strength of Tough Resin High Strain Fiber Laminates." NASA Technical Memorandum 85756, National Aeronautics and Space Administration, Washington, DC, 1984.

Xiong, Y., C. Poon, P. V. Straznicky, and H. Vietinghoff. "A Prediction Method for the Compressive Strength of Impact Damaged Composite Laminates." *Composite Structures*, vol. 30, no. 4, pp. 357–367, 1995.

Yin, W. L. "The Effects of Laminated Structure on Delamination Buckling and Growth." *Journal of Composite Materials*, vol. 22, no. 6, pp. 502–517, 1988.

Yin, W. L., and Z. Fei. "Delamination Buckling and Growth in a Clamped Circular Plate." *American Institute of Aeronautics and Astronautics Journal*, vol. 26, no. 4, pp. 438–445, April 1985.

Ziaee, S. Personal communication. Center for Composite Materials, University of Delaware, Newark, DE, 1999.

Zukas, J. A., T. Nicholas, H. F. Swift, L. B. Greszczuk, and D. R. Curran. *Impact Dynamics*. New York: John Wiley & Sons, Inc., 1982.

Appendix:

Ultrasonic Images

INTENTIONALLY LEFT BLANK.

In this appendix, sample ultrasonic images of the 18-oz S-2 glass/SC-4 resin and 24-oz S-2 glass/CYCOM prepreg are shown. The 24 oz S-2 glass/SC-4 scans are almost identical to those of the 18 oz panels and, therefore, do not warrant exhibition. As with the vinyl-ester panels evaluated in section 4, the SC-4 and CYCOM panels are scanned at three different depth locations. The first scan, called gate 1, is taken at a location just below the impact surface at a depth approximately 10% of total thickness. Gate 2 is located at the middle of the panel, while gate 3 is located near the back face at a depth approximately 80% of total thickness. Figure A-1 shows an ultrasonic scan comparison for nonstitched vs. stitched SC-4 panels. Figure A-2 depicts scans of tiled SC-4 panels, both stitched and nonstitched. Figure A-3 shows scans for the CYCOM panels with and without tiles. There are no stitched CYCOM panels. Table A-1 summarizes the test results for the different panels made with the 18-oz twill weave, including the vinyl-ester panels. Table A-2 summarizes the results for the 24-oz panels, and Table A-3 provides the results of the CYCOM polyester panels.
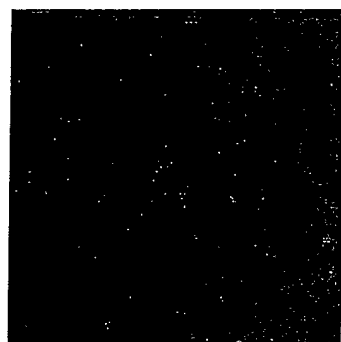
Gate 1   Gate 1
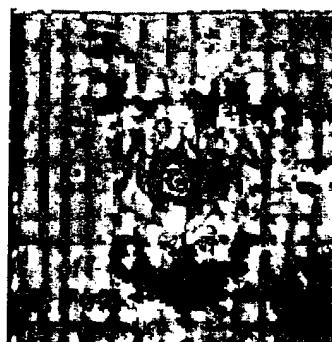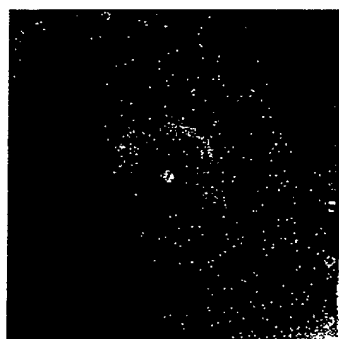
Gate 2   Gate 2
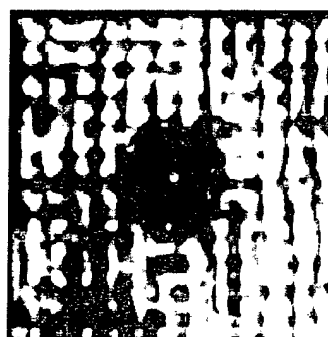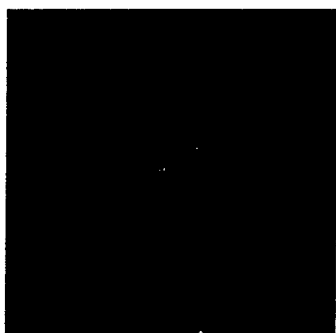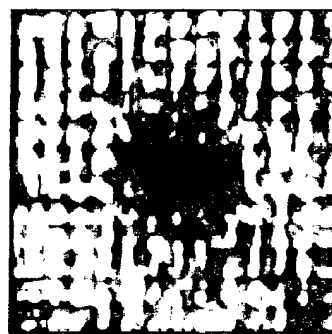
Gate 3   Gate 3

(a)   **(b)**

Figure A-1. Ultrasonic Scans of SC-4 Panels, (a) Nonstitched and (b) Stitched. Gate 1 Is Taken Just Below the Surface at a Depth Approximately 10% of the Total Thickness. Gate 2 Is at the Midplane, and Gate 3 Is at a Depth of 80% of Total Thickness.

146
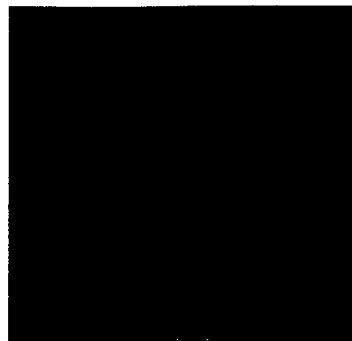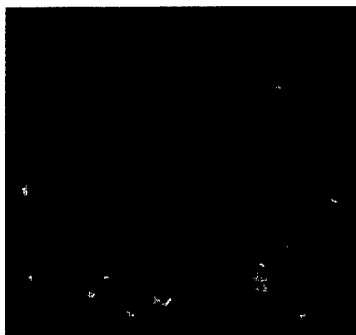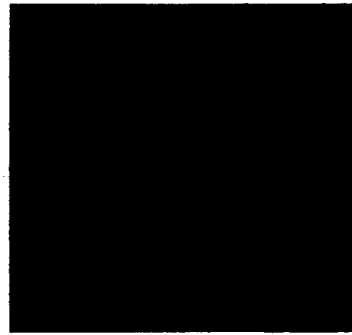
Gate 1

Gate 1

Gate 2

Gate 2

Gate 3

Gate 3

(a)

(b)

Figure A-2. Ultrasonic Scans of SC-4 Tiled Panels, (a) Nonstitched and (b) Stitched. Gate 1 Is Taken Just Below the Surface at a Depth Approximately 10% of the Total Thickness. Gate 2 Is at the Midplane, and Gate 3 Is at a depth of 80% of Total Thickness.

147

Gate 1   Gate 1

Gate 2   Gate 2

Gate 3   Gate 3
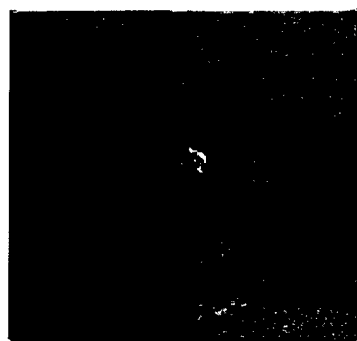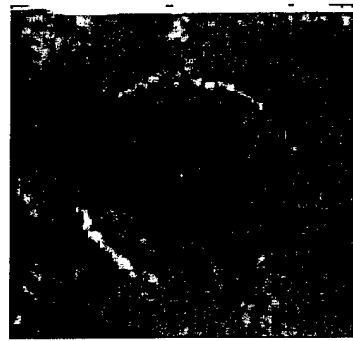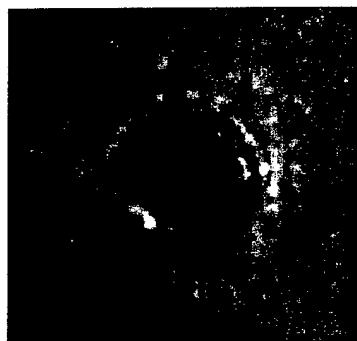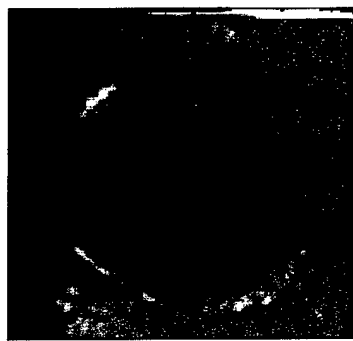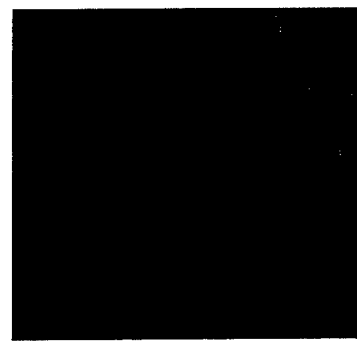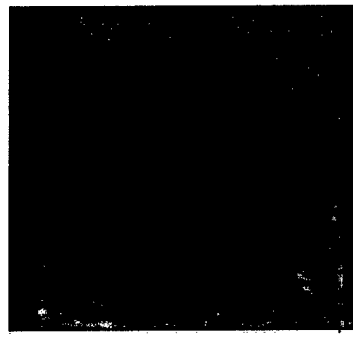
(a)   (b)

Figure A-3. **Ultrasonic Scans of CYCOM Panels, (a) With No Tile and (b) With Tile. Gate 1 Is Taken Just Below the Surface at a Depth Approximately 10% of the Total Thickness. Gate 2 Is at the Midplane, and Gate 3 Is at a Depth of 80% of Total Thickness.**

148

Table A-1. Summary Table of Damage Sizes at Different Gate Locations for the Different Panel Types[a, b]

Panel ID	Sample Description	Gate 1 Damage (cm [in])	Gate 2 Damage (cm [in])	Gate 3 Damage (cm [in])	Average Gates 2 and 3 (cm [in])
VE_1	Vinyl ester	(5.84) [2.30]	(14.43) [5.68]	(14.43) [5.68]	(14.43) [5.68]
VE_2	Vinyl ester	(7.87) [3.10]	(14.61) [5.75]	(14.61) [5.75]	(14.61) [5.75]
VE_3	Vinyl ester	(6.48) [2.55]	(12.85) [5.06]	(13.18) [5.19]	(13.02) [5.13]
VE_4	Vinyl ester	(6.83) [2.69]	(14.45) [5.69]	(14.96) [5.89]	(14.71) [5.79]
VE_5	Vinyl ester	(5.97) [2.35]	(13.92) [5.48]	(13.95) [5.49]	(13.93) [5.49]
VEs_1	Vinyl ester/stitch	(6.02) [2.37]	(9.40) [3.70]	(11.94) [4.70]	(10.67) [4.20]
VEs_2	Vinyl ester/stitch	(8.05) [3.17]	(10.24) [4.03]	(13.46) [5.3]	(11.85) [4.67]
VEs_3	Vinyl ester/stitch	(5.51) [2.17]	(11.38) [4.48]	(11.86) [4.67]	(11.62) [4.58]
VEs_4	Vinyl ester/stitch	(5.41) [2.13]	(12.07) [4.75]	(12.04) [4.74]	(12.05) [4.75]
VEt_1	Vinyl ester/tile	(18.03) [7.10]	(18.80) [7.40]	(19.89) [7.83]	(19.34) [7.62]
VEt_2	Vinyl ester/tile	(17.52) [6.90]	(18.80) [7.40]	(12.04) [7.80]	(19.29) [7.60]
VEt-s_1	Vinyl ester/stitch and tile	(5.74) [2.26]	(11.63) [4.58]	(17.35) [6.83]	(14.49) [5.71]
VEt-s_2	Vinyl ester/stitch and tile	(5.74) [2.26]	(11.55) [4.55]	(17.35) [6.83]	(14.44) [5.69]
SC4_1	SC4 epoxy	—	(14.15) [5.57]	(23.34) [9.19]	(18.74) [7.38]
SC4_2	SC4 epoxy	(6.76) [2.66]	(11.94) [4.7]	(16.43) [6.47]	(14.19) [5.59]
SC4_3	SC4 epoxy	—	(13.97) [5.5]	(23.27) [9.16]	(18.62) [7.33]
SC4_4	SC4 epoxy	(5.77) [2.27]	(14.68) [5.78]	(14.53) [5.72]	(14.61) [5.75]
SC4s_1	SC4/stitch	(5.21) [2.05]	(9.93) [3.91]	(11.28) [4.44]	(10.60) [4.18]
SC4s_2	SC4/stitch	(5.08) [2.00]	(13.56) [5.34]	(15.34) [6.04]	(14.45) [5.69]
SC4t_1	SC4/tile	—	(23.27) [9.16]	(23.62) [9.3]	(23.44) [9.23]
SC4t_2	SC4/tile	—	(20.42) [8.04]	(23.32) [9.18]	(21.87) [8.61]
SC4t-s_1	SC4/ stitch and tile	—	(19.96) [7.86]	(22.05) [8.68]	(21.01) [8.27]
SC4t-s_2	SC4/stitch and tile	—	(12.42) [4.89]	(19.71) [7.76]	(16.07) [6.33]

[a] The reinforcing fiber in all cases is the twill weave, 18-oz S-2 glass.
[b] All panel dimensions were 12 in × 12 in × 0.7 in.

Table A-2. Summary Table of Damage Sizes at Different Gate Locations for the Different Panel Types[a, b]

Panel ID	Sample Description	Gate 1 Damage (cm [in])	Gate 2 Damage (cm [in])	Gate 3 Damage (cm [in])	Average Gates 2 and 3 (cm [in])
VE_1	Vinyl ester	(5.89) [2.32]	(12.07) [4.75]	(12.27) [4.83]	(12.17) [4.79]
VE_2	Vinyl ester	(5.38) [2.12]	(11.94) [4.70]	(12.70) [5.00]	(12.32) [4.85]
VE_3	Vinyl ester	(5.23) [2.06]	(12.22) [4.81]	(13.08) [5.15]	(12.65) [4.98]
VE_4	Vinyl ester	(6.10) [2.4]	(12.22) [4.81]	(12.90) [5.08]	(12.56) [4.95]
VE_5	Vinyl ester	(5.69) [2.24]	(12.57) [4.95]	(13.36) [5.26]	(12.97) [5.11]
VEs_1	Vinyl ester/ stitch	(4.93) [1.94]	(10.64) [4.19]	(10.82) [4.26]	(10.73) [4.23]
VEs_2	Vinyl ester/ stitch	(4.78) [1.88]	(10.36) [4.08]	(10.85) [4.27]	(10.60) [4.18]
VEs_3	Vinyl ester/ stitch	(5.36) [2.11]	(9.96) [3.92]	(10.24) [4.03]	(10.10) [3.98]
Vass	Vinyl ester/ stitch	(5.08) [2.00]	(9.93) [3.91]	(10.29) [4.05]	(10.11) [3.98]
SC4_1	SC4 epoxy	(7.80) [3.07]	(12.32) [4.85]	(12.83) [5.05]	(12.57) [4.95]
SC4_2	SC4 epoxy	(8.81) [3.22]	(13.21) [5.20]	(13.36) [5.26]	(13.28) [5.23]
SC4_3	SC4 epoxy	(8.41) [3.31]	(12.70) [5.00]	(13.54) [5.33]	(13.12) [5.17]
SC4_4	SC4 epoxy	(5.87) [2.31]	(10.01) [3.94]	(11.61) [4.57]	(10.81) [4.26]
SC4_5	SC4 epoxy	(7.72) [3.04]	(13.00) [5.12]	(13.54) [5.33]	(13.27) [5.23]
SC4_6	SC4 epoxy	(8.08) [3.18]	(12.70) [5.00]	(13.61) [5.36]	(13.16) [5.18]
SC4_7	SC4 epoxy	(6.71) [2.64]	(10.82) [4.26]	(13.97) [5.50]	(12.40) [4.88]
SC4_8	SC4 epoxy	(8.81) [3.47]	(11.96) [4.71]	(12.60) [4.96]	(12.28) [4.84]
SC4s_1	SC4/stitch	(6.20) [2.44]	(9.69) [3.78]	(9.98) [3.93]	(9.79) [3.86]
SC4s_2	SC4/stitch	(6.50) [2.56]	(10.90) [4.29]	(11.38) [4.48]	(11.14) [4.39]
SC4s_3	SC4/stitch	(6.48) [2.55]	(12.37) [4.87]	(12.65) [4.98]	(12.51) [4.93]
SC4s_1	SC4/stitch	(5.72) [2.25]	(11.84) [4.66]	(12.01) [4.73]	(11.93) [4.70]
SC4s_2	SC4/stitch	(6.40) [2.52]	(10.77) [4.24]	(10.97) [4.32]	(10.87) [4.28]

[a] The reinforcing fiber in all cases is the twill weave, 24-oz S-2 glass.
[b] All panel dimensions were 12 in × 12 in × 0.7 in.

Table A-3. **Summary Table of Damage Sizes at Different Gate Locations for the CYCOM Polyester Resin Matrix[a, b]**

Panel ID	Sample Description	Gate 1 Damage (cm [in])	Gate 2 Damage (cm [in])	Gate 3 Damage (cm [in])	Average Gates 2 and 3 (cm [in])
CYCOM no. 1	Polyester	(8.509) [3.35]	(22.96) [9.04]	(29.69) [11.69]	(26.33) [10.37]
CYCOM no. 2	Polyester	(9.68) [3.81]	(22.43) [8.83]	(27.86) [10.97]	(25.15) [9.90]
CYCOM no. 1	Polyester with tile	(12.19) [4.8]	(19.81) [7.8]	(24.64) [9.70]	(22.23) [8.75]
CYCOM no. 2	Polyester with tile	(13.41) [5.28]	(20.04) [7.89]	(23.14) [9.11]	(21.60) [8.50]

[a] The reinforcing fiber in all cases is the twill weave, 24-oz S-2 glass.
[b] All panel dimensions were 12 in × 12 in × 0.7 in.

151

INTENTIONALLY LEFT BLANK.

List of Acronyms and Abbreviations

ACT	Advanced Composite Technology (program)
ARL	U.S. Army Research Laboratory
ASTM	American Society for Testing and Materials
CABI	compression after ballistic impact
CAI	compression after impact
CAV	composite armored vehicle
CHP	cumyl hydro peroxide
CIFV	Composite Infantry Fighting Vehicle
CoNap	cobalt naphthanate
CSDS	Compression Strength of Delaminated Structure (program)
CT	computed tomography
DCB	double cantilever beam
FEA	finite element analysis
FGCS	Future Ground Combat System
FSP	fragment simulating projectile
NASA	National Aeronautics and Space Administration
NDE	nondestructive evaluation
PSC	point-stress failure criterion
RTM	resin-transfer molding
SCF	stress concentration factor
SCRIMP	Seemann Composite Resin Infusion Molding Process
TARDEC	U.S. Army Tank-Automotive Research, Development, and Engineering Center
Tg	glass transition temperature
UD-CCM	University of Delaware Center for Composite Materials
UDLP	United Defense Limited Partnership
VARTM	vacuum-assisted resin-transfer molding

INTENTIONALLY LEFT BLANK.

NO. OF COPIES	ORGANIZATION	NO. OF COPIES	ORGANIZATION
2	DEFENSE TECHNICAL INFORMATION CENTER DTIC OCA 8725 JOHN J KINGMAN RD STE 0944 FT BELVOIR VA 22060-6218	1	DIRECTOR US ARMY RESEARCH LAB AMSRL CI AI R 2800 POWDER MILL RD ADELPHI MD 20783-1197
1	HQDA DAMO FDT 400 ARMY PENTAGON WASHINGTON DC 20310-0460	3	DIRECTOR US ARMY RESEARCH LAB AMSRL CI LL 2800 POWDER MILL RD ADELPHI MD 20783-1197
1	OSD OUSD(A&T)/ODDR&E(R) DR R J TREW 3800 DEFENSE PENTAGON WASHINGTON DC 20301-3800	3	DIRECTOR US ARMY RESEARCH LAB AMSRL CI AP 2800 POWDER MILL RD ADELPHI MD 20783-1197
1	COMMANDING GENERAL US ARMY MATERIEL CMD AMCRDA TF 5001 EISENHOWER AVE ALEXANDRIA VA 22333-0001		ABERDEEN PROVING GROUND
1	INST FOR ADVNCD TCHNLGY THE UNIV OF TEXAS AT AUSTIN 3925 W BRAKER LN STE 400 AUSTIN TX 78759-5316	2	DIR USARL AMSRL CI LP (BLDG 305)
1	DARPA SPECIAL PROJECTS OFFICE J CARLINI 3701 N FAIRFAX DR ARLINGTON VA 22203-1714		
1	US MILITARY ACADEMY MATH SCI CTR EXCELLENCE MADN MATH MAJ HUBER THAYER HALL WEST POINT NY 10996-1786		
1	DIRECTOR US ARMY RESEARCH LAB AMSRL D DR D SMITH 2800 POWDER MILL RD ADELPHI MD 20783-1197		

NO. OF COPIES	ORGANIZATION	NO. OF COPIES	ORGANIZATION
1	DIRECTOR US ARMY RESEARCH LAB AMSRL CP CA D SNIDER 2800 POWDER MILL RD ADELPHI MD 20783-1145	2	COMMANDER US ARMY ARDEC AMSTA AR AE WW E BAKER J PEARSON PICATINNY ARSENAL NJ 07806-5000
1	DIRECTOR US ARMY RESEARCH LAB AMSRL OP SD TA 2800 POWDER MILL RD ADELPHI MD 20783-1145	1	COMMANDER US ARMY ARDEC AMSTA AR TD C SPINELLI PICATINNY ARSENAL NJ 07806-5000
3	DIRECTOR US ARMY RESEARCH LAB AMSRL OP SD TL 2800 POWDER MILL RD ADELPHI MD 20783-1145	1	COMMANDER US ARMY ARDEC AMSTA AR FSE PICATINNY ARSENAL NJ 07806-5000
1	DIRECTOR US ARMY RESEARCH LAB AMSRL OP SD TP 2800 POWDER MILL RD ADELPHI MD 20783-1145	6	COMMANDER US ARMY ARDEC AMSTA AR CCH A W ANDREWS S MUSALLI R CARR M LUCIANO E LOGSDEN T LOUZEIRO PICATINNY ARSENAL NJ 07806-5000
1	DIRECTOR DA OASARDA SARD SO 103 ARMY PENTAGON WASHINGTON DC 20310-0103		
1	DPTY ASST SECY FOR R&T SARD TT THE PENTAGON RM 3EA79 WASHINGTON DC 20301-7100	1	COMMANDER US ARMY ARDEC AMSTA AR CCH P J LUTZ PICATINNY ARSENAL NJ 07806-5000
1	COMMANDER US ARMY MATERIEL CMD AMXMI INT 5001 EISENHOWER AVE ALEXANDRIA VA 22333-0001	1	COMMANDER US ARMY ARDEC AMSTA AR FSF T C LIVECCHIA PICATINNY ARSENAL NJ 07806-5000
4	COMMANDER US ARMY ARDEC AMSTA AR CC G PAYNE J GEHBAUER C BAULIEU H OPAT PICATINNY ARSENAL NJ 07806-5000	1	COMMANDER US ARMY ARDEC AMSTA AR QAC T C C PATEL PICATINNY ARSENAL NJ 07806-5000

NO. OF COPIES	ORGANIZATION
1	COMMANDER US ARMY ARDEC AMSTA AR M D DEMELLA PICATINNY ARSENAL NJ 07806-5000
3	COMMANDER US ARMY ARDEC AMSTA AR FSA A WARNASH B MACHAK M CHIEFA PICATINNY ARSENAL NJ 07806-5000
2	COMMANDER US ARMY ARDEC AMSTA AR FSP G M SCHIKSNIS D CARLUCCI PICATINNY ARSENAL NJ 07806-5000
1	COMMANDER US ARMY ARDEC AMSTA AR FSP A P KISATSKY PICATINNY ARSENAL NJ 07806-5000
2	COMMANDER US ARMY ARDEC AMSTA AR CCH C H CHANIN S CHICO PICATINNY ARSENAL NJ 07806-5000
1	COMMANDER US ARMY ARDEC AMSTA ASF PICATINNY ARSENAL NJ 07806-5000
1	COMMANDER US ARMY ARDEC AMSTA AR WET T SACHAR BLDG 172 PICATINNY ARSENAL NJ 07806-5000

NO. OF COPIES	ORGANIZATION
9	COMMANDER US ARMY ARDEC AMSTA AR CCH B P DONADIA F DONLON P VALENTI C KNUTSON G EUSTICE S PATEL G WAGNECZ R SAYER F CHANG PICATINNY ARSENAL NJ 07806-5000
6	COMMANDER US ARMY ARDEC AMSTA AR CCL F PUZYCKI R MCHUGH D CONWAY E JAROSZEWSKI R SCHLENNER M CLUNE PICATINNY ARSENAL NJ 07806-5000
1	COMMANDER US ARMY ARDEC AMSTA AR QAC T D RIGOGLIOSO PICATINNY ARSENAL NJ 07806-5000
1	COMMANDER US ARMY ARDEC AMSTA AR SRE D YEE PICATINNY ARSENAL NJ 07806-5000
1	US ARMY ARDEC INTELLIGENCE SPECIALIST AMSTA AR WEL F M GUERRIERE PICATINNY ARSENAL NJ 07806-5000
2	PEO FIELD ARTILLERY SYS SFAE FAS PM H GOLDMAN T MCWILLIAMS PICATINNY ARSENAL NJ 07806-5000

NO. OF COPIES	ORGANIZATION	NO. OF COPIES	ORGANIZATION
11	PM TMAS SFAE GSSC TMA R MORRIS C KIMKER D GUZOWICZ E KOPACZ R ROESER R DARCY R MCDANOLDS L D ULISSE C ROLLER J MCGREEN B PATTER PICATINNY ARSENAL NJ 07806-5000	3	COMMANDER US ARMY TACOM PM TACTICAL VEHICLES SFAE TVL SFAE TVM SFAE TVH 6501 ELEVEN MILE RD WARREN MI 48397-5000
1	COMMANDER US ARMY ARDEC AMSTA AR WEA J BRESCIA PICATINNY ARSENAL NJ 07806-5000	1	COMMANDER US ARMY TACOM PM BFVS SFAE ASM BV 6501 ELEVEN MILE RD WARREN MI 48397-5000
1	COMMANDER US ARMY ARDEC PRODUCTION BASE MODERN ACTY AMSMC PBM K PICATINNY ARSENAL NJ 07806-5000	1	COMMANDER US ARMY TACOM PM AFAS SFAE ASM AF 6501 ELEVEN MILE RD WARREN MI 48397-5000
1	COMMANDER US ARMY TACOM PM ABRAMS SFAE ASM AB 6501 ELEVEN MILE RD WARREN MI 48397-5000	1	COMMANDER US ARMY TACOM PM RDT&E SFAE GCSS W AB J GODELL 6501 ELEVEN MILE RD WARREN MI 48397-5000
6	PM SADARM SFAE GCSS SD COL B ELLIS M DEVINE R KOWALSKI W DEMASSI J PRITCHARD S HROWNAK PICATINNY ARSENAL NJ 07806-5000	2	COMMANDER US ARMY TACOM PM SURV SYS SFAE ASM SS T DEAN SFAE GCSS W GSI M D COCHRAN 6501 ELEVEN MILE RD WARREN MI 48397-5000
		1	US ARMY CERL R LAMPO 2902 NEWMARK DR CHAMPAIGN IL 61822
1	COMMANDER US ARMY TACOM AMSTA SF WARREN MI 48397-5000	1	COMMANDER US ARMY TACOM PM SURVIVABLE SYSTEMS SFAE GCSS W GSI H M RYZYI 6501 ELEVEN MILE RD WARREN MI 48397-5000

NO. OF COPIES	ORGANIZATION	NO. OF COPIES	ORGANIZATION
1	COMMANDER US ARMY TACOM PM BFV SFAE GCSS W BV S DAVIS 6501 ELEVEN MILE RD WARREN MI 48397-5000	1	COMMANDER WATERVLIET ARSENAL SMCWV SPM T MCCLOSKEY BLDG 253 WATERVLIET NY 12189-4050
1	COMMANDER US ARMY TACOM PM LIGHT TACTICAL VHCLS AMSTA TR S A J MILLS MS 209 6501 ELEVEN MILE RD WARREN MI 48397-5000	2	TSM ABRAMS ATZK TS S JABURG W MEINSHAUSEN FT KNOX KY 40121
1	COMMANDER US ARMY TACOM CHIEF ABRAMS TESTING SFAE GCSS W AB QT T KRASKIEWICZ 6501 ELEVEN MILE RD WARREN MI 48397-5000	3	ARMOR SCHOOL ATZK TD R BAUEN J BERG A POMEY FT KNOX KY 40121
15	COMMANDER US ARMY TACOM AMSTA TR R J CHAPIN R MCCLELLAND D THOMAS J BENNETT D HANSEN AMSTA JSK S GOODMAN J FLORENCE K IYER D TEMPLETON A SCHUMACHER AMSTA TR D D OSTBERG L HINOJOSA B RAJU AMSTA CS SF H HUTCHINSON F SCHWARZ WARREN MI 48397-5000	11	BENET LABORATORIES AMSTA AR CCB R FISCELLA G D ANDREA E KATHE M SCAVULO G SPENCER P WHEELER K MINER J VASILAKIS G FRIAR R HASENBEIN AMSTA CCB R S SOPOK WATERVLIET NY 12189-4050
		2	HQ IOC TANK AMMUNITION TEAM AMSIO SMT R CRAWFORD W HARRIS ROCK ISLAND IL 61299-6000
		2	DAVID TAYLOR RESEARCH CTR R ROCKWELL W PHYILLAIER BETHESDA MD 20054-5000
1	COMMANDER WATERVLIET ARSENAL SMCWV QAE Q B VANINA BLDG 44 WATERVLIET NY 12189-4050	2	COMMANDER US ARMY AMCOM AVIATION APPLIED TECH DIR J SCHUCK FT EUSTIS VA 23604-5577

NO. OF COPIES	ORGANIZATION	NO. OF COPIES	ORGANIZATION
1	DIRECTOR US ARMY AMCOM SFAE AV RAM TV D CALDWELL BLDG 5300 REDSTONE ARSENAL AL 35898	1	NAVAL SURFACE WARFARE CTR DAHLGREN DIV CODE G06 DAHLGREN VA 22448
2	US ARMY CORPS OF ENGINEERS CERD C T LIU CEW ET T TAN 20 MASS AVE NW WASHINGTON DC 20314	1	NAVAL SURFACE WARFARE CTR TECH LIBRARY CODE 323 17320 DAHLGREN RD DAHLGREN VA 22448
		1	NAVAL SURFACE WARFARE CTR CRANE DIVISION M JOHNSON CODE 20H4 LOUISVILLE KY 40214-5245
1	US ARMY COLD REGIONS RSCH & ENGRNG LAB P DUTTA 72 LYME RD HANOVER NH 03755	8	DIRECTOR US ARMY NATIONAL GROUND INTELLIGENCE CTR D LEITER M HOLTUS M WOLFE S MINGLEDORF J GASTON W GSTATTENBAUER R WARNER J CRIDER 220 SEVENTH ST NE CHARLOTTESVILLE VA 22091
1	SYSTEM MANAGER ABRAMS ATZK TS LTC J H NUNN BLDG 1002 RM 110 FT KNOX KY 40121
1	USA SBCCOM PM SOLDIER SPT AMSSB PM RSS A J CONNORS KANSAS ST NATICK MA 01760-5057	6	US ARMY SBCCOM SOLDIER SYSTEMS CENTER BALLISTICS TEAM J WARD MARINE CORPS TEAM J MACKIEWICZ BUS AREA ADVOCACY TEAM W HASKELL SSCNC WST W NYKVIST T MERRILL S BEAUDOIN KANSAS ST NATICK MA 01760-5019
3	BALLISTICS TEAM AMSSB RIP PHIL CUNNIFF JOHN SONG WALTER ZUKAS KANSAS ST NATICK MA 01760-5057
2	MATERIAL SCIENCE TEAM AMSSB RSS JEAN HERBERT MICHAEL SENNETT KANSAS ST NATICK MA 01760-5057	3	NAVAL RESEARCH LAB I WOLOCK CODE 6383 R BADALIANCE CODE 6304 L GAUSE WASHINGTON DC 20375
2	OFC OF NAVAL RESEARCH D SIEGEL CODE 351 J KELLY 800 N QUINCY ST ARLINGTON VA 22217-5660	2	NAVAL SURFACE WARFARE CTR U SORATHIA C WILLIAMS CD 6551 9500 MACARTHUR BLVD WEST BETHESDA MD 20817

NO. OF COPIES	ORGANIZATION	NO. OF COPIES	ORGANIZATION
9	US ARMY RESEARCH OFC A CROWSON J CHANDRA H EVERETT J PRATER R SINGLETON G ANDERSON D STEPP D KISEROW J CHANG PO BOX 12211 RESEARCH TRIANGLE PARK NC 27709-2211	1	AFRL MLBC 2941 P ST RM 136 WRIGHT PATTERSON AFB OH 45433-7750
		1	AFRL MLSS R THOMSON 2179 12TH ST RM 122 WRIGHT PATTERSON AFB OH 45433-7718
2	COMMANDER NAVAL SURFACE WARFARE CTR CARDEROCK DIVISION R PETERSON CODE 2020 M CRITCHFIELD CODE 1730 BETHESDA MD 20084	2	AFRL F ABRAMS J BROWN BLDG 653 2977 P ST STE 6 WRIGHT PATTERSON AFB OH 45433-7739
8	NAVAL SURFACE WARFARE CTR J FRANCIS CODE G30 D WILSON CODE G32 R D COOPER CODE G32 J FRAYSSE CODE G33 E ROWE CODE G33 T DURAN CODE G33 L DE SIMONE CODE G33 R HUBBARD CODE G33 DAHLGREN VA 22448	1	AFRL MLS OL L COULTER 7278 4TH ST BLDG 100 BAY D HILL AFB UT 84056-5205
		1	OSD JOINT CCD TEST FORCE OSD JCCD R WILLIAMS 3909 HALLS FERRY RD VICKSBURG MS 29180-6199
1	NAVAL SEA SYSTEMS CMD D LIESE 2531 JEFFERSON DAVIS HWY ARLINGTON VA 22242-5160	1	DEFENSE NUCLEAR AGENCY INNOVATIVE CONCEPTS DIV 6801 TELEGRAPH RD ALEXANDRIA VA 22310-3398
1	NAVAL SURFACE WARFARE CTR M LACY CODE B02 17320 DAHLGREN RD DAHLGREN VA 22448	1	WATERWAYS EXPERIMENT D SCOTT 3909 HALLS FERRY RD SC C VICKSBURG MS 39180
2	NAVAL SURFACE WARFARE CTR CARDEROCK DIVISION R CRANE CODE 2802 C WILLIAMS CODE 6553 3A LEGGETT CIR BETHESDA MD 20054-5000	5	DIRECTOR LLNL R CHRISTENSEN S DETERESA F MAGNESS M FINGER MS 313 M MURPHY L 282 PO BOX 808 LIVERMORE CA 94550
1	EXPEDITIONARY WARFARE DIV N85 F SHOUP 2000 NAVY PENTAGON WASHINGTON DC 20350-2000		

NO. OF COPIES	ORGANIZATION	NO. OF COPIES	ORGANIZATION
3	DARPA M VANFOSSEN S WAX L CHRISTODOULOU 3701 N FAIRFAX DR ARLINGTON VA 22203-1714	1	OAK RIDGE NATIONAL LABORATORY C EBERLE MS 8048 PO BOX 2008 OAK RIDGE TN 37831
2	FAA TECH CENTER P SHYPRYKEVICH AAR 431 ATLANTIC CITY NJ 08405	1	OAK RIDGE NATIONAL LABORATORY C D WARREN MS 8039 PO BOX 2008 OAK RIDGE TN 37831
2	SERDP PROGRAM OFC PM P2 C PELLERIN B SMITH 901 N STUART ST STE 303 ARLINGTON VA 22203	7	NIST R PARNAS J DUNKERS M VANLANDINGHAM MS 8621 J CHIN MS 8621 D HUNSTON MS 8543 J MARTIN MS 8621 D DUTHINH MS 8611 100 BUREAU DR GAITHERSBURG MD 20899
1	FAA MIL HDBK 17 CHAIR L ILCEWICZ 1601 LIND AVE SW ANM 115N RESTON VA 98055	1	HYDROGEOLOGIC INC SERDP ESTCP SPT OFC S WALSH 1155 HERNDON PKWY STE 900 HERNDON VA 20170
1	US DEPT OF ENERGY OFC OF ENVIRONMENTAL MANAGEMENT P RITZCOVAN 19901 GERMANTOWN RD GERMANTOWN MD 20874-1928	3	NASA LANGLEY RSCH CTR AMSRL VS W ELBER MS 266 F BARTLETT JR MS 266 G FARLEY MS 266 HAMPTON VA 23681-0001
1	DIRECTOR LLNL F ADDESSIO MS B216 PO BOX 1633 LOS ALAMOS NM 87545	1	NASA LANGLEY RSCH CTR T GATES MS 188E HAMPTON VA 23661-3400
1	OAK RIDGE NATIONAL LABORATORY R M DAVIS PO BOX 2008 OAK RIDGE TN 37831-6195	1	FHWA E MUNLEY 6300 GEORGETOWN PIKE MCLEAN VA 22101
3	DIRECTOR SANDIA NATIONAL LABS APPLIED MECHANICS DEPT MS 9042 J HANDROCK Y R KAN J LAUFFER PO BOX 969 LIVERMORE CA 94551-0969	4	CYTEC FIBERITE R DUNNE D KOHLI M GILLIO R MAYHEW 1300 REVOLUTION ST HAVRE DE GRACE MD 21078

NO. OF COPIES	ORGANIZATION	NO. OF COPIES	ORGANIZATION
1	USDOT FEDERAL RAILRD M FATEH RDV 31 WASHINGTON DC 20590	2	COMPOSIX D BLAKE L DIXON 120 O NEILL DR HEBRUN OH 43025
1	CENTRAL INTLLGNC AGNCY OTI WDAG GT W L WALTMAN PO BOX 1925 WASHINGTON DC 20505	2	SIMULA J COLTMAN R HUYETT 10016 S 51ST ST PHOENIX AZ 85044
1	MARINE CORPS INTLLGNC ACTVTY D KOSITZKE 3300 RUSSELL RD STE 250 QUANTICO VA 22134-5011	1	SIOUX MFG B KRIEL PO BOX 400 FT TOTTEN ND 58335
1	DIRECTOR NATIONAL GRND INTLLGNC CTR IANG TMT 220 SEVENTH ST NE CHARLOTTESVILLE VA 22902-5396	2	PROTECTION MATERIALS INC M MILLER F CRILLEY 14000 NW 58 CT MIAMI LAKES FL 33014
1	DIRECTOR DEFENSE INTLLGNC AGNCY TA 5 K CRELLING WASHINGTON DC 20310	3	FOSTER MILLER J J GASSNER M ROYLANCE W ZUKAS 195 BEAR HILL RD WALTHAM MA 02354-1196
1	ADVANCED GLASS FIBER YARNS T COLLINS 281 SPRING RUN LANE STE A DOWNINGTON PA 19335	1	ROM DEVELOPMENT CORP R O MEARA 136 SWINEBURNE ROW BRICK MARKET PLACE NEWPORT RI 02840
1	COMPOSITE MATERIALS INC D SHORTT 19105 63 AVE NE PO BOX 25 ARLINGTON WA 98223	2	TEXTRON SYSTEMS T FOLTZ M TREASURE 201 LOWELL ST WILMINGTON MA 08870-2941
1	JPS GLASS L CARTER PO BOX 260 SLATER RD SLATER SC 29683	1	GLCC INC J RAY 103 TRADE ZONE DR STE 26C WEST COLUMBIA SC 29170
1	COMPOSITE MATERIALS INC R HOLLAND 11 JEWEL CT ORINDA CA 94563	1	O GARA HESS & EISENHARDT M GILLESPIE 9113 LESAINT DR FAIRFIELD OH 45014
1	COMPOSITE MATERIALS INC C RILEY 14530 S ANSON AVE SANTA FE SPRINGS CA 90670		

NO. OF COPIES	ORGANIZATION
2	MILLIKEN RSCH CORP H KUHN M MACLEOD PO BOX 1926 SPARTANBURG SC 29303
1	CONNEAUGHT INDUSTRIES INC J SANTOS PO BOX 1425 COVENTRY RI 02816
2	BATTELLE NATICK OPNS J CONNORS B HALPIN 209 W CENTRAL ST STE 302 NATICK MA 01760
1	ARMTEC DEFENSE PRODUCTS S DYER 85 901 AVE 53 PO BOX 848 COACHELLA CA 92236
3	PACIFIC NORTHWEST LAB M SMITH G VAN ARSDALE R SHIPPELL PO BOX 999 RICHLAND WA 99352
8	ALLIANT TECHSYSTEMS INC C CANDLAND MN11 2830 C AAKHUS MN11 2830 B SEE MN11 2439 N VLAHAKUS MN11 2145 R DOHRN MN11 2830 S HAGLUND MN11 2439 M HISSONG MN11 2830 D KAMDAR MN11 2830 600 SECOND ST NE HOPKINS MN 55343-8367
2	AMOCO PERFORMANCE PRODUCTS M MICHNO JR J BANISAUKAS 4500 MCGINNIS FERRY RD ALPHARETTA GA 30202-3944
1	SAIC M PALMER 1410 SPRING HILL RD STE 400 MS SH4 5 MCLEAN VA 22102

NO. OF COPIES	ORGANIZATION
1	SAIC G CHRYSSOMALLIS 3800 W 80TH ST STE 1090 BLOOMINGTON MN 55431
1	AAI CORPORATION T G STASTNY PO BOX 126 HUNT VALLEY MD 21030-0126
1	APPLIED COMPOSITES W GRISCH 333 NORTH SIXTH ST ST CHARLES IL 60174
3	ALLIANT TECHSYSTEMS INC J CONDON E LYNAM J GERHARD WV01 16 STATE RT 956 PO BOX 210 ROCKET CENTER WV 26726-0210
1	CUSTOM ANALYTICAL ENG SYS INC A ALEXANDER 13000 TENSOR LANE NE FLINTSTONE MD 21530
1	OFC DEPUTY UNDER SEC DEFNS JAMES THOMPSON 1745 JEFFERSON DAVIS HWY CRYSTAL SQ 4 STE 501 ARLINGTON VA 22202
1	PROJECTILE TECHNOLOGY INC 515 GILES ST HAVRE DE GRACE MD 21078
5	AEROJET GEN CORP D PILLASCH T COULTER C FLYNN D RUBAREZUL M GREINER 1100 WEST HOLLYVALE ST AZUSA CA 91702-0296
3	HEXCEL INC R BOE PO BOX 18748 SALT LAKE CITY UT 84118

NO. OF COPIES	ORGANIZATION	NO. OF COPIES	ORGANIZATION
1	HERCULES INC HERCULES PLAZA WILMINGTON DE 19894	2	CYTEC FIBERITE M LIN W WEB 1440 N KRAEMER BLVD ANAHEIM CA 92806
1	BRIGS COMPANY J BACKOFEN 2668 PETERBOROUGH ST HERNDON VA 22071-2443	1	HEXCEL T BITZER 11711 DUBLIN BLVD DUBLIN CA 94568
1	ZERNOW TECHNICAL SERVICES L ZERNOW 425 W BONITA AVE STE 208 SAN DIMAS CA 91773	1	BOEING R BOHLMANN PO BOX 516 MC 5021322 ST LOUIS MO 63166-0516
2	OLIN CORPORATION FLINCHBAUGH DIV E STEINER B STEWART PO BOX 127 RED LION PA 17356	2	BOEING DFNSE & SPACE GP W HAMMOND S 4X55 J RUSSELL S 4X55 PO BOX 3707 SEATTLE WA 98124-2207
1	OLIN CORPORATION L WHITMORE 10101 NINTH ST NORTH ST PETERSBURG FL 33702	2	BOEING ROTORCRAFT P MINGURT P HANDEL 800 B PUTNAM BLVD WALLINGFORD PA 19086
1	GKN AEROSPACE D OLDS 15 STERLING DR WALLINGFORD CT 06492	1	BOEING DOUGLAS PRODUCTS DIV L J HART SMITH 3855 LAKEWOOD BLVD D800 0019 LONG BEACH CA 90846-0001
5	SIKORSKY AIRCRAFT G JACARUSO T CARSTENSAN B KAY S GARBO MS S330A J ADELMANN 6900 MAIN ST PO BOX 9729 STRATFORD CT 06497-9729	1	LOCKHEED MARTIN S REEVE 8650 COBB DR D 73 62 MZ 0648 MARIETTA GA 30063-0648
1	PRATT & WHITNEY C WATSON 400 MAIN ST MS 114 37 EAST HARTFORD CT 06108	1	LOCKHEED MARTIN SKUNK WORKS D FORTNEY 1011 LOCKHEED WAY PALMDALE CA 93599-2502
1	AEROSPACE CORP G HAWKINS M4 945 2350 E EL SEGUNDO BLVD EL SEGUNDO CA 90245	1	LOCKHEED MARTIN R FIELDS 1195 IRWIN CT WINTER SPRINGS FL 32708

NO. OF COPIES	ORGANIZATION	NO. OF COPIES	ORGANIZATION
1	MATERIALS SCIENCES CORP B W ROSEN 500 OFC CENTER DR STE 250 FT WASHINGTON PA 19034	2	GDLS D REES M PASIK PO BOX 2074 WARREN MI 48090-2074
1	UDLP D MARTIN PO BOX 359 SANTA CLARA CA 95052	1	GDLS MUSKEGON OPERATIONS W SOMMERS JR 76 GETTY ST MUSKEGON MI 49442
1	NORTHRUP GRUMMAN CORP ELECTRONIC SENSORS & SYSTEMS DIV E SCHOCH MS V 16 1745A W NURSERY RD LINTHICUM MD 21090	1	GENERAL DYNAMICS AMPHIBIOUS SYS SURVIVABILITY LEAD G WALKER 991 ANNAPOLIS WAY WOODBRIDGE VA 22191
2	NORTHROP GRUMMAN ENVIRONMENTAL PROGRAMS R OSTERMAN A YEN 8900 E WASHINGTON BLVD PICO RIVERA CA 90660	6	INST FOR ADVANCED TECH H FAIR I MCNAB P SULLIVAN S BLESS W REINECKE C PERSAD 3925 W BRAKER LN STE 400 AUSTIN TX 78759-5316
1	UDLP G THOMAS PO BOX 58123 SANTA CLARA CA 95052		
2	UDLP R BARRETT MAIL DROP M53 V HORVATICH MAIL DROP M53 328 W BROKAW RD SANTA CLARA CA 95052-0359	2	CIVIL ENGR RSCH FOUNDATION PRESIDENT H BERNSTEIN R BELLE 1015 15TH ST NW STE 600 WASHINGTON DC 20005
3	UDLP GROUND SYSTEMS DIVISION M PEDRAZZI MAIL DROP N09 A LEE MAIL DROP N11 M MACLEAN MAIL DROP N06 1205 COLEMAN AVE SANTA CLARA CA 95052	1	ARROW TECH ASSO 1233 SHELBURNE RD STE D8 SOUTH BURLINGTON VT 05403-7700
4	UDLP R BRYNSVOLD P JANKE MS 170 4800 EAST RIVER RD MINNEAPOLIS MN 55421-1498	1	R EICHELBERGER CONSULTANT 409 W CATHERINE ST BEL AIR MD 21014-3613
1	GDLS DIVISION D BARTLE PO BOX 1901 WARREN MI 48090	1	UCLA MANE DEPT ENGR IV H T HAHN LOS ANGELES CA 90024-1597

NO. OF COPIES	ORGANIZATION	NO. OF COPIES	ORGANIZATION
2	UNIV OF DAYTON RESEARCH INST R Y KIM A K ROY 300 COLLEGE PARK AVE DAYTON OH 45469-0168	1	STANFORD UNIV DEPT OF AERONAUTICS & AEROBALLISTICS S TSAI DURANT BLDG STANFORD CA 94305
1	MIT P LAGACE 77 MASS AVE CAMBRIDGE MA 01887	1	UNIV OF DAYTON J M WHITNEY COLLEGE PARK AVE DAYTON OH 45469-0240
1	IIT RESEARCH CENTER D ROSE 201 MILL ST ROME NY 13440-6916	7	UNIV OF DELAWARE CTR FOR COMPOSITE MTRLS J GILLESPIE M SANTARE G PALMESE S YARLAGADDA S ADVANI D HEIDER D KUKICH 201 SPENCER LABORATORY NEWARK DE 19716
1	GA TECH RSCH INST GA INST OF TCHNLGY P FRIEDERICH ATLANTA GA 30392		
1	MICHIGAN ST UNIV MSM DEPT R AVERILL 3515 EB EAST LANSING MI 48824-1226	1	DEPT OF MATERIALS SCIENCE & ENGINEERING UNIVERSITY OF ILLINOIS AT URBANA CHAMPAIGN J ECONOMY 1304 WEST GREEN ST 115B URBANA IL 61801
1	UNIV OF KENTUCKY L PENN 763 ANDERSON HALL LEXINGTON KY 40506-0046		
1	UNIV OF WYOMING D ADAMS PO BOX 3295 LARAMIE WY 82071	1	NORTH CAROLINA STATE UNIV CIVIL ENGINEERING DEPT W RASDORF PO BOX 7908 RALEIGH NC 27696-7908
2	PENN STATE UNIV R MCNITT C BAKIS 212 EARTH ENGR SCIENCES BLDG UNIVERSITY PARK PA 16802	1	UNIV OF MARYLAND DEPT OF AEROSPACE ENGNRNG A J VIZZINI COLLEGE PARK MD 20742
1	PENN STATE UNIV R S ENGEL 245 HAMMOND BLDG UNIVERSITY PARK PA 16801	3	UNIV OF TEXAS AT AUSTIN CTR FOR ELECTROMECHANICS J PRICE A WALLS J KITZMILLER 10100 BURNET RD AUSTIN TX 78758-4497
1	PURDUE UNIV SCHOOL OF AERO & ASTRO C T SUN W LAFAYETTE IN 47907-1282		

NO. OF COPIES	ORGANIZATION	NO. OF COPIES	ORGANIZATION
3	VA POLYTECHNICAL INST & STATE UNIV DEPT OF ESM M W HYER K REIFSNIDER R JONES BLACKSBURG VA 24061-0219		ABERDEEN PROVING GROUND (CONT)

3	VA POLYTECHNICAL INST & STATE UNIV DEPT OF ESM M W HYER K REIFSNIDER R JONES BLACKSBURG VA 24061-0219		

ABERDEEN PROVING GROUND (CONT)

3 VA POLYTECHNICAL
INST & STATE UNIV
DEPT OF ESM
M W HYER
K REIFSNIDER
R JONES
BLACKSBURG VA 24061-0219

1 DREXEL UNIV
A S D WANG
32ND & CHESTNUT ST
PHILADELPHIA PA 19104

1 SOUTHWEST RSCH INST
ENGR & MATL SCIENCES DIV
J RIEGEL
6220 CULEBRA RD
PO DRAWER 28510
SAN ANTONIO TX 78228-0510

ABERDEEN PROVING GROUND

1 US ARMY MATERIEL
SYSTEMS ANALYSIS ACTIVITY
P DIETZ
392 HOPKINS RD
AMXSY TD
APG MD 21005-5071

1 DIRECTOR
US ARMY RESEARCH LAB
AMSRL OP AP L
APG MD 21005-5066

105 DIR USARL
AMSRL CI
AMSRL CI H
  W STUREK
AMSRL CI S
  A MARK
AMSRL CS IO FI
  M ADAMSON
AMSRL SL B
  J SMITH
AMSRL SL BA
AMSRL SL BL
  D BELY
  R HENRY
AMSRL SL BG
AMSRL SL I
AMSRL WM
  E SCHMIDT

AMSRL WM B
  A HORST
AMSRL WM BA
  F BRANDON
AMSRL WM BC
  P PLOSTINS
  D LYON
  J NEWILL
  S WILKERSON
  A ZIELINSKI
AMSRL WM BD
  B FORCH
  R FIFER
  R PESCE RODRIGUEZ
  B RICE
AMSRL WM BE
  C LEVERITT
  D KOOKER
AMSRL WM BR
  C SHOEMAKER
  J BORNSTEIN
AMSRL WM M
  D VIECHNICKI
  G HAGNAUER
  J MCCAULEY
  B TANNER
AMSRL WM MA
  R SHUFORD
  P TOUCHET
  N BECK TAN
AMSRL WM MA
  D FLANAGAN
  L GHIORSE
  D HARRIS
  S MCKNIGHT
  P MOY
  P PATTERSON
  G RODRIGUEZ
  A TEETS
  R YIN
AMSRL WM MB
  B FINK
  J BENDER
  T BOGETTI
  R BOSSOLI
  L BURTON
  K BOYD
  S CORNELISON
  P DEHMER
  R DOOLEY
  W DRYSDALE
  G GAZONAS

NO. OF COPIES	ORGANIZATION	NO. OF COPIES	ORGANIZATION

ABERDEEN PROVING GROUND (CONT)

ABERDEEN PROVING GROUND (CONT)

AMSRL WM MB
  S GHIORSE
  D GRANVILLE
  D HOPKINS
  C HOPPEL
  D HENRY
  R KASTE
  M KLUSEWITZ
  M LEADORE
  R LIEB
  E RIGAS
  J SANDS
  D SPAGNUOLO
  W SPURGEON
  J TZENG
  E WETZEL
AMSRL WM MB
  A FRYDMAN
AMRSL WM MC
  J BEATTY
  E CHIN
  J MONTGOMERY
  A WERECZCAK
  J LASALVIA
  J WELLS
AMSRL WM MD
  W ROY
  S WALSH
AMSRL WM T
  B BURNS
AMSRL WM TA
  W GILLICH
  T HAVEL
  J RUNYEON
  M BURKINS
  E HORWATH
  B GOOCH
  W BRUCHEY
AMSRL WM TC
  R COATES
AMSRL WM TD
  A DAS GUPTA
  T HADUCH
  T MOYNIHAN
  F GREGORY
  A RAJENDRAN
  M RAFTENBERG
  M BOTELER
  T WEERASOORIYA
  D DANDEKAR
  A DIETRICH

AMSRL WM TE
  A NIILER
  J POWELL
AMSRL SS SD
  H WALLACE
AMSRL SS SE R
  R CHASE
AMSRL SS SE DS
  R REYZER
  R ATKINSON
AMSRL SE L
  R WEINRAUB
  J DESMOND
  D WOODBURY

NO. OF COPIES	ORGANIZATION	NO. OF COPIES	ORGANIZATION
1	LTD R MARTIN MERL TAMWORTH RD HERTFORD SG13 7DG UK	1	ISRAEL INST OF TECHNOLOGY S BODNER FACULTY OF MECHANICAL ENGR HAIFA 3200 ISRAEL
1	SMC SCOTLAND P W LAY DERA ROSYTH ROSYTH ROYAL DOCKYARD DUNFERMLINE FIFE KY 11 2XR UK	1	DSTO MATERIALS RESEARCH LAB NAVAL PLATFORM VULNERABILITY SHIP STRUCTURES & MTRLS DIV N BURMAN PO BOX 50 ASCOT VALE VICTORIA AUSTRALIA 3032
1	CIVIL AVIATION ADMINSTRATION T GOTTESMAN PO BOX 8 BEN GURION INTERNL AIRPORT LOD 70150 ISRAEL	1	ECOLE ROYAL MILITAIRE E CELENS AVE DE LA RENAISSANCE 30 1040 BRUXELLE BELGIQUE
1	AEROSPATIALE S ANDRE A BTE CC RTE MD132 316 ROUTE DE BAYONNE TOULOUSE 31060 FRANCE	1	DEF RES ESTABLISHMENT VALCARTIER A DUPUIS 2459 BOULEVARD PIE XI NORTH VALCARTIER QUEBEC CANADA PO BOX 8800 COURCELETTE GOA IRO QUEBEC CANADA
3	DRA FORT HALSTEAD P N JONES M HINTON SEVEN OAKS KENT TN 147BP UK	1	INSTITUT FRANCO ALLEMAND DE RECHERCHES DE SAINT LOUIS DE M GIRAUD 5 RUE DU GENERAL CASSAGNOU BOITE POSTALE 34 F 68301 SAINT LOUIS CEDEX FRANCE
1	DEFENSE RESEARCH ESTAB VALCARTIER F LESAGE COURCELETTE QUEBEC COA IRO CANADA	1	ECOLE POLYTECH J MANSON DMX LTC CH 1015 LAUSANNE SWITZERLAND
1	SWISS FEDERAL ARMAMENTS WKS W LANZ ALLMENDSTRASSE 86 3602 THUN SWITZERLAND	1	TNO PRINS MAURITS LABORATORY R IJSSELSTEIN LANGE KLEIWEG 137 PO BOX 45 2280 AA RIJSWIJK THE NETHERLANDS

NO. OF COPIES	ORGANIZATION
2	FOA NATL DEFENSE RESEARCH ESTAB DIR DEPT OF WEAPONS & PROTECTION B JANZON R HOLMLIN S 172 90 STOCKHOLM SWEDEN
2	DEFENSE TECH & PROC AGENCY GROUND I CREWTHER GENERAL HERZOG HAUS 3602 THUN SWITZERLAND
1	MINISTRY OF DEFENCE RAFAEL ARMAMENT DEVELOPMENT AUTH M MAYSELESS PO BOX 2250 HAIFA 31021 ISRAEL
1	DYNAMEC RESEARCH AB AKE PERSSON BOX 201 SE 151 23 SODERTALJE SWEDEN
1	TNO DEFENSE RESEARCH I H PASMAN POSTBUS 6006 2600 JA DELFT THE NETHERLANDS
1	B HIRSCH TACHKEMONY ST 6 NETAMUA 42611 ISRAEL
1	DEUTSCHE AEROSPACE AG DYNAMICS SYSTEMS M HELD PO BOX 1340 D 86523 SCHROBENHAUSEN GERMANY

INTENTIONALLY LEFT BLANK.

REPORT DOCUMENTATION PAGE

Public reporting burden for this collection of information is estimated to average 1 hour per response, including the time for reviewing instructions, searching existing data sources, gathering and maintaining the data needed, and completing and reviewing the collection of information. Send comments regarding this burden estimate or any other aspect of this collection of information, including suggestions for reducing this burden, to Washington Headquarters Services, Directorate for Information Operations and Reports, 1215 Jefferson Davis Highway, Suite 1204, Arlington, VA 22202-4302, and to the Office of Management and Budget, Paperwork Reduction Project(0704-0188), Washington, DC 20503.

1. AGENCY USE ONLY (Leave blank)	2. REPORT DATE	3. REPORT TYPE AND DATES COVERED
	May 2001	Final, June 1997–August 1999

4. TITLE AND SUBTITLE
Damage Tolerance of Thick-Section Composites Subjected to Ballistic Impact

5. FUNDING NUMBERS
AH42

6. AUTHOR(S)
Bruce K. Fink, Ahmed M. Monib,[*] and John W. Gillespie, Jr.[*]

7. PERFORMING ORGANIZATION NAME(S) AND ADDRESS(ES)
U.S. Army Research Laboratory
ATTN: AMSRL-WM-MB
Aberdeen Proving Ground, MD 21005-5069

8. PERFORMING ORGANIZATION REPORT NUMBER
ARL-TR-2477

9. SPONSORING/MONITORING AGENCY NAMES(S) AND ADDRESS(ES)

10. SPONSORING/MONITORING AGENCY REPORT NUMBER

11. SUPPLEMENTARY NOTES
[*] University of Delaware, Newark, DE 19716

12a. DISTRIBUTION/AVAILABILITY STATEMENT
Approved for public release; distribution is unlimited.

12b. DISTRIBUTION CODE

13. ABSTRACT (Maximum 200 words)

There are two predominate modes of failure in a compressively loaded laminate that has been subjected to ballistic damage. Analysis has shown that the stress concentration and the membrane failure are sensitive to the in-plane stiffness matrix of the damaged region, while delamination growth failure is dependent on the size and location of the damage as well as the fracture toughness of the material. An experimental study investigated means of improving damage tolerance ranging from resin toughness to through-thickness stitching. From the experimental study, it was found that improving fracture toughness by through-the-thickness stitching resulted in a reduction in damage size. Stitching may cause severe reductions in stiffness of the damage region as projectile energy is absorbed through the fiber breakage and pullout mechanisms. Thus, while stitching improves multi-impact performance, it may also lead to an increase in fiber damage, causing the compression after ballistic impact (CABI) failure mode to shift from delamination growth to membrane failure. A design trade-off exists between maximum fracture toughness and stiffness reduction induced within the ballistically damaged region. By examining the factors affecting residual strength (i.e., fracture toughness, inclusion stiffness, loading condition, and finite width effects) the methodology to develop design chart may be produced to optimize damage tolerance.

14. SUBJECT TERMS
composite material

15. NUMBER OF PAGES
183

16. PRICE CODE

17. SECURITY CLASSIFICATION OF REPORT	18. SECURITY CLASSIFICATION OF THIS PAGE	19. SECURITY CLASSIFICATION OF ABSTRACT	20. LIMITATION OF ABSTRACT
UNCLASSIFIED	UNCLASSIFIED	UNCLASSIFIED	UL

NSN 7540-01-280-5500

Standard Form 298 (Rev. 2-89)
Prescribed by ANSI Std. 239-18   298-102

INTENTIONALLY LEFT BLANK.

USER EVALUATION SHEET/CHANGE OF ADDRESS

This Laboratory undertakes a continuing effort to improve the quality of the reports it publishes. Your comments/answers to the items/questions below will aid us in our efforts.

1. ARL Report Number/Author___ARL-TR-2477 (Fink)_____Date of Report___May 2001_____

2. Date Report Received_____

3. Does this report satisfy a need? (Comment on purpose, related project, or other area of interest for which the report will be used.) _____

_____

4. Specifically, how is the report being used? (Information source, design data, procedure, source of ideas, etc.)_____

_____

_____

5. Has the information in this report led to any quantitative savings as far as man-hours or dollars saved, operating costs avoided, or efficiencies achieved, etc? If so, please elaborate._____

_____

_____

6. General Comments. What do you think should be changed to improve future reports? (Indicate changes to organization, technical content, format, etc.)_____

_____

_____

_____

CURRENT
ADDRESS

Organization
_____

Name   E-mail Name
_____

Street or P.O. Box No.
_____

City, State, Zip Code

7. If indicating a Change of Address or Address Correction, please provide the Current or Correct address above and the Old or Incorrect address below.

OLD
ADDRESS

Organization
_____

Name
_____

Street or P.O. Box No.
_____

City, State, Zip Code

(Remove this sheet, fold as indicated, tape closed, and mail.)
(DO NOT STAPLE)